Oven-Controlled Inertial Sensors

by

Donguk Max Yang

A dissertation submitted in partial fulfillment
of the requirements for the degree of
Doctor of Philosophy
(Electrical and Computer Engineering)
in The University of Michigan
2019

Doctoral Committee:

Professor Khalil Najafi, Chair
Dr. Jae Y. Cho, Enertia Microsystems Inc.
Professor Yogesh Gianchandani
Dr. Jay Mitchell, ePack Inc.
Associate Professor Kenn Oldham

And let steadfastness have its full effect, that you may be
perfect and complete, lacking in nothing.

- James 1:4 -

Donguk Max Yang

yangmax@umich.edu

ORCID iD: 0000-0002-1336-9371

TABLE OF CONTENTS

CHAPTER

LIST OF FIGURES

Figure

LIST OF TABLES

ABSTRACT

MEMS technology has enabled substantial expansion of the inertial sensor market by decreasing power consumption, size, and cost of inertial sensors. Furthermore, with significant performance improvements in recent years, MEMS inertial sensors are used in many emerging applications, including autonomous systems, position-sensing and navigation, space, and defense. However, maintaining high performance of MEMS inertial sensors remains challenging as it is not perfectly resistant to changes in surrounding temperature or other environmental effects.

In this study, a single-isolation stage oven-controlled inertial sensor (SOCIS)—an oven-controlled inertial sensor using one isolation stage—is implemented to mitigate environmental effects. The isolation stage is suspended beam structure and made of low thermal conductivity material to isolate mechanical and thermal effects. A commercial IMU, Invensense MPU-6050, is attached to the isolation stage and vacuum-sealed in the LCC package. Furthermore, to control IMU temperature accurately, different temperature sensing methods are studied, among which the method representing the actual IMU temperature most accurately is selected. Experiment results during thermal-cycle show temperature effects on gyroscopes and accelerometers are improved by 108 and 13.1 times, respectively, for the best SCOIS, while average improvements of eight SOCISs are 11 and 1.1 times, respectively. Furthermore, experiment results during strain-induced stress tests show the stress effect on gyroscopes is improved by 36 times. Finally, simulation results suggest that the SOCIS would filter mechanical vibrations at 3.1kHz or higher.

Although SOCIS mitigated environmental effects significantly, the system is limited by two fundamental limitations: temperature-induced stress, which is caused by temperature gradient and its change on the glass isolation stage, and limited design and material selections for the isolation stage. Therefore, a new structure, a double-isolation stage oven-controlled inertial sensor (DOCIS), is proposed to address these limitations. In DOCIS, the temperature gradient is minimized by replacing glass with silicon. Since such isolation stage cannot provide a good thermal isolation capability, a second stage is added between the silicon stage and LCC package to provide thermal isolation. The second stage is made of cross-linked polyimide aerogel for extremely low thermal conductivity of 0.03W/m·K, and higher mechanical durability than that of typical silica aerogel by 100 times. Furthermore, to increase the thermal resistance of DOCIS further, the contact area between the silicon and aerogel isolation stages is minimized by forming small bonding pads at the bottom surface of the silicon isolation stage, and electrical connections are established using 0.5-mil platinum bonding wires. Simulation and experiment results show that thermal resistance at 1mTorr is 1,700K/W and the maximum temperature-induced stress on inertial sensors would be reduced by 62 times.

Finally, DOICS packaging technology is applied to a fused-silica birdbath shell resonator to mitigate the temperature effect on the resonator and to survive a 5,000g impact. A 9x9 array of square bonding pads is formed at the bottom surface, and no suspended structure is used in the silicon isolation stage. Simulation results show DOCIS will survive a shock impact higher than 5,000g when the width of the square bonding pad is larger than 800μm. Finally, total thermal resistance would be 817K/W, when the aerogel stage is 250μm-thick, 22 electrical connections are established using 0.5-mil platinum wires, and the pressure in the package is lower than 1mTorr. This can be increased to 1180K/W and 1520K/W, if the thickness of the aerogel stage is increased to 375μm and 500μm, respectively.

CHAPTER I

Introduction

Ever since the global navigation satellite system (GNSS) was developed, there have been numerous efforts to improve its position accuracy. As a result, many studies have reported that the GNSS technology can be accurate with cm-level resolution. However, such a highly accurate system requires a large base station nearby the system to reduce the position error, and has other limitations [1, 2]. Furthermore, since the satellites that perform the measurement of the position of an object are orbiting around the earth and sending the information to a receiver through air, this can often create issues in extreme situations, such as during wartime where wireless signals can be jammed or spoofed, in urban canyons where signals can be easily blocked by buildings, underwater/underground applications, and space applications.

Alternatively, an inertial navigation system (INS), which uses inertial sensors, can potentially provide highly accurate position information even in those extreme situations [3]. Inertial sensors are sensors that measure inertia—the angular velocity and acceleration—of an object through mechanical, electrical or optical methods. Two main types of inertial sensors are the gyroscope and the accelerometer. They measure the angular velocity and acceleration of an object, respectively. Although gyroscopes and the accelerometers were first invented in 1852 and 1783, respectively, accurate inertial sensors have not been manufactured until recently, and their performances are becoming much higher than ever [4, 2]. Furthermore, due to the rapid growth in the micro electromechanical system (MEMS) fabrication technology, better understanding of the device, and improvements in device structure, packaging, and interface circuits in the last few decades, MEMS inertial sensors that have high accuracy, lower power consumption, and smaller size have been developed to potentially aid or replace the GNSS in the navigation system [5, 6, 7, 8, 9, 10].

The performance of inertial sensors is classified in five grades as shown in Figure 1.1, and ranges from flight control grade to strategic grade. In this grade classification table, it should be noted that the bias indicates the bias instability that is calculated based on the Allen Deviation plot at room temperature. Many studies have been making progress to develop navigation grade MEMS inertial sensors, and the current state-of-the-art MEMS gyroscopes and accelerometers are shown in Figure 1.3 and Figure 1.2. As shown, assuming that there is no environmental effects on the MEMS inertial sensors, the MEMS accelerometers have already reached the strategic grade, while the best performing MEMs gyroscopes are ranging from the flight grade to the inertial AHRS grade. However, the performance is known to be greatly degrading when they are exposed to environmental effects, such as vibration, stress, temperature, and shock. In this chapter, we will review how environmental effects degrade the performance of MEMS inertial sensors, and how the temperature effect, as one of the most significant source of error, adversely impacts the position error in the INS using state-of-the-art MEMS inertial sensors.

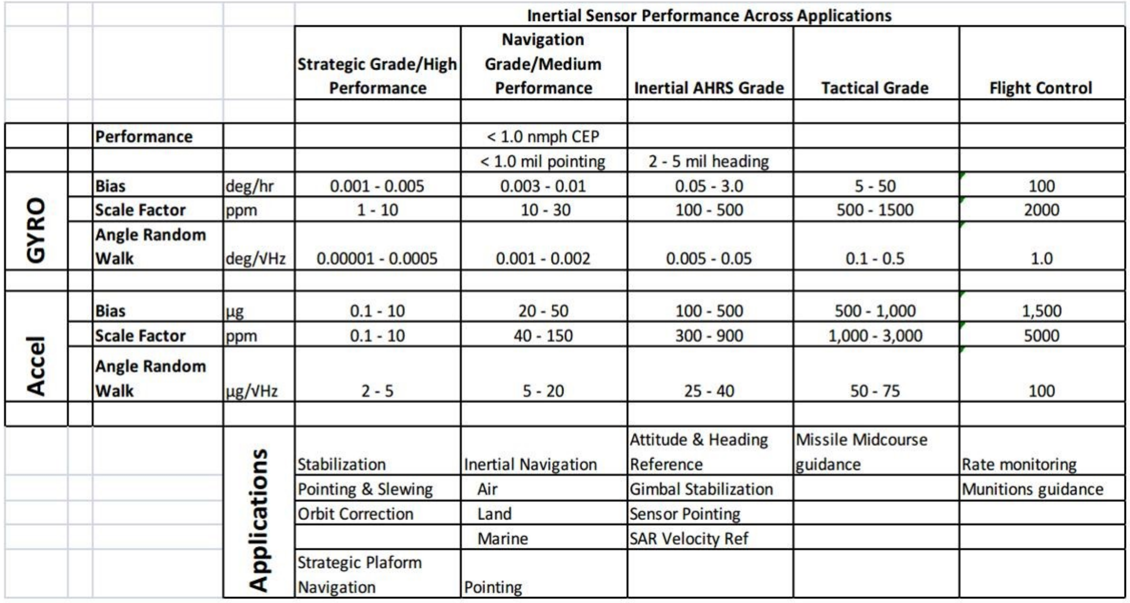

			Inertial Sensor Performance Across Applications				
			Strategic Grade/High Performance	Navigation Grade/Medium Performance	Inertial AHRS Grade	Tactical Grade	Flight Control
	Performance			< 1.0 nmph CEP			
				< 1.0 mil pointing	2 - 5 mil heading		
GYRO	Bias	deg/hr	0.001 - 0.005	0.003 - 0.01	0.05 - 3.0	5 - 50	100
	Scale Factor	ppm	1 - 10	10 - 30	100 - 500	500 - 1500	2000
	Angle Random Walk	deg/√Hz	0.00001 - 0.0005	0.001 - 0.002	0.005 - 0.05	0.1 - 0.5	1.0
Accel	Bias	µg	0.1 - 10	20 - 50	100 - 500	500 - 1,000	1,500
	Scale Factor	ppm	0.1 - 10	40 - 150	300 - 900	1,000 - 3,000	5000
	Angle Random Walk	µg/√Hz	2 - 5	5 - 20	25 - 40	50 - 75	100
		Applications	Stabilization	Inertial Navigation	Attitude & Heading Reference	Missile Midcourse guidance	Rate monitoring
			Pointing & Slewing	Air	Gimbal Stabilization		Munitions guidance
			Orbit Correction	Land	Sensor Pointing		
				Marine	SAR Velocity Ref		
			Strategic Plaform Navigation	Pointing			

Figure 1.1: Inertial sensor Performance Grade [11].

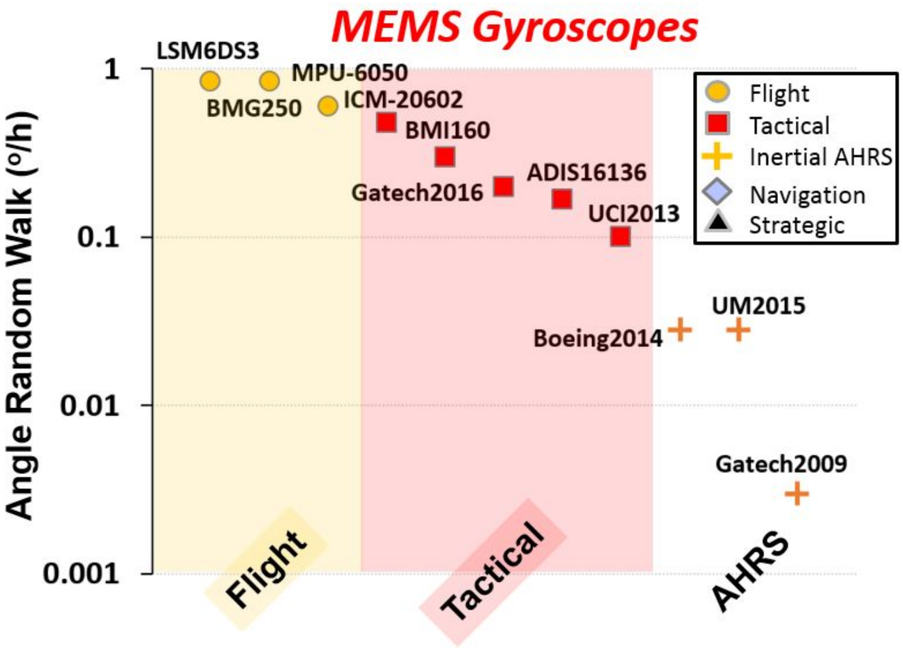

Figure 1.2: Performance Grades of the state-of-the-art MEMS gyroscopes [22, 23, 24, 13, 25, 26, 6, 10, 8, 27, 28].

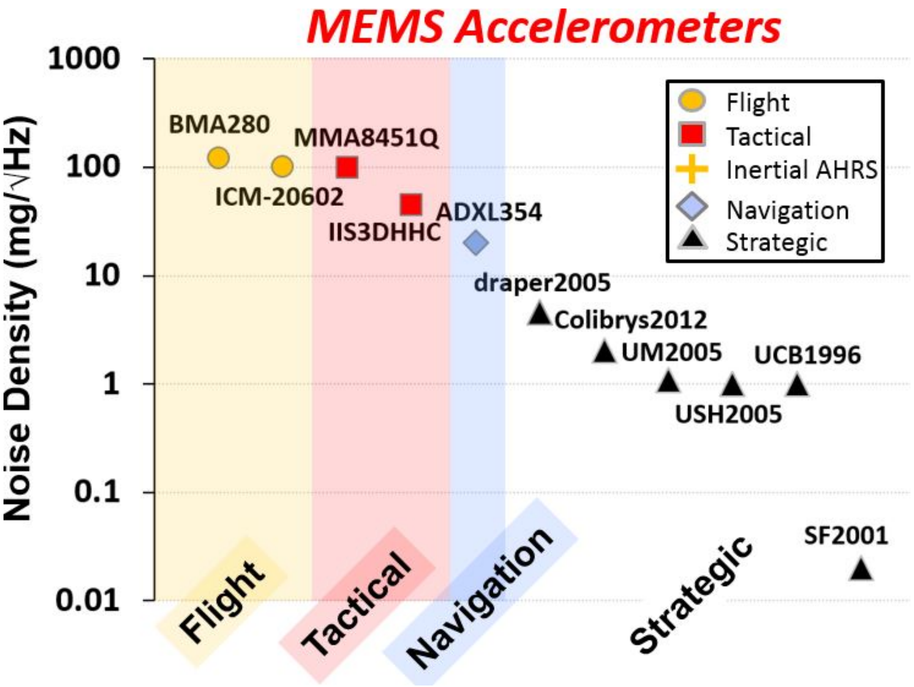

Figure 1.3: Performance Grades of the state-of-the-art MEMS accelerometers [12, 13, 14, 15, 16, 17, 18, 19, 20, 21].

1.1 Noise Performance of State-of-The-Art MEMS Inertial Sensors

Noise performance of an inertial sensor is generally evaluated using two most typical metrics: angle/velocity random walk (ARW/VRW) and bias instability (BI). The ARW and VRW represent white noise of the gyroscope and accelerometer, respectively, and the BI is flicker noise (1/f noise) in the overall system of the inertial sensor. For instance, if inertial sensors show low ARW, VRW, and BI values, then it indicates that the noise performance of the inertial sensor is good. Details about the method to compute the ARW, VRW, and BI values will be discussed in the next chapter.

A number of studies have shown improved performance of MEMS gyroscopes to date, and ARW and BI values of the state-of-the-art gyroscopes are summarized

Table 1.1: Noise performance summary of the state-of-the-art gyroscopes.

Name	**Type**	**BI (°/h)**	**ARW ($^\circ/\sqrt(h)$)**	**Temp Sensitivity (°/h) -40 °C to 85 °C**
MPU-6050	**Commercial**	5	0.3	10000
UCI 2013	**Research**	0.6	0.1	4375
Gatech 2009	**Research**	0.16	0.003	n/a
Gatech 2016	**Research**	10	0.2	28800
Boeing 2014	**Research**	0.025	0.028	1000
UM 2015	**Research**	0.178	0.028	n/a
Navigation Grade	**N/A**	0.01	0.002	0.01

in Table 1.1 [28, 8, 10, 27, 24, 6]. These ARW and BI values are used as inputs to the strap-down INS simulation to compute their position errors. Furthermore, noise level in the MEMS accelerometers is assumed to be negligible and thus not summarized in this study, because the position error in an INS largely comes from MEMS gyroscopes [29].

1.2 Modeling of INSs using State-of-The-Art MEMS Inertial Sensors

Based on the noise performance of the MEMS gyroscopes summarized in the previous section, a strap-down INS model is developed, and used to determine and compare the position errors of the INS using the state-of-the-art MEMS gyroscopes. Three-axis gyroscopes and three-axis accelerometers are used in modeling, and the MEMS accelerometers are assumed to be ideal.

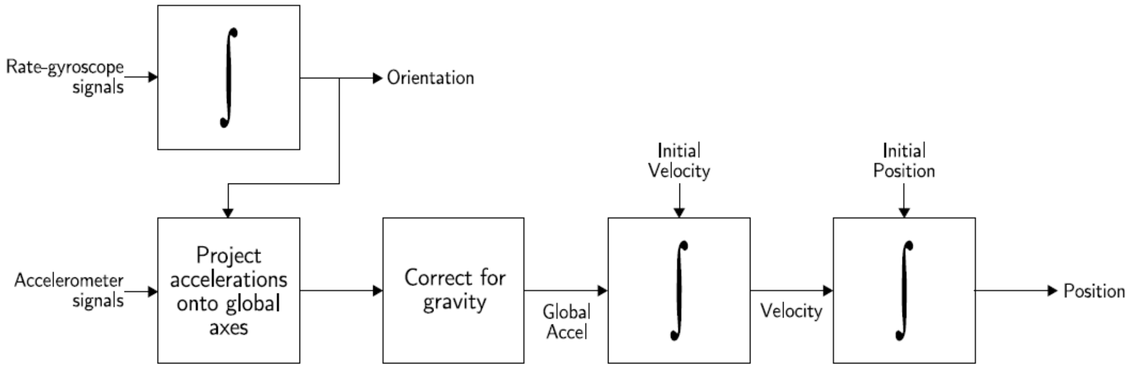

Figure 1.4: A block diagram of the strap-down INS [29].

A block diagram of the strap-down INS is shown in Figure 1.4. In order to compute the position from the angular velocity and acceleration signals, the angular velocity signals are first integrated to produce 3-axis orientation of the navigation system. Because this 3-axis orientation is calculated on the body axes, which are the local axes that represent the relative orientation to the initial orientation, the orientation needs to be projected onto the global axes. In this study, the projection is conducted by the direction cosines method as follows [29]:

$$a_g(t) = C(t) \cdot a_b(t) \tag{1.1}$$

where $a_g(t)$ is the acceleration in the global axes, $C(t)$ is the direction cosines rotation matrix, and $a_b(t)$ is the acceleration in the body axes and can be represented as $a_b(t) = (a_{bx}(t), a_{by}(t), a_{bz}(t))^T$. The direction cosines rotation matrix at time t can be calculated as [29]:

$$C(t) = C(t - \delta t) \cdot (I + sin\alpha/\alpha \cdot B + (1 - cos\sigma/\sigma^2 \cdot B^2)) \tag{1.2}$$

where $\sigma =| \omega_b \delta t |, \omega_b = (\omega_{bx}, \omega_{by}, \omega_{bz})^T$, which are the angular velocities measured by the 3-axis gyroscopes, $B = \begin{pmatrix} 0 & -\omega_{bz}\delta t & \omega_{by}\delta t \\ \omega_{bz}\delta t & 0 & -\omega_{bx}\delta t \\ -\omega_{by}\delta t & \omega_{bx}\delta t & 0 \end{pmatrix}$, and I is a 3 x 3 identity matrix. The accelerations in the global axes that were described in Equation 1.1 can then be subtracted by a gravity matrix, g_g, to make a correction for the gravity factor. The corrected accelerations are then integrated once to calculate the velocities and twice to calculate the positions as follows:

$$v_g(t) = v_g(0) + \int_0^t (a_g(t) - g_g)dt \tag{1.3}$$

$$s_g(t) = s_g(0) + \int_0^t (v_g(t))dt \tag{1.4}$$

where $v_g(0)$ and $s_g(0)$ are the initial velocities and positions, respectively.

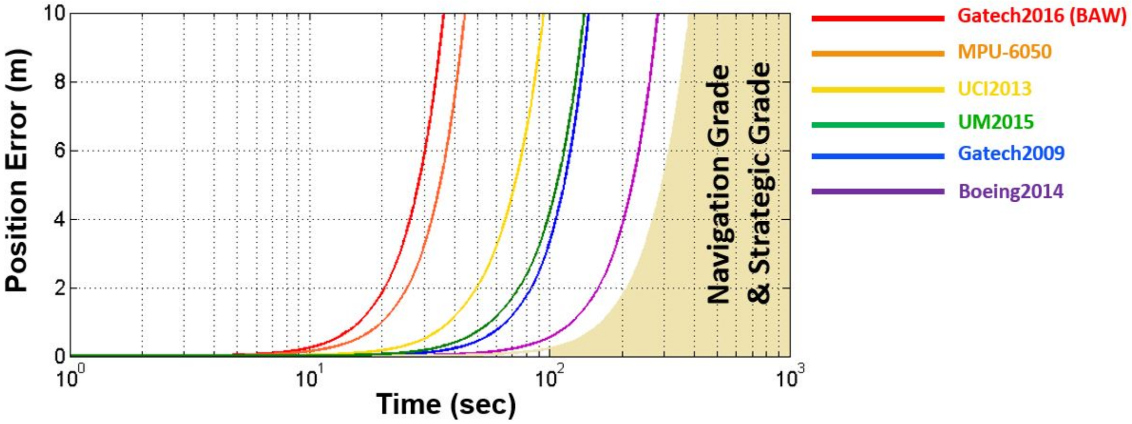

Figure 1.5: Position errors due to noise in the MEMS gyroscopes.

Figure 1.5 shows the position errors of the INS using six state-of-the-art gyroscopes over time. The position error is the Euclidean distance of $s_g(t)$ in Equation 1.4 from the origin, and the position error over time was computed 50 times for each INS.

The repeated measurements were then averaged to produce each plot. As shown, the position error exhibits a rapid growth due to several integral operations in calculating the position from the rate outputs and the accelerations. Furthermore, the shaded area in Figure 1.5 indicates the position error of an INS using navigation- and strategic-grade inertial sensors as a reference. According to the simulation results, Boeing2014 [8] shows the lowest position error over time, followed by Gatech2009 [6], UM2015 [30], UCI2013 [5], MPU-6050 [24], and Gatech2016 [7]. Furthermore, based on the position error plots in Figure 1.5 and the noise performance in Table 1.1, it was found that a gyroscope with a lower BI value produces lower position errors than that with a higher BI value, while a gyroscope with a lower ARW value does not necessarily produce lower position errors than tat with a higher ARW value. Therefore, the BI of the gyroscope is the dominant factor that contributes to the position error.

1.3 Environmental Effects on MEMS Gyroscopes

Although the state-of-the-art MEMS gyroscopes presented in the previous section provide the best performance of all time, one of the remaining challenges is to maintain the good performance in any environment, especially when the sensors are disturbed by temperature, stress, vibration, or shock effects. This section reviews environmental effects on MEMS gyroscopes. INS simulations will be conducted using available temperature sensitivity data of the state-of-the-art MEMS gyroscopes in Table 1.1 to better understand the temperature effect on the INS. Finally, oven-controlled inertial sensors (OCIS) will be introduced as one of the most efficient methods to mitigate environmental effects.

There are two types of errors in the outputs of MEMS gyroscopes: zero-rate output (ZRO) and nonzero-rate output (nZRO) [5, 29]. The ZRO is the existence of a non-zero finite output in the gyroscope when the gyroscope is not subject to angular velocity, and this is sometimes referred to as bias drift. This type of error becomes very problematic and pronounced when the surrounding temperature changes. The nZRO refers to inaccurate output of inertial sensors when the sensors are subject to angular velocity or acceleration, and this type of error is often referred as the scale factor (SF) error. The SF error is also very susceptible to temperature effects [31]. The main causes for the temperature-induced bias drift in MEMS gyroscopes are: 1) changes in material properties of the MEMS gyroscopes including Youngs modulus, 2) temperature dependence of associated driving, sensing, and control electronics [32], and 3) coefficients of thermal expansion (CTE) mismatch between the package and the sensor element [33, 34, 35].

Mechanical stress effect on MEMS gyroscopes is another critical environmental effect, and thus many efforts have been made to address the stress effect on MEMS gyroscope [35, 36, 37]. In general, there are two types of mechanical stress that affect the MEMS gyroscope significantly: strain-induced mechanical stress and temperature-induced mechanical stress.

The strain-induced mechanical stress refers to the stress that is induced by the strain on the substrate on which the MEMS gyroscopes is attached. Since MEMS gyroscopes are generally attached to a PCB, this stress is often called a PCB stress [37]. Because the PCB stress can cause a tremendous impact on the gyroscope performance, some studies developed methods to mitigate PCB stress by using a mechanical stress isolation stage, attaching strain gauges to the substrate, or designing a structure for the MEMS gyroscope that is less sensitive to PCB stress effect (e.g., STMicroś mushroom structure or University of Michigans birdbath shell resonator) [36, 35, 37, 30]. In the method of attaching the strain gauges to the substrate, an additional calibration step will be required for each gyroscope, since the PCB stress effect on the MEMS gyroscope generally varies greatly from sample to sample.

On the other hand, the temperature-induced mechanical stress is the stress that is caused by, but not limited to, coefficient of thermal expansion (CTE) mismatch, and one typical example is the mounting stress [38]. More specifically, in order to attach the MEMS gyroscope to a PCB or any other type of substrate, an intermediate layer needs to be applied between the gyroscope and the substrate, such as solder or glue adhesives. The intermediate layer is then baked and cured at an elevated temperature, and finally cooled down to room temperature. Throughout this process, CTE mismatches among the substrate, intermediate layer, and gyroscope cause mechanical strain on the MEMS gyroscope, which degrades the gyroscope performance significantly. The mounting stress can be minimized by reducing the attachment area or using the substrate, intermediate layer, and gyroscope that are made of the same material or materials that have similar CTEs. Furthermore, since this stress can change when the surrounding temperature changes, and it is difficult to differentiate the temperature-induced stress effect from the pure temperature effect on the MEMS gyroscope, developing a proper compensation method for this stress is not easy.

The third critical environmental effect on MEMS gyroscope is the vibration effect [39]. Generally, this effect can be managed by attaching the MEMS gyroscope on a micro-machined mechanical isolation stage that blocks off mechanical vibrations with a frequency higher than the resonant frequency of the isolation stage [39]. Another effective method to mitigate the vibration effect is to use electrical filters, such as Kalman filter, to block the mechanical vibrations.

The shock impact is the final critical environmental effect on the MEMS gyroscope because this effect can adversely affect the performance of the gyroscope or even cause malfunction and irreversible physical damages. In order to mitigate the shock effect, a specialized structure design for MEMS inertial sensors needs to be developed [40, 41] or a shock-proof packaging technology needs to be used [42].

1.3.1 Temperature Effect on INS using MEMS Inertial Sensors

Since data on environmental effects other than the temperature effect—vibration, shock, and stress—for the state-of-the-art gyroscopes are not available and even the data on the temperature effect is not available for some of the state-of-the-art gyroscopes in the literature, this section discusses temperature effects on the INS using gyroscopes whose temperature sensitivity data could be found in the literature.

In order to understand temperature effects on INS using the state-of-the-art MEMS gyroscopes, the temperature sensitivity data in Table 1.1 was included in the INS simulation model that was developed in Section 1.1. Then, thermal shock with a linear slope of 3 °C/min was induced to the INS simulation model at time = 0 second. The results after the thermal shock was induced are shown in Figure 1.6 where the position errors of the four INS models were degraded significantly from the position errors of the four INS models without the thermal shock. Furthermore, it was found that the INS model using Boeing2014 was the most significantly affected by the thermal shock. In other words, before the thermal shock was induced, the INS model using Boeing2014 took around 300 seconds to reach a position error of 10 m. After the shock was induced, however, it took only 55 seconds to reach the same position error, resulting in 5.5 times degradation. The degradation of the position error in the INS model is more prominent in a higher performing MEMS gyroscope, due to the fact that the temperature sensitivity of the higher performing MEMS gyroscope is only slightly lower than that of a lower performing MEMS gyroscope. For instance, the BI of Boeing2014 is 200 times lower than that of MPU-6050, while the temperature sensitivity of Boeing2014 is only 10 times lower than that of MPU-6050. Therefore, the temperature effect on the INS should be properly managed.

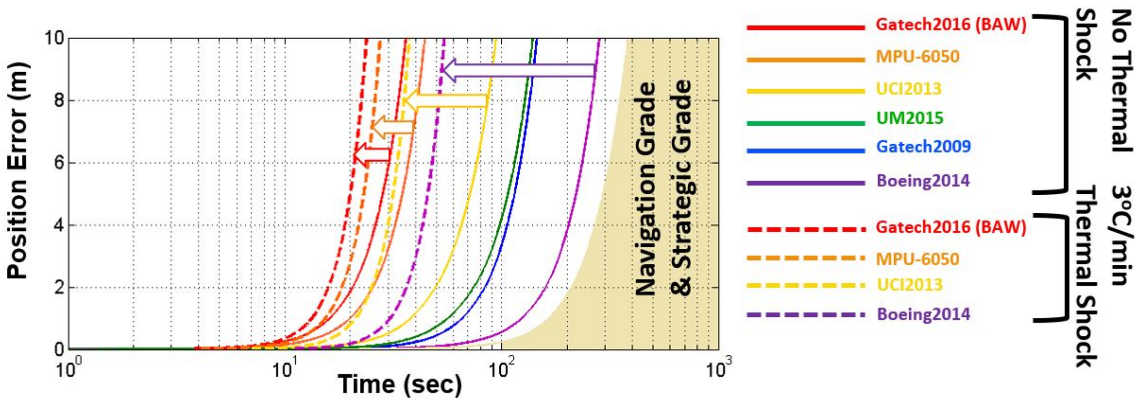

Figure 1.6: Position errors due to random noise and thermal variation in inertial Sensors.

1.3.2 Oven-Controlled Inertial Sensors

A number of methods have been proposed to mitigate temperature effect on MEMS inertial sensors, of which the following three have proven to be the most effective: (a) foreground temperature compensation, (b) background temperature compensation, and (c) oven-control method.

Foreground temperature compensation utilizes the measured temperature and calibration data of the sensor output to electronically correct for sensor output variations due to temperature. As such, it requires that reliable sensor output vs. temperature data is available through one-time calibration process. Although this method has been widely used in commercial applications due to its simple design and low cost, the foreground compensation method alone is usually insufficient to mitigate the temperature-induced bias drift by more than a factor of 10, as the sensor output vs. temperature can vary from the data that was obtained through one-time calibration process after a long-term operation.

On the other hand, background compensation utilizes machine-learning techniques to update measured parameters in real-time, instead of relying on the one-time calibration data, to improve long-term temperature effect on MEMS inertial sensors. However, because of the need for significant signal and data processing, it is usually not suitable in small systems. In addition, the reported performance to date is not as good as any oven-controlled inertial sensors [43].

Finally, the oven-control method utilizes a heated isolation stage whose temperature is actively controlled and kept at a predetermined constant value using a heater and a temperature sensor, in any environment including when the temperature surrounding the stage changes. In this method, the MEMS inertial sensors are attached to the heated isolation stage, and thus they are maintained at a constant temperature. Consequently, the sensor output is expected not to change when the surrounding temperature changes. To date, this method has provided the smallest temperature-induced bias drift among the three approaches discussed here [44].

The oven-control method has been adopted and used for decades in certain applications, including oscillators (oven-controlled crystal oscillator (OCXO)) and timing units. The OCXO has successfully provided very stable performance [45, 46]. However, most existing OCXOs dissipate a large amount of power due to inadequate thermal isolation, which limits their possible applications. In order to design a low power oven-control system, many studies have developed integrated sensor systems with an isolation stage and a vacuum-sealed package [47, 48, 49, 50]. Some of these approaches monolithically integrated resonators that were fabricated in a custom-designed process with an isolation stage and a heater to fabricate an integrated device [47, 48, 49]. Another oven-control approach is using a hybrid attachment method where a resonator and an isolation stage are fabricated separately and they are attached in later steps using a bonding technique [50]. The monolithically integrated resonators have the advantage of having a small size and very high thermal conduction between the local heater and resonator, thus reducing its power dissipation to a few mW [47]. However, this custom approach is useful only for a completely integrated system where the resonator, isolation stage, heater, and temperature sensors are fabricated using the same process. This limits the ranges of applications and resonator designs that can benefit from the oven-control method. In the hybrid attachment method, on the other hand, the oven-control system can accommodate various types of sensors that were fabricated using a different process or are commercial off-the-shelf (COTS) sensors. Therefore, in this thesis, the hybrid attachment oven-control method is adopted for MEMS inertial sensors to make oven-controlled inertial sensors (OCIS) [50].

Furthermore, since the design of the isolation stage in the present study is a crab-leg structure, the OCIS is expected to isolate stress and vibration effects on MEMS inertial sensors as well [50, 44]. Finally, the shock effect can also be mitigated to some extent with a proper design of the OCIS [42].

1.4 Objectives of Research

In this Chapter, a literature review was conducted to understand environmental effects on MEMS gyroscopes, and the INS using the state-of-the-art gyroscopes were modelled to calculate their position errors due to changes in temperature. In the rest of the thesis, two types of OCIS technologies that can effectively mitigate temperature, stress, vibration, and shock effects on MEMS inertial sensors will be presented. The objectives of this study is to:

1) understand available temperature sensing methods for the first type of OCIS technology, a single isolation stage oven-controlled inertial sensor (SOCIS), and finding the most accurate method among those temperature sensing methods. There are three available temperature sensing methods for the SOCIS: a) an on-chip solid-state temperate sensor integrated in the commercial IMU, b) an RTD temperature sensor on the isolation stage, and c) a temperature sensing method based on the temperature coefficient of frequency (TCF) of the resonant frequency of the gyroscope. Each of the

three methods will be used to oven-control MEMS inertial sensors during thermal-cycle tests in an oven-chamber, and the results will be compared to determine which method represents the temperature of the MEMS inertial sensors most accurately.

2) understand the effects of strain-induced stress and temperature-induced stress on the SOCIS. The strain-induced stress is the stress caused by deformation of the substrate on which the SOCIS is attached, while the temperature-induced stress is caused by the temperature gradient and change of the temperature gradient on the isolation stage in the SOCIS during the thermal-cycle test. Each of these two effects will be analyzed through experiments and simulations.

3) understand fundamental limitations of the SOCIS. The two main fundamental limitations of the SOCIS are: a) the temperature-induced stress on the MEMS inertial sensors due to the temperature gradient on the isolation stage, and b) the constrained design flexibility for the isolation stage due to the trade-off between the mechanical and thermal isolation capabilities. These fundamental limitations will be confirmed through experiments and simulations.

4) address the fundamental limitations of the SOCIS by proposing a new double-isolation stage oven-controlled inertial sensor (DOCIS). In the DOCIS, two stages are used to isolate the mechanical and thermal effects from the sensor, instead of a single isolation stage, to eliminate the need for trade-off between the mechanical and thermal isolation capabilities. In this way, the two limitations in the SOCIS can be seperately resolved, providing better overall performance. The first isolation stage in the DOCIS is made of silicon to isolate the mechanical effects and minimize temperature-induced stress on MEMS inertial sensors, while the second isolation stage in the DOCIS is made of polyimide aerogel to produce a high thermal resistance. Experiments and simulations will be followed to validate the advantages of the DOCIS.

5) understand environmental and other non-ideal effects on one of the state-of-the-art gyroscopes, the fused-silica birdbath (BB) shell resonator, and design an oven-

controlled BB shell resonator based on the DOCIS to mitigate its environmental and other non-ideal effects. Short- and long-term performance changes of the shell resonator will be monitored during and after vacuum-sealing process, and the effects of pressure, temperature, stress, shock, and bias voltage on the shell resonator will be analyzed to find the most critical effects on the shell resonator. Finally, the DOCIS technology will be applied to the shell resonator to mitigate these critical effects.

1.5 Thesis Outline

The remaining chapters are described in this section. Chapter II discusses the operating principles and performance enhancement of the SOCIS, including heat transfer analysis of the system, temperature sensing and control methods, compensation algorithms, mechanical stress isolation capability, unexpected high bias drift in Z-axis accelerometers, and position errors of the INS using the SOCIS. Furthermore, challenges and fundamental limitations of the SOCIS are discussed. In Chapter III, the DOCIS is proposed to address the fundamental limitations of the SOCIS, and details of the DOCIS, such as the packaging design, heat transfer analysis of the system, temperature-induced stress on the isolation stage, design flexibility of the mechanical isolation stage, mounting stress, fabrication and assembly steps, and remaining problems, are discussed. In Chapter IV, environmental and non-ideal effects on the BB shell resonator, such as short- and long-term performance changes of the shell resonator during and after the vacuum-sealing process, and the effects of pressure, temperature, stress, shock, and bias voltage on the shell resonator, will be analyzed. Then, the oven-controlled birdbath shell resonator will be proposed and analyzed to mitigate the two most critical effects on the shell resonator, the temperature and shock effects. Finally, in Chapter V, summary, contributions, and recommended future works will be presented.

CHAPTER II

Single Isolation Stage Oven-Controlled Inertial Sensors

In this chapter, details about the single isolation stage oven-controlled inertial sensors (SOCIS), where one isolation stage is used to mitigate both thermal and mechanical effects on MEMS inertial sensors, are presented. The initial design of the SOCIS was presented in [51], and vibration and shock effects on MEMS inertial sensors and potential solutions were discussed in [42]. As a continuing effort, the present study mainly focuses on 1) further understanding heat transfer mechanism in the SOCIS to reduce power consumption of the oven-control system, 2) understanding available temperature sensing and control methods to improve thermal stability of the MEMS inertial sensors, 3) understanding design parameters of the isolation stage to improve the mechanical and thermal isolation capabilities, 4) performance analyses of the SOCIS to validate the improved mechanical and thermal isolation capabilities, and 5) fundamental limitations of the SOCIS.

2.1 Selection Process of Commercial MEMS Inertial Sensors in SOCIS

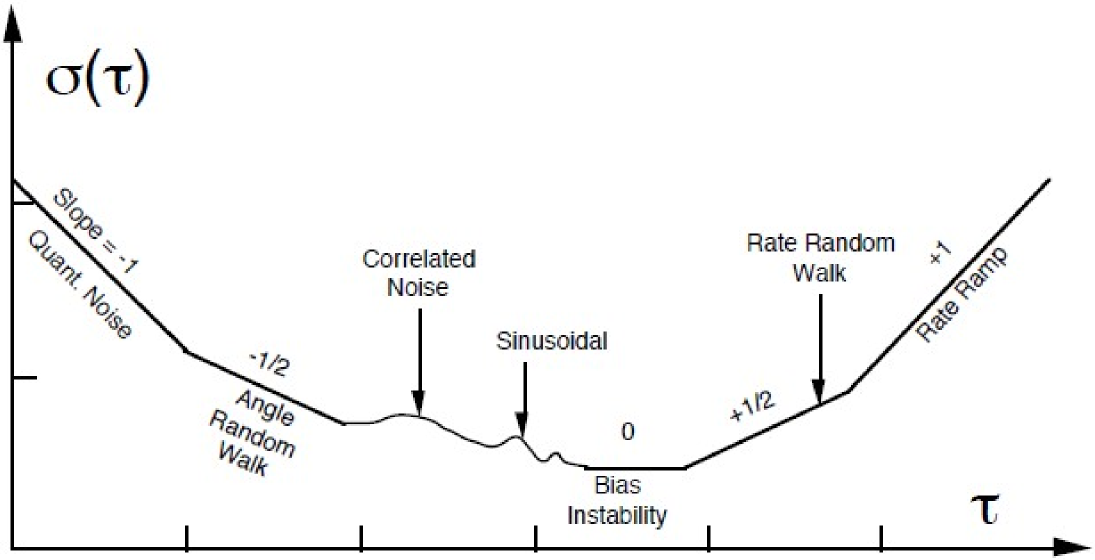

Figure 2.1: ADEV Plot [52].

Prior to designing and fabricating the SOCIS, a selection process of appropriate MEMS inertial sensors for the SOCIS should come first. In order to select the appropriate MEMS inertial sensors, a total of six state-of-the-art commercial inertial measurement units (IMU) were prepared based on the noise performance on the datasheet. The noise characteristics of these IMUs were then measured and compared by collecting the outputs of the IMUs for 24 hours at room temperature and computing the stability of the outputs via Allan Deviation (ADEV). ADEV was first developed by David W. Allan to calculate frequency stability of oscillators. This measure is now widely used to evaluate the noise performance of the inertial sensors including quantization noise, angle random walk, bias instability, rate random walk, and rate ramp, as shown in Figure 2.1 [52].

In order to compute ADEV values of N consecutive data that has a sampling time of τ_0, the data is first grouped into clusters that have the same length of time, τ, and the number of data, n, where n < N/2. The average of each cluster is then calculated as [53]:

$$\overline{X}_{k,\tau} = \frac{1}{\tau} \int\limits_{t_k}^{t_k+\tau} X(t)dt \tag{2.1}$$

where $\overline{X}_{k,\tau}$ is the average of kth cluster having a time length of τ, and $X(t)$ is an output of an inertial sensor at time $= t$. After then, difference between the averages of two adjacent clusters are calculated as [53]:

$$\delta t_k = \overline{X}_{k+1,\tau} - \overline{X}_{k,\tau}. \tag{2.2}$$

By using this difference, the Allan variance (AVAR) of the data can be calculated as [53]:

$$\sigma_\tau^2 = \frac{1}{2(N-2n)} \sum_{k=1}^{N-2n} \delta t_k^2. \tag{2.3}$$

Finally, ADEV can be calculated as [53]:

$$\sigma_\tau = \sqrt{\frac{1}{2(N-2n)} \sum_{k=1}^{N-2n} \delta t_k^2}. \tag{2.4}$$

Calculation of the ADEV value is repeated for each of the time lengths of $\tau = n \cdot \tau_0$, where $n = 1, 2, 3, \ldots$ For computational simplicity, the ADEV values can be calculated for the time lengths of $n = 2^i$, where i=1, 2, 3, ... with a comparable accuracy [54].

The ADEV values are then plotted as τ increases to half of the total measurement time where two averaged clusters are used to calculate the ADEV. Based on the ADEV plot, the level of each noise source can be identified as follows. If the ADEV decreases at the rate (slope) of -1 as τ increases, or $\sigma_{\mathcal{T}} \propto \tau^{-1}$, then this represents that the dominant noise in the output of the inertial sensor is quantization noise—the noise that is generated from a finite number of bits in the analog-to-digital converter (ADC) in the read-out circuits. In the ADEV plot, the quantization noise is normally found when τ is much shorter than 1 second, and its unit is ° for the gyroscopes and m/s for the accelerometers. Likewise, if the decreasing rate (slope) of the ADEV plot is -1/2, or $\sigma_{\mathcal{T}} \propto \tau^{-\frac{1}{2}}$, then this represents that the dominant noise in the output of the inertial sensor is white noise. The level of white noise in the inertial sensor is normally specified as angle random walk (ARW) for gyroscopes and as velocity random walk (VRW) for accelerometers. It is called angle random walk for gyroscopes because the integral of the white noise in angular velocity becomes random walk noise (i.e., Brownian noise) in angle. Similarly, it is the velocity random walk for accelerometers because the integral of the white noise in acceleration becomes random walk noise (i.e., Brownian noise) in velocity. ARW and VRW values can be obtained from the ADEV plot by reading the ADEV value at $\tau = 1$ second [54]. $^\circ/\sqrt{hr}$ and $^\circ/sec/\sqrt{Hz}$ are interchangeably used as a unit for ARW and one can be converted to the other as:

$$1^\circ/s/\sqrt{Hz} = 60^\circ/\sqrt{hr}. \tag{2.5}$$

Similarly, $g/\sqrt{Hz}$ and $m/s^{3/2}$ are interchangeably used as a unit for VRW and the conversion can be done as:

$$1g/\sqrt{Hz} = 9.8m/s^{3/2}. \tag{2.6}$$

If the ADEV stays at a constant value as τ increases (i.e., the slop becomes zero), it represents that the flicker noise in the read-out electronics and inertial sensors is the dominant noise source. For MEMS inertial sensors, the flicker noise becomes a dominant noise source when τ is tens to hundreds of seconds, or even over a thousand seconds depending on the noise level of the sensors. The ADEV value when the slope is zero is called the bias instability (BI) and specified in °/hr for gyroscopes and g or m/s^2 for accelerometers. BI is a very important noise metric to compare performances of inertial sensors, since it significantly affects the position error of an inertial navigation system (INS), as discussed in Chapter I.

The next noise that can be identified in the ADEV plot of inertial sensors is the rate random walk (RRW) for gyroscopes and the acceleration random walk (AcRW) for accelerometers [55]. The RRW is the random walk noise that appears in the outputs of rate gyroscopes, while the AcRW is the random walk noise that appears in the outputs of accelerometers. This type of noise normally indicates inherent Brownian noise in the inertial sensors. If this noise dominates, the ADEV value will increase at the rate of $+1/2$ as τ increases, and the units are $^\circ/hr^{3/2}$ for the RRW and $m/s^{5/2}$ for the AcRW. Although this noise is not considered as important as ARW/VRW and BI, and thus not specified in commercial datasheets nor technical papers, it could inflict a long-term bias drift on the inertial sensors.

The last non-ideal source that can be identified in the ADEV plot is the rate ramp (RR) for gyroscopes and the acceleration ramp (AcR) for accelerometers. RR and AcR normally indicate the outputs that are correlated to environmental effects, such as temperature change, and the ADEV value will increase at the rate of $+1$ as τ increases, if this noise source dominates. The units for RR and AcR are $^\circ/hr^2$ and m/s^3, respectively. In an ideal test setup for performance evaluation of inertial sensors, the environmental effects are strictly controlled so that RR or AcR do not interfere with other noise sources. Therefore, instead of calculating this value from the ADEV plot, a separate test is conducted to measure the temperature sensitivity of the outputs of the gyroscopes and the accelerometers, and specified in $^\circ/hr/^\circ C$ and $g/^\circ C$, respectively. Table 2.1 summarizes the noise sources for the gyroscopes

Table 2.1: Noise sources for the gyroscopes and accelerometers.

Noise Source	**Gyroscope**	**Accelerometer**
Quantization Noise	Quant. Noise (°)	Quant. Noise (m/s)
White Noise	ARW ($°/\sqrt{hr}$)	VRW ($g/\sqrt{Hz}$)
Flicker Noise	BI (°/hr)	BI (g)
Brownian Noise	RRW ($°/hr^{3/2}$)	AcRW ($m/s^{5/2}$)
Environmental Effects	RR ($°/hr^2$)	AcR (m/s^3)

and accelerometers, and their units.

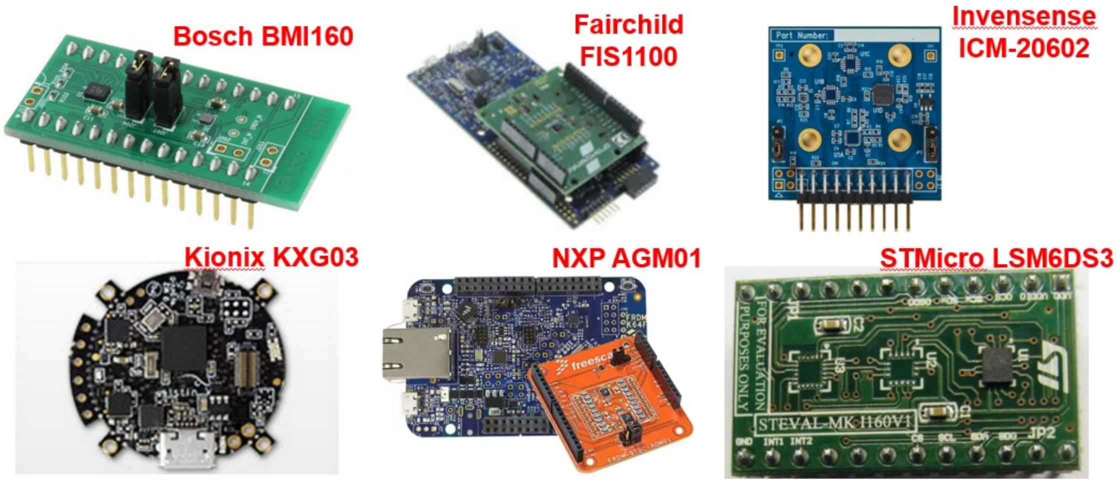

Figure 2.2: Commercial inertial measurement units.

Figure 2.2 shows the six state-of-the-art commercial MEMS inertial sensors: Bosch BMI 160, Fairchild FIS1100, Invensense MPU-6050, Kionix KXG03, NXP AGM01, and STMicro LSM6DS3. They are all 6-axis inertial measurement units (IMUs) consisting of 3-axis gyroscopes and 3-axis accelerometers. In the selection process, only the two most commonly used metrics—ARW/VRW and BI—were computed and compared. In order to compute ARW/VRW and BI from the ADEV plot, outputs of each IMU were collected at room temperature for 24 hours, and the ADEV values for each IMU were then plotted as shown in Figure 2.3. ARW/VRW and BI values of these IMUs are summarized in Table 2.2.

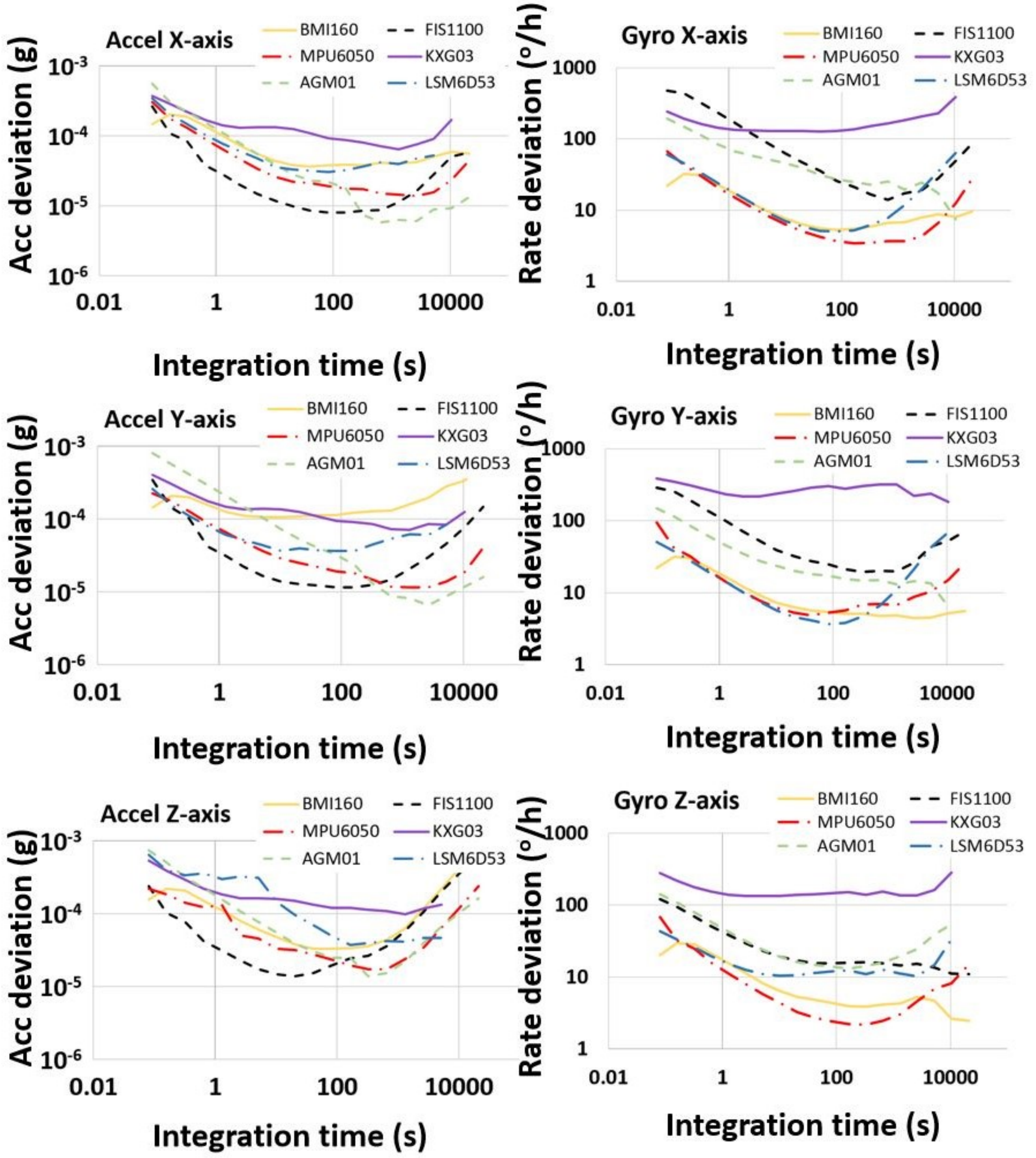

Figure 2.3: ADEV plots for commercial IMUs.

Table 2.2: Commercial IMUs Noise Performance Comparison.

Evaluated IMU	3-axis Gyroscopes		3-axis Accelerometers	
	ARW ($^\circ/\sqrt{hr}$)	BI ($^\circ/hr$)	VRW ($\mu g/\sqrt{Hz}$)	BI (μg)
Bosch BMI 160	0.32, 0.32, 0.30	5.3, 4.4, 3.9	116, 139, 129	36.1, 105, 32.9
Fairchild FIS1100	2.9, 1.7, 0.65	14, 19, 11	28.4, 31.4, 31.7	8.04, 11.6, 14.0
Invensense MPU6050	0.22, 0.23, 0.21	4.8, 3.8, 1.9	150, 150, 220	21.0, 22.0, 29.0
Kionix KXG03	2.5, 4.8, 2.7	130, 220, 130	190, 200, 253	63.6, 70.3, 98.1
NXP AGM01	1.6, 1.2, 1.1	19, 13, 13	127, 243, 184	6.51, 6.73, 8.02
STMicro LSM6DS3	0.47, 0.39, 0.37	5.0, 3.7, 10	123, 93.6, 349	30.2, 36.3, 37.7

According to the inertial sensor performance grade in Figure 1.1, assuming that there were no environmental effects on the inertial sensors, all accelerometers of the six IMUs are either navigation- or strategic-grade, while the gyroscopes of these IMUs are lower-grade ranging from inertial AHRS-grade to flight control-grade. As a result, most position errors in the strap-down INS occur due to the errors in the gyroscopes [29]. Therefore, as this IMU that provides the best gyroscope performance of all, Invensense MPU-6050 was selected in designing the SOCIS.

2.2 Power Consumption

Since the SOCIS has to provide heat energy to the MEMS inertial sensors continuously to control the temperature at a constant value, it normally consumes larger power that other temperature compensation techniques, mostly hundreds of mW to even above 1 W [48, 49]. Therefore, it is critical to reduce the power consumption of the SOCIS. In efforts to reduce the power consumption, two approaches are introduced in this section—heat transfer analysis and control techniques.

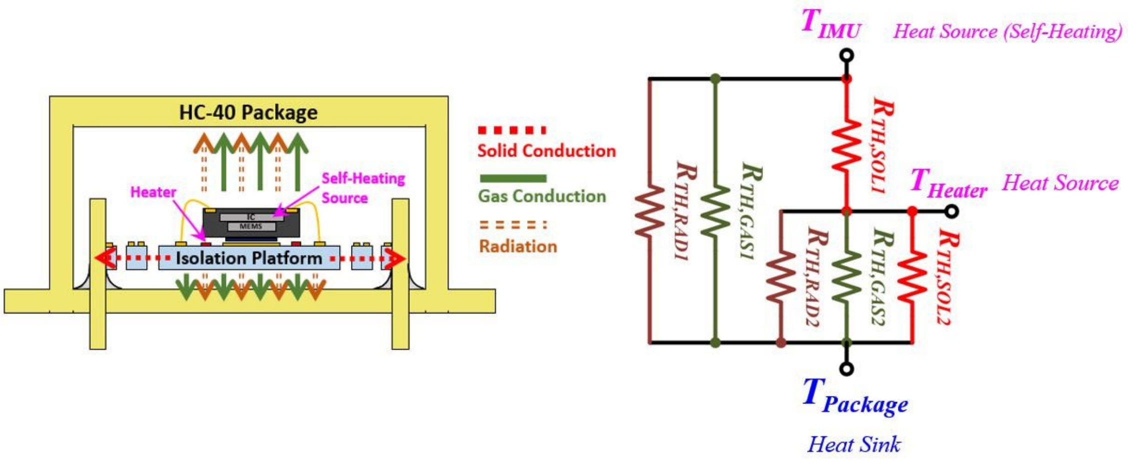

Figure 2.4: Single isolation stage oven-controlled inertial sensors (SOCIS) and the equivalent thermal circuit model.

2.2.1 Reduction in Power Consumption Through Heat Transfer Analysis in SOCIS

Figure 2.4 shows the cross-section and the equivalent thermal circuit model of the SOCIS [44]. Because we are interested in the steady-state analysis, the thermal circuit consists of thermal resistors only. Furthermore, heat is dissipated from two heat sources—a heater on the isolation stage and the integrated circuit in MPU-6050—to the surrounding environment through solid conduction, gas conduction, and radiation.

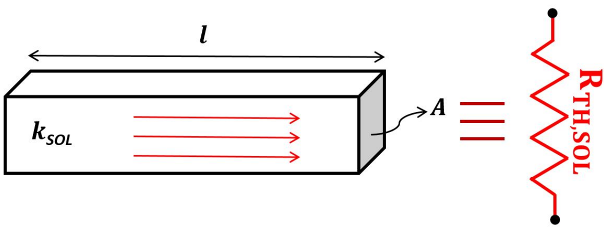

Figure 2.5: Thermal resistance through solid material.

Solid conduction refers to heat transfer due to the existence of a temperature gradient across a solid object. The degree of heat transfer is determined by thermal property and geometry of the solid object, and the thermal resistance of a simple beam structure shown in Figure 2.5 can be calculated as:

$$R_{SOL} = l/k_{SOL} \cdot A \tag{2.7}$$

where R_{SOL} and k_{SOL} are the thermal resistance and thermal conductivity of the beam structure, respectively, and l and A are the length and the cross-sectional area of the structure. According to this equation, in order to maximize the thermal resistance through solid heat conduction, the beam structure should be long, thin, and narrow, and made of a material that has low thermal conductivity. One typical example is a crab-leg isolation stage shown in Figure 2.6 where the thermal resistance is maximized by forming four long, thin, and narrow beams made of glass [51]. One consideration in the design of the crab-leg isolation stage is that if the beams are made extremely long, thin, and narrow for better thermal isolation, the stage might become susceptible to breakage and other mechanical effects. Therefore, appropriate design parameters will need to be selected.

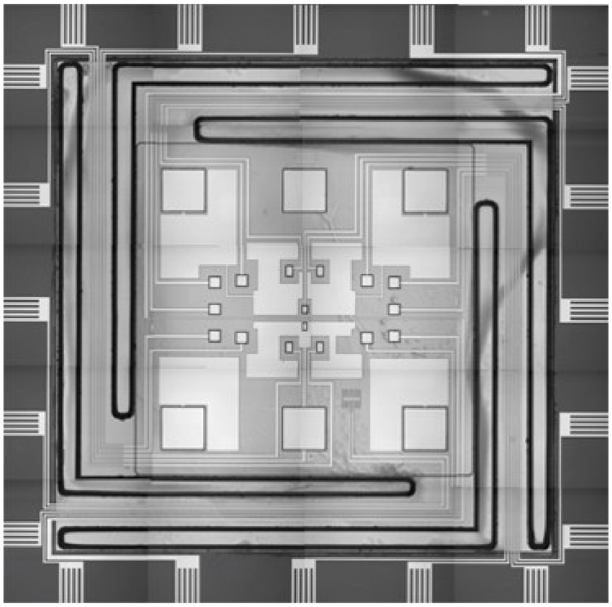

Figure 2.6: A crab-leg isolation stage [51].

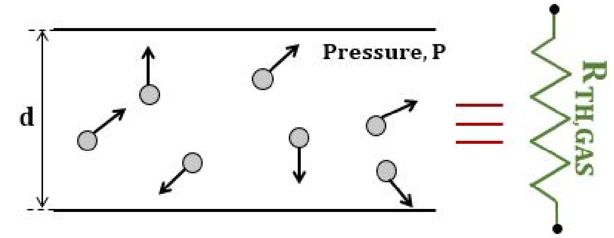

Figure 2.7: Thermal resistance through gas conduction.

Next, a large amount of heat dissipation can also occur through gas conduction in the SOCIS. In general, if the inertial sensors are vacuum-sealed in a package and the vacuum level in the package is sub-mTorr, the heat dissipation through gas conduction will be negligible [51]. However, in certain cases where the MEMS inertial sensors are integrated with a silicon integrated circuit (IC) die that consumes tens of mWs of power, it is not desirable to vacuum-seal the inertial sensors at too low-pressure level [44]. In other words, the self-heating, which is generated by the silicon IC die, could become a significant heat source when the pressure in the package is too low. For instance, at a pressure level in sub-mTorr, thermal resistance through gas conduction may be higher than 10,000 K/W depending on the package size [51]. This means that the self-heating will raise the temperature of the sensors by more than 100 °C when the silicon IC die consumes 10 mW, and thus temperature set point for the SOCIS has to be 185 °C or higher to operate in the commercial temperature span (-40 to 85 °C). As a result, the high operating temperature may cause problems in the MEMS inertial sensors including malfunction of the sensors or degraded noise performance [5]. Therefore, an appropriate level of pressure in the package has to be determined based on self-heating to control the sensors at a reasonable temperature. For the pressure level of tens of mTorr and cm-size cavity having the geometry as shown in Figure 2.7, the Low-Pressure theory can be used for accurate calculation of the thermal conductivity through gas conduction (k_{GAS}) as follows [56]:

$$k_{GAS} = k_{GAS,0} \cdot \frac{1}{1 + \frac{c}{PP}} \tag{2.8}$$

where $k_{GAS,0}$ represents the thermal conductivity of gas at atmosphere pressure levels; c is a constant equal to $7.6 \cdot 10^{-5} m \cdot K/N$; and PP is a pressure parameter, which is defined as:

$$PP = \frac{P \cdot d}{T} \tag{2.9}$$

where P is the pressure in Pa; d is the distance between the isolation stage and the package in m; and T is the temperature in Kelvin. Even when the pressure parameter is much smaller than $10^4 N/m \cdot K$ where the free molecule theory is normally used, this simple equation should give quite accurate estimate [56]. The thermal resistance through gas conduction is then calculated by using Equation 2.7. Gas convection can be ignored in this case, since the package is fully sealed.

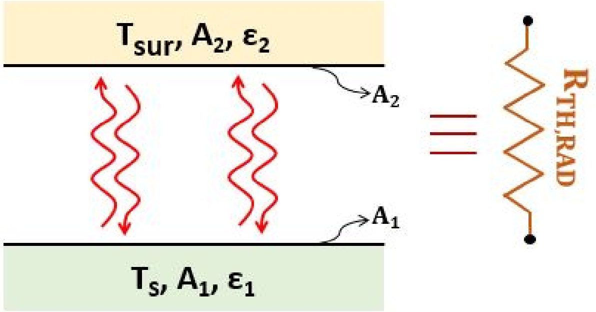

Figure 2.8: Thermal resistance through radiation.

Finally, heat dissipation also occurs through radiation in the SOCIS. In this mechanism, heat is transferred through electromagnetic waves, which does not require a medium. A simplified equation for calculating thermal resistance due to heat dissipation through radiation between two walls having the same view factor would be [51]:

$$R_{TH,RAD} = \frac{\epsilon_1^{-1} + \epsilon_2^{-1} - 1}{\sigma \cdot A \cdot (T_s + T_{sur}) \cdot (T_s^2 - T_{sur}^2)} \tag{2.10}$$

where ϵ_1 and ϵ_2 are emissivities of the sensors and the package in W/m^2; T_s and T_{sur} are absolute surface temperatures of the sensor and the oven-control package in Kelvin, respectively; A is the area of the sensors and the package, which are assumed to be equal; and σ is the Stefan-Boltzmann constant, $5.56 \cdot 10^8 W/m^2 \cdot K^4$. According to Equation 2.10, heat loss through radiation becomes significant as the temperature difference between the sensors and the package increases. This can be a problem for the SOCIS where the temperature difference can be as high as 120 °C or even higher. One way to reduce this radiation loss is to increase ϵ_2^{-1} by using a material with very low emissivity for the package, such as polished aluminum or gold. Practically, metal packages or metal-coated leadless chip carriers (LCC) can be used for this purpose.

Based on the equivalent thermal circuit model in Figure 2.1, the total thermal resistance between the sensors and the package shell can be calculated as:

$$R_{TOT} = (R_{GAS1} \parallel R_{RAD1}) \parallel (R_{SOL1} + R_{SOL2} \parallel R_{GAS2} \parallel R_{RAD2}) \tag{2.11}$$

where R_{TOT} is the total equivalent thermal resistance between the IMU and the shell; $R_{TH,SOL1}$ and $R_{TH,SOL2}$ are thermal resistances through solid conduction between the IMU and the heater and between the heater and the package shell, respectively, $R_{TH,GAS1}$ and $R_{TH,GAS2}$ are thermal resistances due to gas conduction between the IMU and the package shell and between the heater and the package shell, respectively, and $R_{TH,RAD1}$ and $R_{TH,RAD2}$ are thermal resistances due to the radiation between the IMU and the package shell, and between the heater and the package shell, respectively. Because most thermal resistors are connected in parallel, heat loss will be dominated by a path that has the smallest thermal resistance. For example, the heat loss will be dominated by gas conduction at high pressure, while heat loss through gas conduction will become negligible and solid conduction and radiation will be the dominant heat transfer paths below certain pressure.

Considering much smaller cavity size below the isolation stage than above the IMU (i.e. $R_{TH,GAS1} \gg R_{TH,GAS2}$), high solid thermal conduction from the heater to the IMU (i.e. small $\mathrm{R}_{TH,SOL1}$), and high reflectivity (or low-emissivity) of the metal package (i.e. large $\mathrm{R}_{TH,RAD1}$ and $\mathrm{R}_{TH,RAD2}$), we can approximate the total thermal resistance from Equation 2.11 to be:

$$R_{TOT} \approxeq R_{SOL1} + (R_{SOL2} \parallel R_{GAS2}) \tag{2.12}$$

In order to calculate the second term in Equation 2.12, $R_{TH,GAS2}$ and $R_{TH,SOL2}$ are first calculated by using Equation 2.13 and Equation 2.14. Each of the thermal resistances is then plotted over pressure as shown in Figure 2.9. As shown in the plot, $R_{TH,GAS2}$ is inversely proportional to pressure while $R_{TH,SOL2}$ does not depend on pressure. Furthermore, when the pressure level is higher than 100 mTorr, $R_{TH,GAS2}$ is much smaller than $R_{TH,SOL2}$, which makes this pressure region to be dominated by gas conduction. On the other hand, when the pressure level is below 5 mTorr, the thermal resistance through gas conduction becomes significantly larger than that through solid conduction. Therefore, the region where the pressure level is lower than 5 mTorr becomes dominated by solid conduction. Pressure levels between these two extreme regions will be dominated by both gas and solid conductions. Finally, calculated total thermal resistance (i.e., R_{TOT}) is plotted and compared with actual measurements in Figure 2.10.

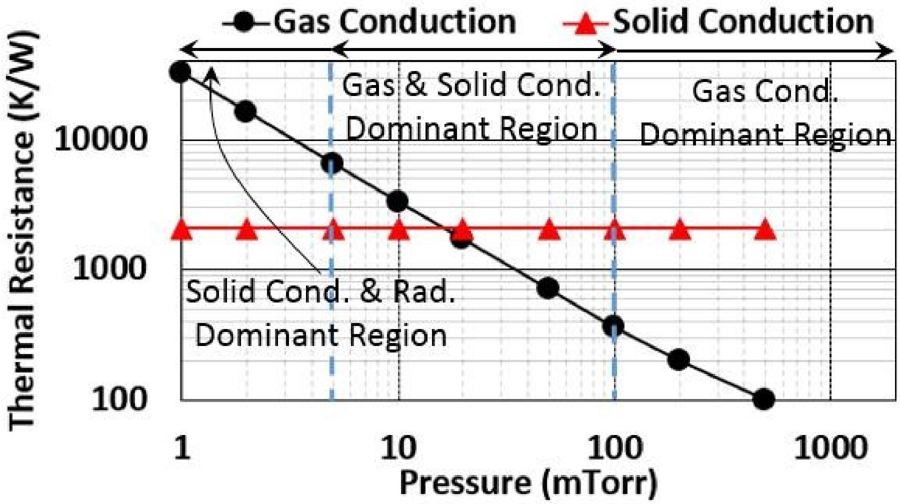

Figure 2.9: Calculated thermal resistances through gas and solid conductions at different pressure levels. Temperature was maintained at room temperature (300K).

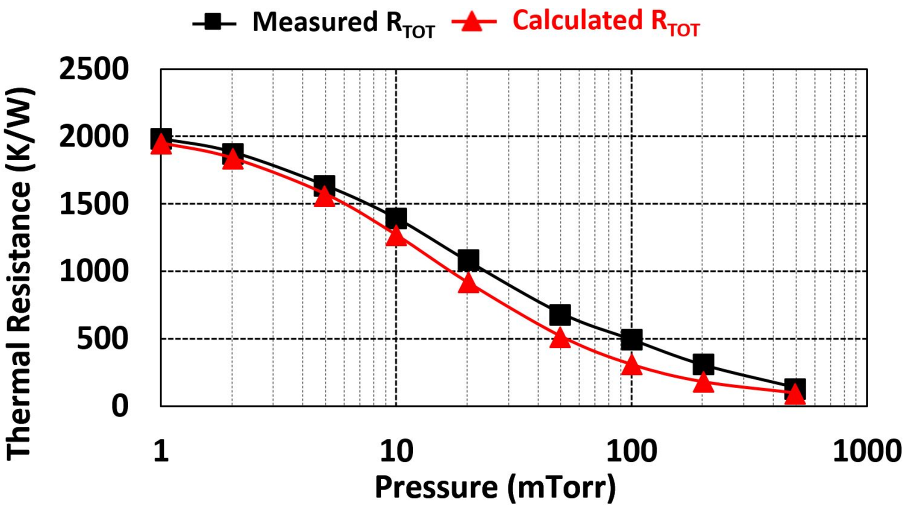

Figure 2.10: Calculated total thermal resistance using Equation 2.12 and measured total thermal resistance of the SOCIS

2.2.2 Reduction in Power Consumption Using Control Techniques

In addition to the reduction in power consumption of the SOCIS through a heat transfer analysis, a further reduction in power consumption can be achieved by using more efficient oven-control techniques. In this section, therefore, we will introduce and discuss two efficient oven-control techniques for the SOCIS: pulse width modulation (PWM)-based oven-control technique and multiple set point (MSP) oven-control technique.

2.2.2.1 PWM-Based Oven-Control Technique

Pulse width modulation (PWM) is one of the modulation techniques that changes pulse width (or duty cycle) of an output square wave signal (or a carrier signal) according to an input analog signal. The output signal of PWM has a fixed amplitude and frequency. The output signal can be represented as:

$$f(t) = A_0 + \sum_{n=1}^{\infty}[A_n \cdot cos(\frac{2n \cdot \pi \cdot t}{T})] \tag{2.13}$$

$$A_0 = a \cdot d \tag{2.14}$$

and

$$A_n = a \cdot \frac{1}{n \cdot \pi}[sin(n \cdot \pi \cdot d) - sin(2n \cdot \pi(1 - \frac{d}{2}))] \tag{2.15}$$

where a and d denote the amplitude and the duty cycle of the PWM signal $f(t)$, respectively, and A_0 and A_n are the DC component and the amplitude of the harmonic functions of the PWM carrier signal. The analog DC output signal ranges from 0 to a, which can be controlled by selecting an appropriate duty cycle. Because only the DC component is useful information for a PWM system, the harmonics (A_n) can be removed by a low-pass filter that has a cut-off frequency lower than the carrier frequency.

One advantage of the PWM system is that it can reduce power loss in a power transistor due to its digital-based operation in which the transistor operates as a switch. When the power transistor is turned off, no current will flow through the transistor. Similarly, when the transistor is turned on and the power is transferred to a load, there will be a very small voltage drop across the transistor. Therefore, power losses in both cases will be negligible that the power consumption will be reduced.

Practically, the stability of the filtered PWM output is limited by two factors. The first factor is the quantization noise from a duty cycle controller in the PWM system. The PWM duty cycle controller generates phase-modulated outputs, and the resolution of the duty cycle is determined by the resolution of a frequency counter in the system. Therefore, a higher resolution will generate smaller quantization noise and thus higher stability of the filtered PWM output. Furthermore, this resolution can be somewhat enhanced by a PID controller in the oven-control system, which produces the input to the PWM duty cycle controller, because the PID controller accumulates historic errors and therefore inherently dithers the quantization noise to enhance the resolution of the PWM duty cycle controller.

The second factor is the peak-to-peak ripple voltage due to unfiltered harmonics. Although most of the harmonics in Equation 2.13 are filtered by using a low pass filter, some harmonics will still remain in the signal. Designing a higher-order low-pass filter (i.e., higher stop-band roll-off) can be a method to reduce the harmonics. However, increasing the stop-band roll-off generally requires a more complex analog filter circuit. Fortunately, the present SOCIS would not be so much limited by the ripple voltage, as the time constant of the equivalent thermal circuit inside the vacuum-sealed package is long enough, such that the package itself will work as a good low pass filter. Therefore, the harmonic ripple voltage will not be a big concern in the SOCIS.

Figure 2.11 shows the overall schematic of the PWM-based oven-control system. In this control system, an Invensense MPU-6050 is oven-controlled by using an on-chip solid-state temperature sensor, a thin-film gold heater on the isolation stage, a PID controller, a PWM duty cycle controller, and a heater driving circuit. The PID controller calculates the input value to the PWM duty cycle controller ($V(t)$) based on the temperature difference between the temperature sensor and the set point temperature ($e(t)$). After then, the duty cycle is adjusted in the PWM duty cycle controller to control the heater driving circuit ($V_{PWM}(t)$), and finally to provide an appropriate amount of current to the heater.

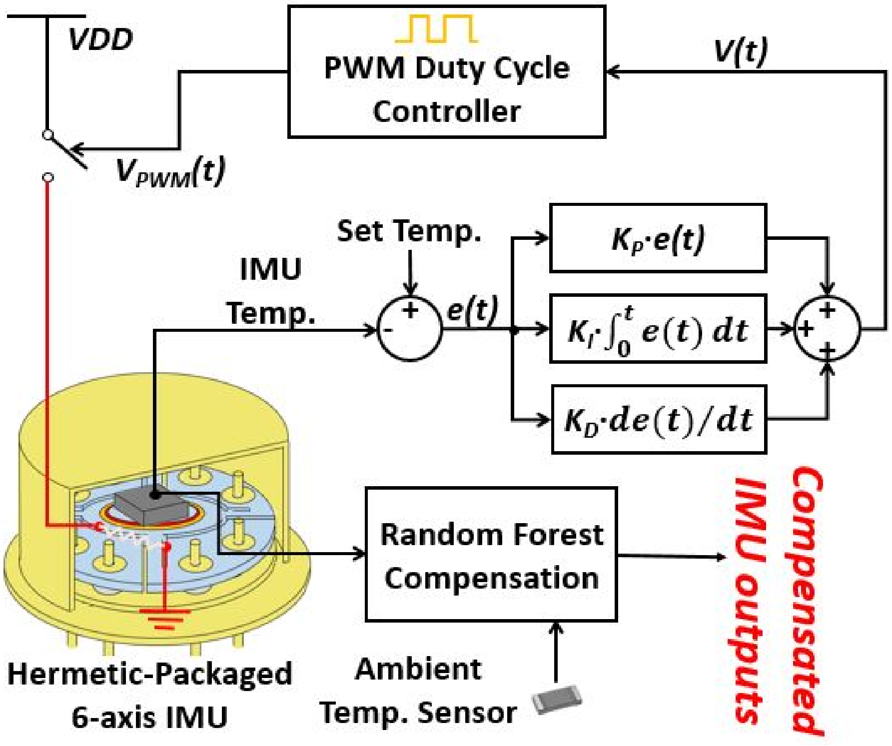

Figure 2.11: Schematic of the PWM-based oven-control system.

The PWM-based oven-control system was fabricated and assembled on a single printed circuit board (PCB) measuring 42 mm × 42 mm × 10 mm, as shown in Figure 2.13. The SOCIS was vacuum-sealed inside an HC-40 TO package, the PID controller and the PWM duty cycle controller were implemented on a microcontroller, Teensy 3.2, to control the IMU temperature, and the heater-driving circuit in Figure 2.12 was assembled on the PCB. Finally, an ambient temperature sensor was assembled on the PCB to measure the surrounding temperature.

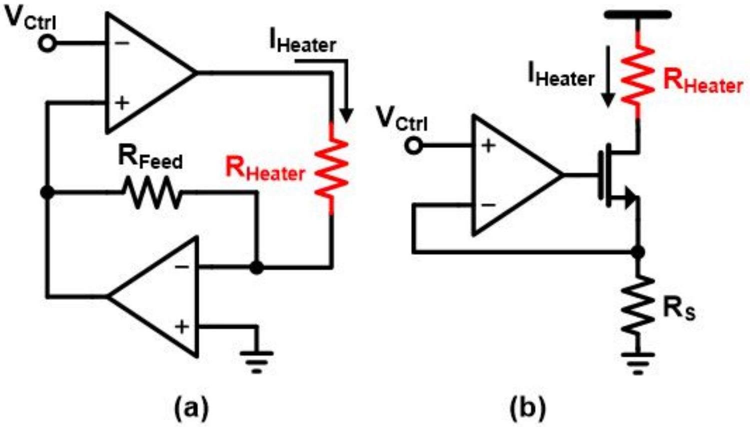

Figure 2.12: A heater-driving circuit using a regulated amplifier and a power transistor [49].

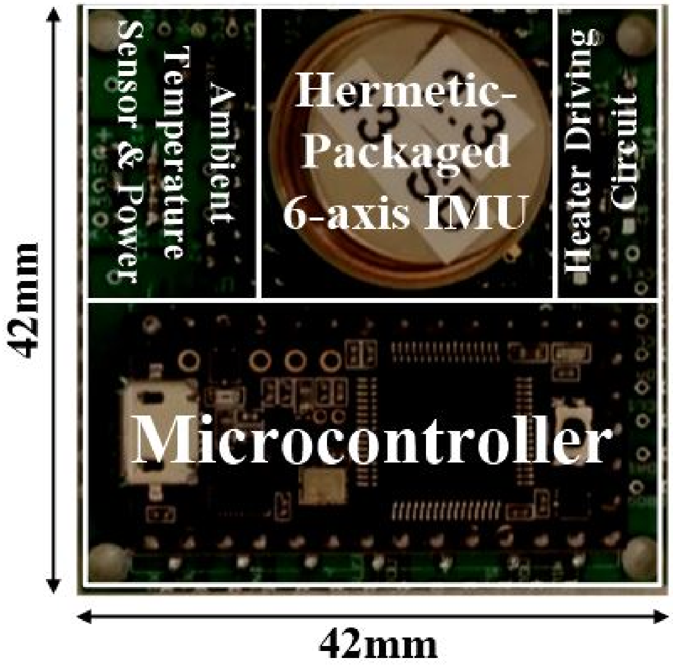

Figure 2.13: PWM-based SOCIS on a single PCB.

In order to quantify the efficiency of the PWM-based oven-control system, power consumption of the heater-driving circuit in the PWM-based oven-control system was measured and compared with that of the previous analog-based oven-control system.

In this comparison, an identical SOCIS was controlled at 92 °C. As a result, the power efficiency of the oven-control system was improved from 53% to 94.4%.

Furthermore, the noise performance of the SOCIS and thermal stability of the oven-control systems were measured to ensure that the PWM-based controller does not introduce additional noise or instability to the system. From the measurement results shown in Table 2.3, it was verified that the noise performance and the thermal stability are almost identical for both the PWM-based and analog-based oven-control systems.

Table 2.3: Performance comparison of two driving schemes.

Driving Scheme	Gyro ARW (deg/sqrthr)	Accel VRW (ug/sqrtHz)	IMU temperature stability (mK)	Power (mW)
Analog (Fig 2b)	0.247	194	7.8	127.38 (53%)
Digital (PWM)	0.250	193	7.5	70.95 (94.4%)

In addition, in order to find if the PWM-based oven-control system is as stable as the analog-based oven-control system when the surrounding temperature changes, a thermal-cycle test was conducted over the industrial temperature span (-40 to 85 °C) inside an oven chamber (SH-240 by ESPEC). The rate of the change of the temperature was 1 °C/min, and the IMU temperature was controlled to 92 °C during the thermal-cycle test. The IMU temperature was observed from the on-chip solid-state temperature sensor and the resonant frequency of an X-axis gyroscope in the IMU during the thermal-cycle test. The IMU temperature measured from the temperature sensor is shown in Figure 2.14, in which the stability of the IMU temperature (1 σ) was found to be 7.5 mK. Such stability is comparable to that of the analog-based oven-control system where the stability was found to be 7.8 mK during the thermal-cycle test. Finally, the PWM-based oven-control system reduced the drift of the resonant frequency of the X-axis gyroscope from ±1900 ppm to ±1.8 ppm over the commercial temperature span (Figure 2.15), which is also comparable to the reduction in the drift of the resonant frequency of the X-axis gyroscope in the analog-based oven-control system [57].

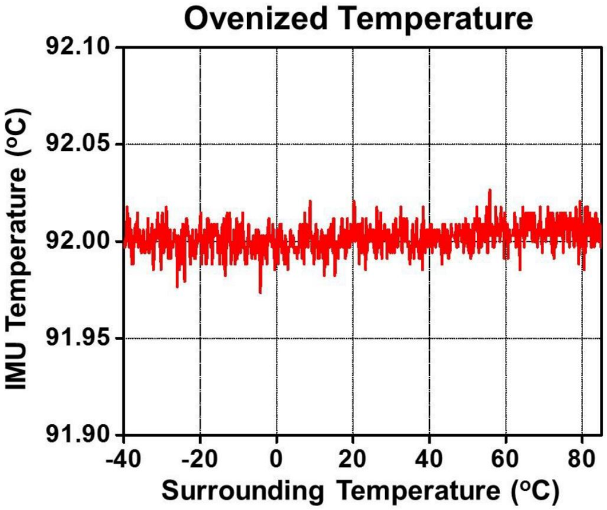

Figure 2.14: Measured temperature of the PWM-based SOCIS during thermal-cycle.

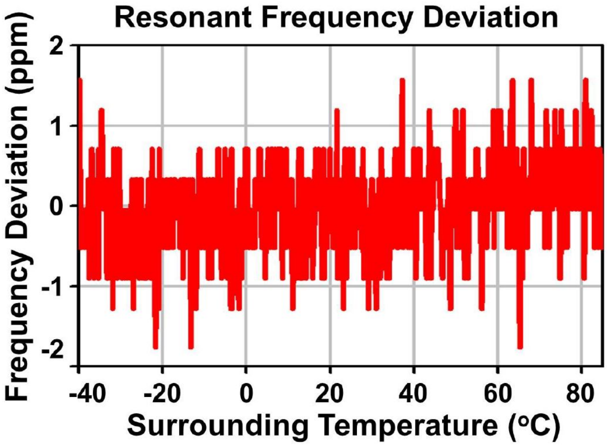

Figure 2.15: Measured resonant frequency of an X-axis gyroscope in the PWM-based SOCIS during thermal-cycle.

2.2.2.2 MSP Oven-Control Technique

Another control technique for reducing power consumption of the SOCIS is the multiple set point (MSP) oven-control technique where the temperature set point is adjusted according to the surrounding temperature. In this technique, the temperature set point is adjusted in a manner that the temperature difference between the temperature set point and the surrounding temperature (i.e., Δ temperature) is significantly lower than Δ temperature in the conventional, single set point (SSP) oven-control technique, where the temperature set point is invariant at all times [58]. For instance, if the surrounding temperature is expected to change from -40 °C to 85 °C, then the temperature set point in the SSP technique has to be 85 °C or higher even when the surrounding temperature is -40 °C; however, in the MSP technique, power consumption at -40 °C can be significantly reduced by lowering the set temperature to a much lower value, say 5 °C, instead of 85 °C. Flow chart of the MSP oven-control system is shown in Figure 2.16 and the equation is:

$$T_{set}(t+\delta t) = \begin{cases} T_{set}(t) + T_{step} & \begin{aligned} if \quad T_{sur}(t+\delta t) > T_{sur}(t), \\ T_{set}(t) < T_{sur}(t) + T_{min}, \\ |T_{IMU}(t) - T_{set}(t)| < 2^{\circ}C \end{aligned} \\ \\ T_{set}(t) - T_{step} & \begin{aligned} if \quad T_{sur}(t+\delta t) < T_{sur}(t), \\ T_{set}(t) > T_{sur}(t) + T_{max}, \\ |T_{IMU}(t) - T_{set}(t)| < 2^{\circ}C \end{aligned} \end{cases} \tag{2.16}$$

where $0 < T_{min} < T_{step} < T_{max}$, $T_{SelfHeating} < T_{min}$, $T_{min} + T_{step} < T_{max}$, T_{IMU} is the temperature of inertial sensors, T_{sur} is the surrounding temperature, and T_{set} is the set temperature. In this technique, it is important to make sure that the temperature profile of the temperature set point at the increasing surrounding temperature should be different from the temperature profile at the decreasing surrounding temperature, as shown in Figure 2.17. Otherwise, the temperature set point will oscillate between two adjacent set points in a boundary region.

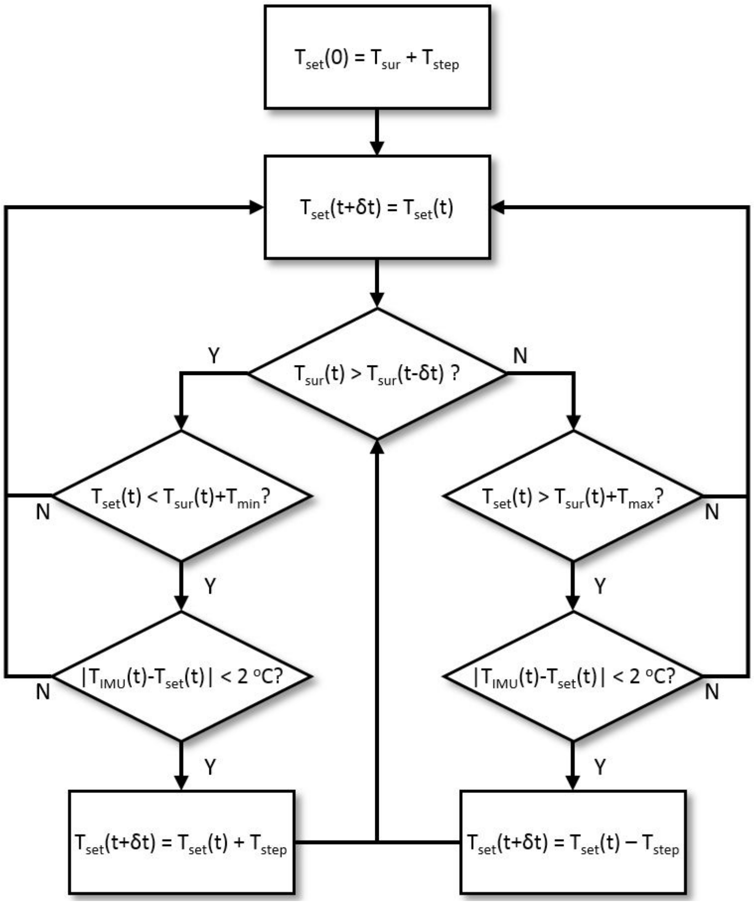

Figure 2.16: Flow chart of the MSP technique.

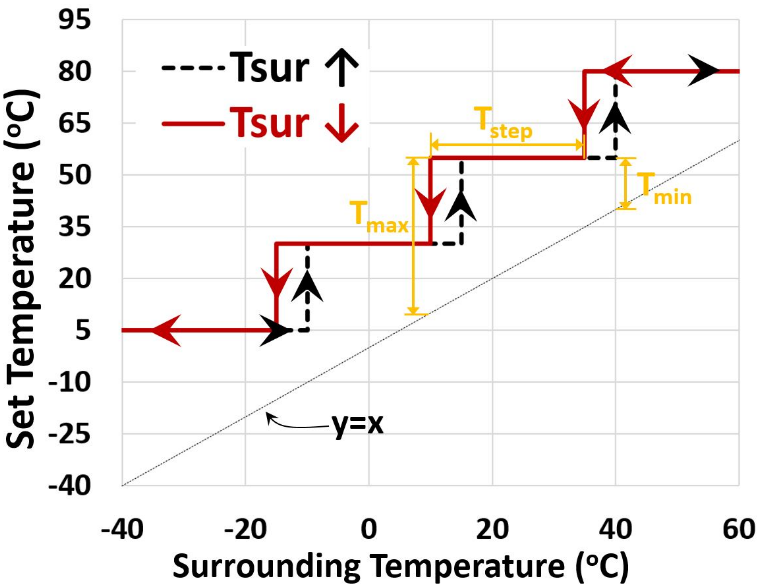

Figure 2.17: Temperature profile of temperature set points for the MSP technique.

Next, the MSP technique was implemented in the SOCIS, and the SOCIS was then thermal-cycled from 65 °C to -40 °C and back to 65 °C at the rate of 1 °C/min. The surrounding temperature and IMU temperature during the thermal-cycle test are shown in Figure2.18. Also, outputs of 3-axis gyroscopes and 3-axis accelerometers in MPU-6050 during the same test are shown in Figure2.19 and Figure2.20, respectively. Furthermore, Figure2.21 shows the ratio of power consumption when the MSP technique was used in the SOCIS to power consumption when the SSP technique was used in the SOCIS. The ratio is a calculated value based on $\Delta temperature$, and is specified in percentage. The result suggests that power consumption will be reduced by up to 88 % at the lowest surrounding temperature (-40 °C). Finally, temperature-induced bias drift for each of the inertial sensors is summarized in Table 2.4. The number of temperature set points in the MSP technique can be adjusted depending on the desired temperature-induced bias drift and power consumption.

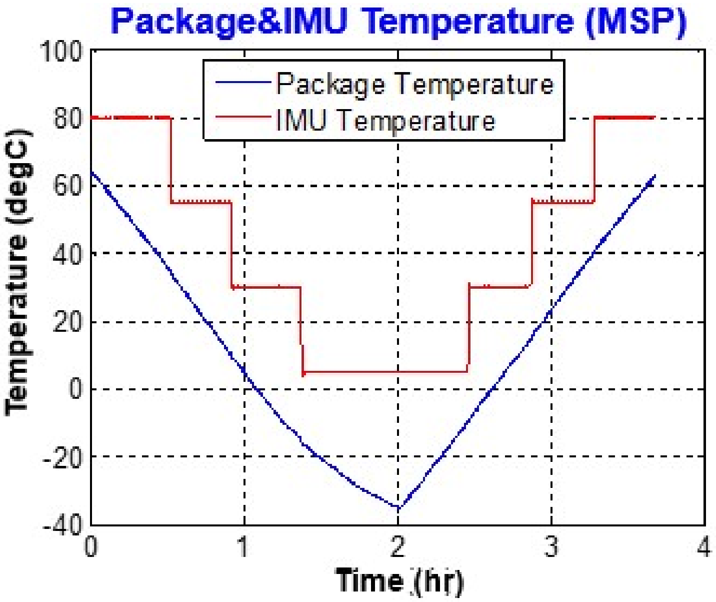

Figure 2.18: Measured surrounding and IMU tempetaures when the MSP algorithm was used in the SOCIS.

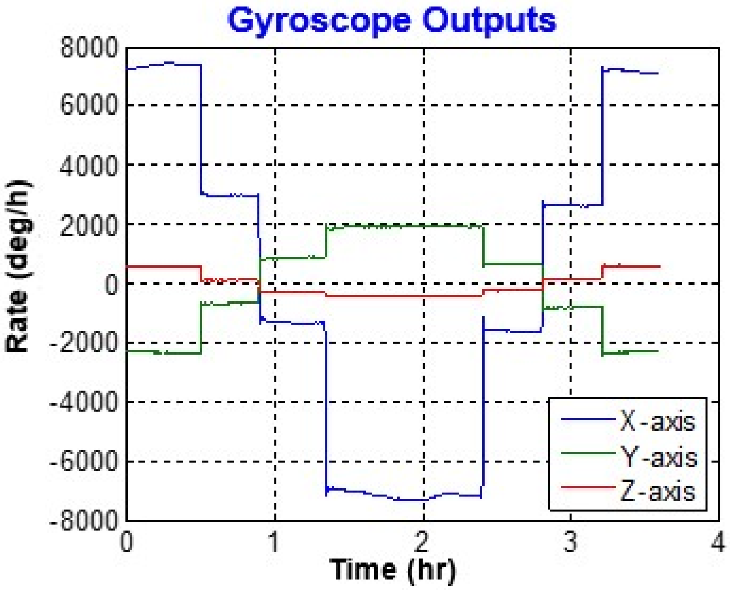

Figure 2.19: Measured rate outputs from Invensense MPU-6050 when surrounding and IMU temperatures change according to Figure 2.18.

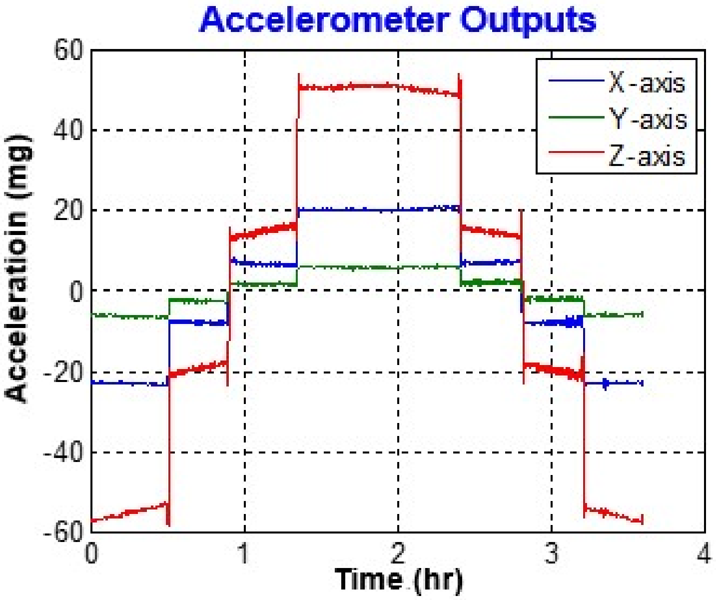

Figure 2.20: Measured acceleroation outputs from Invensense MPU-6050 when surrounding and IMU temperatures change according to Figure 2.18.

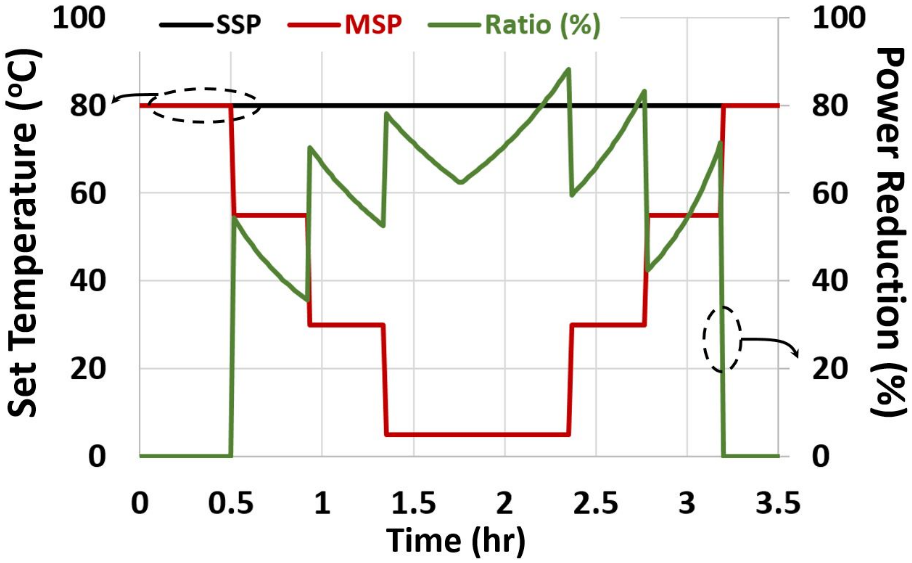

Figure 2.21: IMU temperatures during SSP and MSP oven-controls, and calculated ratio of power consumption during SSP oven-control to power consumption during MSP oven-control.

Table 2.4: Performance of MSP algorithm during thermal-cycle

Surrounding Temperature Range	Gyroscopes (°/h)			Accelerometers (mg)		
	X	Y	Z	X	Y	Z
60 °C to 35 °C	211	78.6	41.5	1.95	2.15	5.97
35 °C to 10 °C	48.6	56.6	51.6	1.59	1.48	4.21
10 °C to -15 °C	122	79.7	42.6	1.86	1.18	5.23
-15 °C to -40 °C to -10 °C	445	188	51.6	2.53	1.68	5.24
-10 °C to 15 °C	79.9	40.6	45.9	1.69	1.66	4.13
15 °C to 40 °C	60.7	79.7	39	3.35	2.02	4.86
40 °C to 60 °C	146	71.7	36.5	3.07	2.04	5.91

2.3 Thermal Stability

Since the temperature effect on the MEMS inertial sensors is mitigated by controlling their temperature to a constant value in the SOCIS, thermal stability of the controlled temperature is one of the critical specifications for the SOCIS. In order to obtain high thermal stability of the temperature of the inertial sensors, accuracy and precision of the oven-control system need to be improved. The accuracy of the oven-control system would be determined by a temperature sensor that represents the temperature of the inertial sensors, while precision of the oven-control system would be determined by a control algorithm for the oven-control system. Therefore, in this section, we will discuss several temperature sensing methods and a control algorithm for the SOCIS to improve thermal stability.

2.3.1 Temperature Sensing Methods

In the SOCIS, temperature measurement from a temperature sensor may not represent the actual temperature of the MEMS inertial sensors, if a finite thermal resistance exists between the temperature sensor and the MEMS inertial sensors. Furthermore, this discrepancy would change over time if the surrounding temperature fluctuates during a thermal-cycle test. As a result, the actual temperature of the MEMS inertial sensors would change significantly during the thermal-cycle, even if the temperature measured by the temperature sensor were perfectly controlled at a constant value. Therefore, finding an appropriate method that accurately represents the temperature of the MEMS inertial sensors in the SOCIS is critical.

In order to find the most accurate temperature sensing method, a total of three temperature sensing methods were prepared: 1) a resistance temperature detector (RTD), which is fabricated on the isolation stage near the inertial sensors by depositing and patterning a Ti/Pt metal layer; 2) an on-chip temperature sensor in the MPU-6050; and 3) a resonator of the X-axis gyroscope in MPU-6050.

In the first temperature sensing method, the RTD, resistance of the RTD was measured by using the 4-pt measurement method. The 4-pt measurement method, as shown in Figure 2.22, is a method that employs four electrical nodes to measure the resistance of a resistor, instead of employing two electrical nodes in a conventional method, to exclude parasitic resistances (R_{par}) in the measurement. Two electrical nodes at each end of the RTD ($I+$ and $I-$) are used to flow a constant current through it, while the other two electrical nodes are used to measure the voltage across the RTD ($V+$ and $V-$). Because the current only flows through the path between $I+$ and $I-$, there will be no voltage drop due to the lead resistance in the voltage measurement. Therefore, more accurate measurement of the RTD (R_{RTD}) will be possible than with the conventional 2-point measurement method.

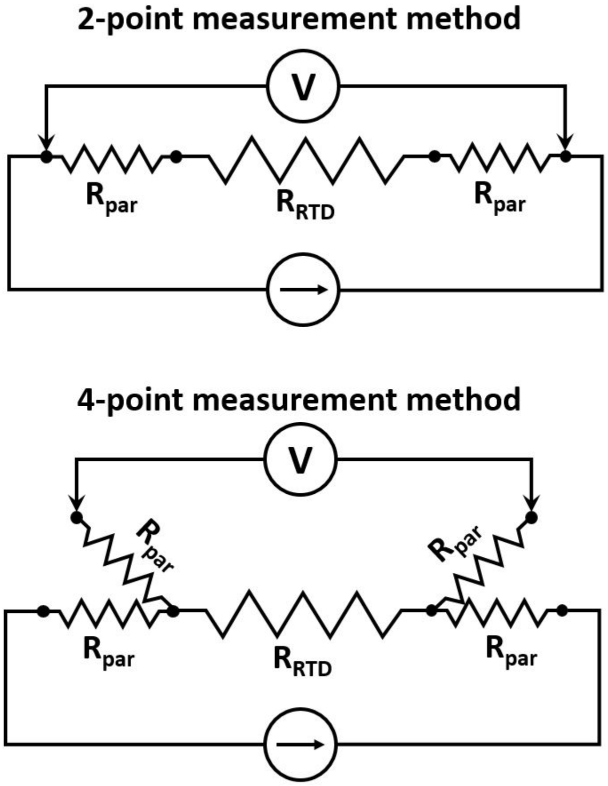

Figure 2.22: 2-point and 4-point measurement methods.

Next, the on-chip temperature sensor in MPU-6050, which is integrated on the same die as the read-out IC die for the MEMS inertial sensors in MPU-6050, was used to measure the temperature in the SOCIS. The data was collected from the digital output of MPU-6050. According to the datasheet, this temperature sensor can measure from -40 to 85 °C, and its linearity is ± 1 °C within the same temperature range [24].

Finally, the resonant frequency of the X-axis gyroscope in the MPU-6050 was used to measure the temperature. Structure of the gyroscope in MPU-6050 is designed based on a silicon tuning-fork resonator, and the resonant frequency of the resonator is directly affected by the surrounding temperature. Therefore, the resonator can be used to measure the temperature of the inertial sensors by measuring its resonant frequency. In order to measure the resonant frequency of the X-axis gyroscope, since there is no electrical pin on MPU-6050 that directly measures the resonant frequency of the X-axis gyroscope, the resonant frequency was indirectly measured by measuring an interrupt signal from MPU-6050, which can be configured to be generated from the resonant frequency of the X-axis gyroscope through a frequency divider. Furthermore, the frequency of the interrupt signal was calculated by using a frequency counter and a reference clock signal on a Teensy 3.2 microcontroller.

Prior to conducting experiments using the three temperature sensing methods, the Teensy 3.2 microcontroller was thermal-cycled from -40 °C to 85 °C to find the temperature sensitivity of the reference clock signal that will be used for calculating the resonant frequency of the X-axis gyroscope. This step is important because a temperature-sensitive reference clock will produce inaccurate results in the calculation. The test result is shown in Figure 2.23. The temperature sensitivity of the reference clock signal was found to be ±10 ppm during the thermal-cycle test. This would produce a temperature variation of approximately ± 0.4 °C in the SOCIS during the same thermal-cycle, given that the temperature sensitivity of a silicon resonator is around -26 ppm/°C [59].

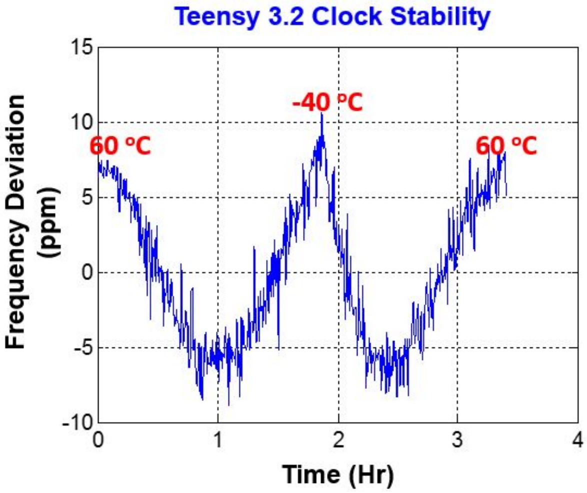

Figure 2.23: Temperature sensitivity of the Teensy microcontroller reference clock.

After then, based on the observed temperature sensitivity of the reference clock signal from Teensy 3.2, the gyroscope frequency variation was calibrated to the surrounding temperature measured by a temperature sensor that is located outside the package for each of the experiments using different temperature sensing methods, and the calibrated temperature was used as reference for the actual IMU temperature. This temperature is the y-axis in Figure 2.24. In each test shown in this graph, the surrounding temperature was ramped from -40 °C to 60 °C at the rate of 1 °C/min, and the un-calibrated X-axis gyroscope frequency, the RTD, or the on-chip solid-state temperature sensor was used to close-loop control the IMU temperature to 80 °C. As illustrated, when using the un-calibrated gyroscope frequency for closed-loop temperature control, there was a ±0.4 °C change in the actual IMU temperature. This change is likely due to the ±10 ppm change in the reference clock that was used for measuring the resonant frequency of the gyroscope. Also, when the RTD was used for closed-loop temperature control, there was a 3.3 °C change in the actual IMU temperature. This relatively high change is due to the fact that finite thermal resistance between the RTD and the IMU causes the discrepancy in their temperatures, and the discrepancy changes as the surrounding temperature changes. Finally, when the on-chip temperature sensor was used for closed-loop temperature control, there was a 0.03 °C change in the actual IMU temperature. This excellent stability over surrounding temperature is related to how close a temperature sensing method sits to the actual inertial sensors and how sensitive a read-out circuit for a temperature sensing method is to temperature variation. Therefore, we concluded that the on-chip temperature sensor is the most accurate source among these three methods to determine the actual IMU temperature in this specific experiment.

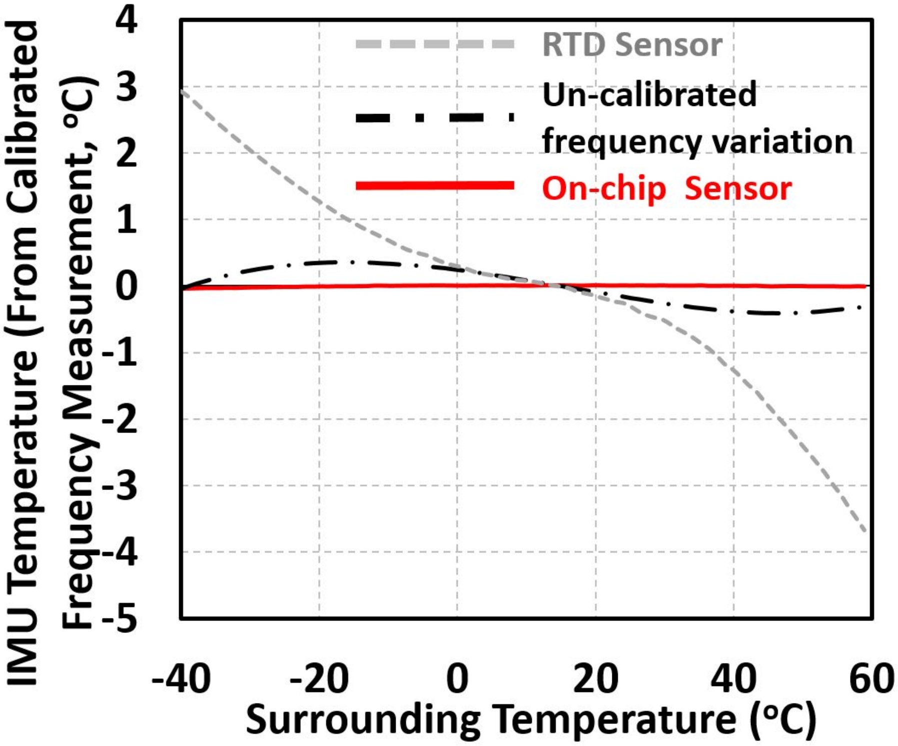

Figure 2.24: Measured IMU temperature variations of the SOCISs using three different temperature sensing methods for closed-loop control: the RTD, the resonator, and the on-chip temperature sensor.

2.3.2 Temperature Control Method

In order to provide high precision in the SOCIS, an appropriate temperature control method needs to be developed. One of the most typical and mature control methods is the proportional-integral-derivative (PID) controller. Mathematical expression for the PID controller is [60]:

$$V(t) = K_P \cdot e(t) + K_I \cdot \int_0^t e(t)dt + K_D \cdot \frac{de(t)}{dt} \tag{2.17}$$

where K_P, K_I, and K_D are proportional (P), integral (I), and derivative (D) gains, $e(t)$ is an error or the difference between the temperature set point and the measured temperature at time t, and $V(t)$ is the corresponding controller output. The first term in this equation is called a proportional term and it multiplies the error by the proportional gain, K_P. This term alone can decrease transient response time and the error to a certain degree. In a steady state, however, the proportional term alone cannot eliminate the error completely and thus leaves an offset. This offset can be eliminated by adding the second term in the equation—an integral term. The integral term accumulates past errors over the course of time and is multiplied by the integral gain, K_I. This term not only eliminates the offset, but also rejects the disturbance. Finally, the third term is called a derivative term and it predicts future errors by calculating the derivative of current errors. This term is known to reduce the transient response time of a control system by mitigating the overshoot effect—the effect in which controlled temperature goes much beyond the set temperature—or undershoot effect—the effect in which controlled temperature goes much below the set temperature—, if any, thus increasing the controllers stability [60].

In order to obtain an initial good guess for the PID parameters, one of the most popular methods, the Ziegler-Nichols step response method was used [61]. A step input voltage with the magnitude of 1V was first applied to the input of the heater driving circuit at 0 seconds. The step response at the IMU temperature was then observed, as shown in Figure 2.25. Based on the step response and Table 2.5, initial PID parameters were calculated. In the step response experiment, it was found that a is 4.74 °C and τ is 0.83 seconds. In order to build an oven-control system with a faster rise and settling times, and better stability, these PID values were manually fine-tuned afterward to optimize for the start-up time.

Table 2.5: Calculation of PID parameters according to Ziegler-Nichols method.

Type	K_P	K_I	K_D
P	1/a	-	-
PI	0.9/a	$K_P/3\tau$	-
PID	1.2/a	$K_P/2\tau$	$K_P \cdot 0.5\tau$

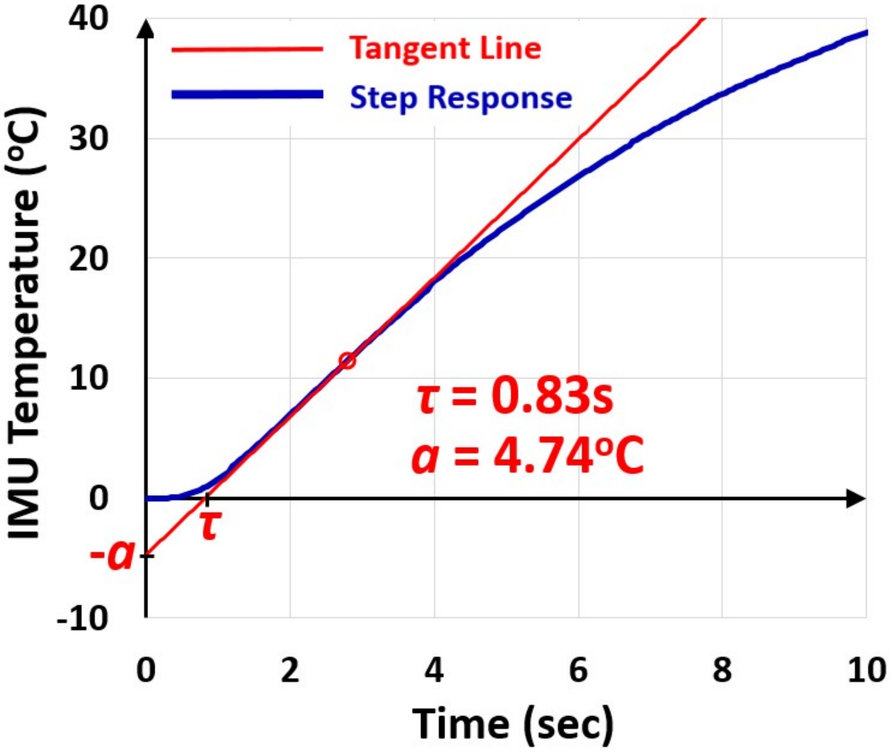

Figure 2.25: ZieglerNichols step response experiment.

After the fine-tuning process was completed, the startup time and stability of the control system were measured at room temperature. Target IMU set temperatures were 60 *degree*C, 70 *degree*C, and 80 *degree*C, and two initial conditions for the controller, cold start and warm start, were considered in the experiment. In the cold start condition, the system power is physically disconnected for more than 24 hours and connected back right before the oven-control system is turned on, while in the warm start condition, the system power is connected at all times but only the oven-control is turned off until it is turned back on for the test. Furthermore, the startup time was measured at a time when the controlled IMU temperature reaches within ±0.1 °C of the final set point (or approximately 0.1% of the final set point).

Experimental results are shown in Figure 2.26 where the IMU was controlled at 60 °C, 70 °C, and 80 °C in the warm start initial condition from room temperature, and experimental results in both the warm and the cold initial conditions are summarized in Table 2.6. The startup times in the warm start condition were found to be 25.7 seconds, 41.1 seconds, and 50.2 seconds for the set temperatures of 60 °C, 70 °C, and 80 °C, respectively, and the startup times in the cold start condition were 32.7s, 48.1s, and 57.2s for the set temperatures of 60 °C, 70 °C, and 80 °C, respectively. Therefore, reaching 80 °C from room temperature would take less than a minute in both cold and warm initial conditions, and this may be further improved by increasing the maximum available heater power consumption or the thermal resistance of the SOCIS.

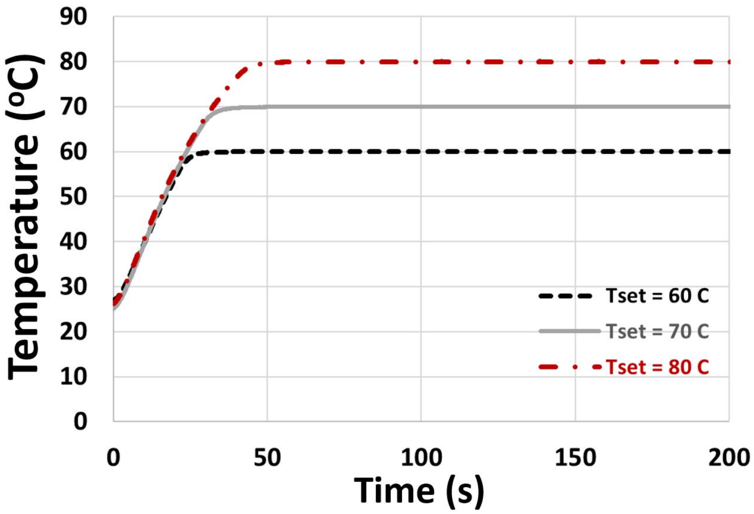

Figure 2.26: IMU temperature during start-up time measurements in warm start initial condition: target oven set temperatures are 60 °C, 70 °C, and 80 °C.

Table 2.6: Summarized startup time.

Surrounding Temp.	Oven Temp.	Cold Start	Warm Start
RT	60 °C	32.7s	25.7s
RT	70 °C	48.1s	41.1s
RT	80 °C	57.2s	50.2s

After the startup time and thermal stability were measured at room temperature, a test setup was prepared to measure the thermal stability during a thermal-cycle test. The IMU temperature was controlled at 80 °C during the thermal-cycle test where the surrounding temperature changed from -40 °C 70 °C at the rate of 1 °C/min. The result is shown in Figure 2.27. The standard deviation (1σ) of the IMU temperature during the thermal-cycle test was found to be 7.1 m°C, which should be low enough for the SOCIS.

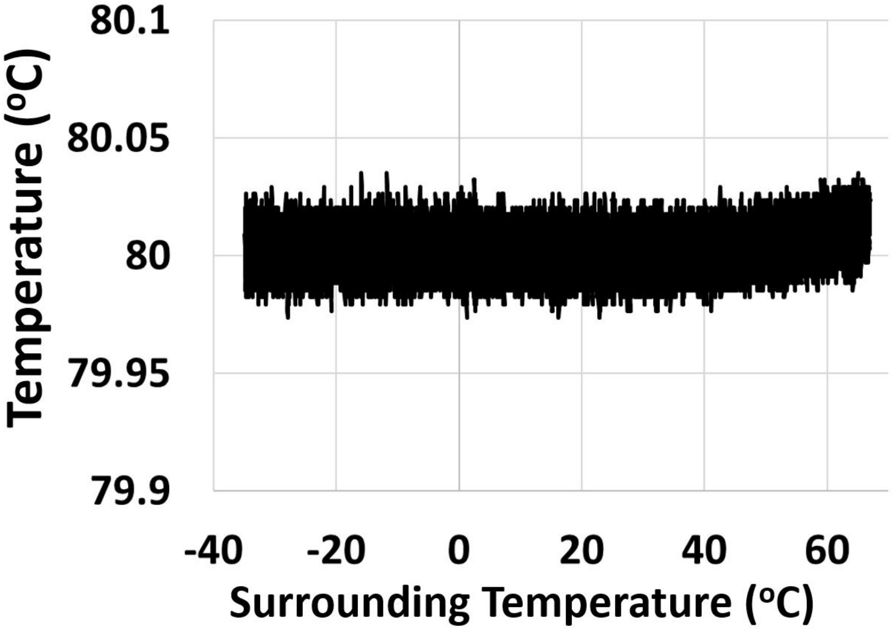

Figure 2.27: IMU temperature vs surrounding temperature during the thermal-cycle test.

2.4 Design of Isolation Stage in SOCIS

Since a single isolation stage is used in the SOCIS to mitigate stress, vibration, and temperature effects on the MEMS inertial sensors, the following design specifications need to be considered: a good stress-relieving ability, a high resonant frequency, and a high thermal resistance of the isolation stage. The stress-relieving ability of the isolation stage is an important specification because MEMS inertial sensors are known to be very susceptible to stress as mentioned previously. Furthermore, because inertial sensors should be able to accurately measure the motion of an object of interest, if the resonant frequency of the isolation stage is too low, then the movement of the isolation stage may interfere with the motion of the object. Finally, the thermal resistance should be considered to reduce the power consumption and the thermal stability in the oven-control system [44]. Therefore, geometric parameters for a crab-leg isolation stage are studied through simulations to provide good stress-relieving ability, high resonant frequency, and high thermal resistance.

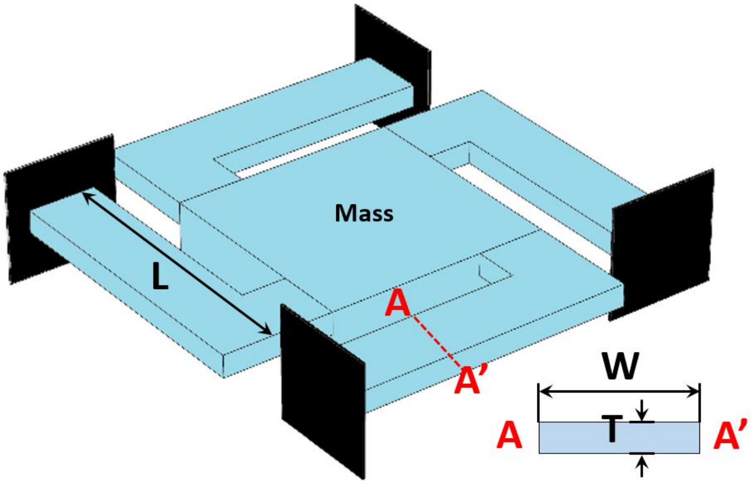

Figure 2.28: Basic crab-leg structure [62].

The width (W), length (L), and thickness (T) of the beams of the isolation stage are the three key design parameters to meet the three design requirements—good stress-relieving ability, high resonant frequency, and high thermal isolation. A design optimization process has been performed by considering two main properties of the isolation stage: stiffness (or a spring constant) and thermal conductivity. A basic crab-leg structure is shown in Figure 2.28 and the spring constant in the z-direction (i.e., perpendicular to the mass) can be calculated as [62]:

$$k_z = 4 \cdot \frac{E \cdot W \cdot T^3}{L^3} \tag{2.18}$$

where k_z is the spring constant of the crab-leg structure in the z-direction in N/m, E is Youngs modulus of the beams in N/m^2, W is the width of the beams in m, T is the thickness of the beams in m, and L is the length of each of the beams in m. Furthermore, the thermal resistance of the crab-leg structure can be calculated as:

$$R_{leg} = \frac{1}{4} \cdot \frac{L}{k_{th} \cdot W \cdot T} \tag{2.19}$$

where R_{leg} is the thermal resistance of the isolation stage in K/W, and k_{th} is a thermal conductivity of the material used for fabricating the isolation stage in $W/m \cdot K$. According to Equation 2.18 and Equation 2.19, wider, thicker, and shorter legs will make the isolation stage mechanically stiffer (i.e., higher k_z) and thermally more conductive, while narrower, thinner, and longer legs will make it more flexible (i.e., lower k_z) and thermally less conductive. Therefore, the design of the isolation stage requires trade-offs, because a less conductive isolation stage with a better stress-relieving ability requires narrower, thinner, and longer legs, while an isolation stage with a higher resonant frequency requires wider, shorter, and thicker legs.

Prior to finding the optimum design parameters for the isolation stage, the desired thermal resistance of the isolation stage was first calculated. Experimentally, multiple vacuum-packaging trials were performed, and it was found that the vacuum level inside the package ranges from tens to hundreds of mTorr. Since the thermal resistance due to heat loss through the gas conduction at such a vacuum level will be 2,000 K/W or less according to Figure 2.9, a high thermal resistance through the isolation stage will be desired to compensate for the heat loss through gas conduction. Therefore, considering the size restriction for the isolation stage due to the size of the package, 25,000 K/W was selected as a desired thermal resistance through the isolation stage.

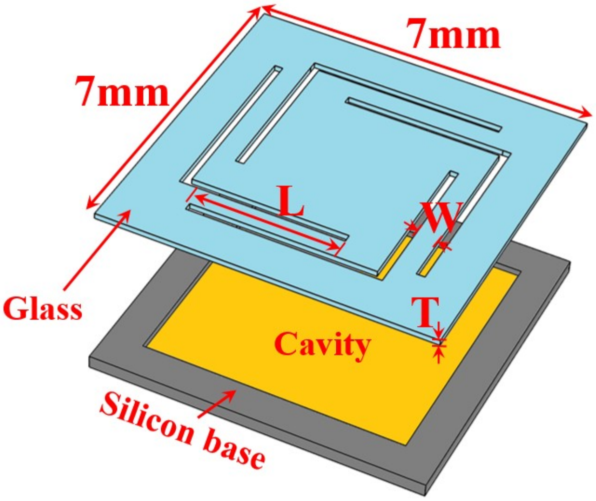

Figure 2.29: A micro isolation platform [51].

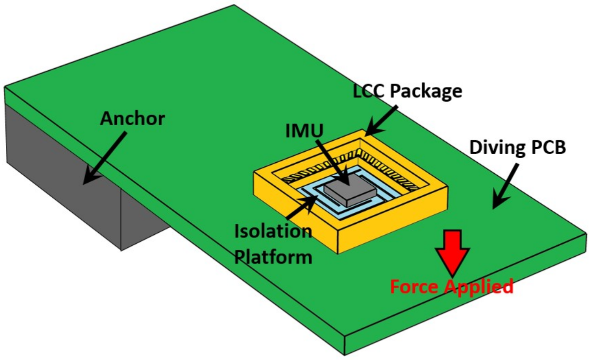

Figure 2.30: A geometry for testing stress effect on the IMU using a cantilever PCB.

Based on the desired thermal resistance of the isolation stage, 3D multi-physics simulations have been performed using commercial software, COMSOL, to find the optimal design parameters for the isolation stage, as shown in Figure 2.29. In the simulation, a silicon block, which represents the IMU, was mounted on the isolation stage, and packaged in a leadless chip carrier (LCC) package. The LCC package was then mounted on a cantilever printed circuit board (PCB) where one side is suspended while the other side is fixed on the main PCB (Figure 2.30). The suspended side was then pressed to be bent by a 1 cm displacement to induce stress on the IMU while the other side is still fixed. In order to calculate the width and length of each of the beams to provide the desired thermal resistance level using a glass wafer that has k_{leg} of 1 W/m·K and T of 100 μm, the equation becomes:

$$\frac{L}{W} = 10 \tag{2.20}$$

Figure 2.31 shows simulation results of the stress on the inertial sensors and the resonant frequency (up-down mode) of the isolation stage as the two parameters, the width and the length of the beams, are increased with their ratio fixed until the length becomes 5.5 mm, which is the maximum possible length of the beams since the side length of the isolation stage is 6 mm in this study. According to [24], the maximum required a bandwidth of the IMU used in this experiment (Invensense MPU-6050) is 260 Hz. Therefore, the mechanical resonant frequency of the isolation stage should be well above 260 Hz to ensure that the isolation stage does not interfere with the actual motion of the IMU. Fortunately, since the resonant frequency of the isolation stage is always above 260 Hz, only the stress relieving ability of the isolation stage can be considered. As a result, the width and length of the beams were determined to be 550 μm and 5500 μm, respectively. Furthermore, based on the analysis, it can be concluded that wider and longer beams are desired in the design of the isolation stage in the SOCIS, assuming the ratio of the length to width of the beams is fixed. Finally, the stress imposed on the inertial sensors without the isolation stage was computed in a simulation and found over 454 MPa, which is about 5.7 times higher than that with the optimized isolate stage.

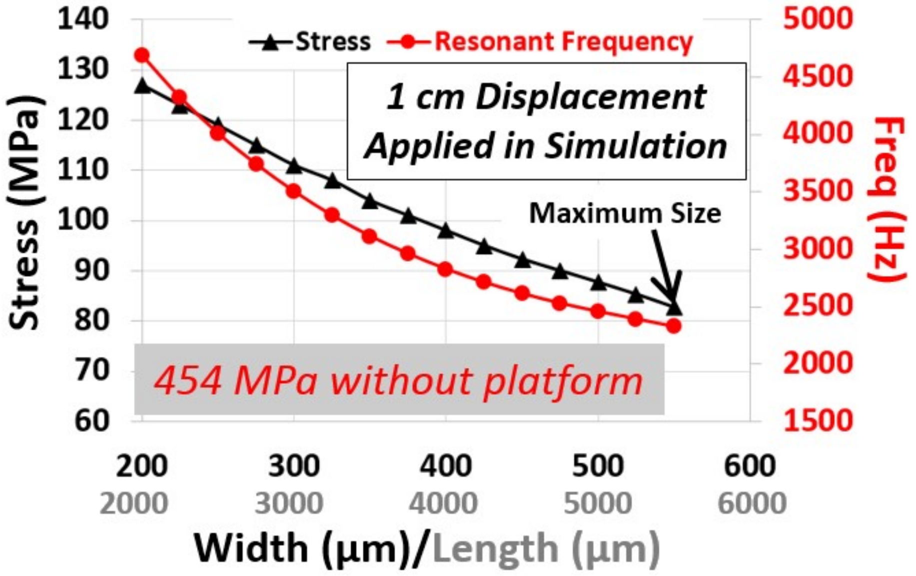

Figure 2.31: Simulation results: average stress on the IMU and resonant frequency of the isolation stage over the width and length of the beams.

2.5 Performance and Error Analyses of the SOCIS

In this section, the performance and error analyses of the SOCIS, including the noise performance at room temperature, temperature-induced errors during the thermal-cycle test, stress-induced errors, effect of the bias voltage of the gyroscope on the performance of the gyroscope, effect of the voltage across the heater in the SOCIS on the Z-axis accelerometer, and temperature-induced position errors in the INS using the SOCIS, will be presented.

2.5.1 Noise Performance

Since the MEMS inertial sensors are controlled at an elevated temperature in the SOCIS, there is a concern about the degradation of the noise performance of the inertial sensors due to the elevated temperature. For example, in [28], it was found that the ARW and BI of the vibratory gyroscope were inversely proportional to the temperature. Therefore, it is important to examine if the elevated temperature in the SOCIS degrades the noise performance of the MEMS inertial sensors.

In order to examine the effect of the elevated temperature on the noise performance of the MEMS inertial sensors, five SOCISs using Invensense MPU-6050s were prepared, and the outputs from each of these SOCISs were recorded for 10 hours without oven-control (i.e., No Oven) and another 10 hours with oven-control at 80 °C (i.e., Oven). Using the 10-hr data, ADEV values were calculated and plotted as shown in Figure 2.32 and Figure 2.33, and ARWs, VRWs, and BIs are summarized in Table 2.7. As a result, the average ARW of the five 3-axis gyroscopes with oven-control was higher than the average ARW of the five 3-axis gyroscopes without oven-control by 5%, while the average BI of the five 3-axis gyroscopes with oven-control was lower than the average BI of the five 3-axis gyroscopes without oven-control by 18%. Likewise, the average VRW of the five 3-axis accelerometers with oven-control was higher than the average VRW of the five 3-axis accelerometers without oven-control by 8%, while the average BI of the five 3-axis accelerometers with oven-control was lower than the average BI of the five 3-axis accelerometers without oven-control by 11%. Overall, it was found that the ARW and VRW, which are the metrics that indicate the level of white noise in the inertial sensors, were degraded, while the BI, which is the metric that indicates the level of flicker noise, was improved. The degraded ARW and VRW are expected since the mechanical white noise can be increased due to the decreased quality factor of the inertial sensors at an elevated temperature, but the improved BIs were not expected since these values are also known to be degraded at a higher temperature. We believe another factor may have affected the BI values in the inertial sensors without oven-control, and the factor is a small temperature fluctuation in ambient temperature in the test setup, which is around ±0.5 °C for 10 hours, to cause the long-term bias drift. As a result, the rate ramp (RR) was added to the ADEV plot, and higher BIs were observed. Likewise, since the temperature of the inertial sensors with oven-control was controlled precisely within ±10 m°C, lower BIs were observed.

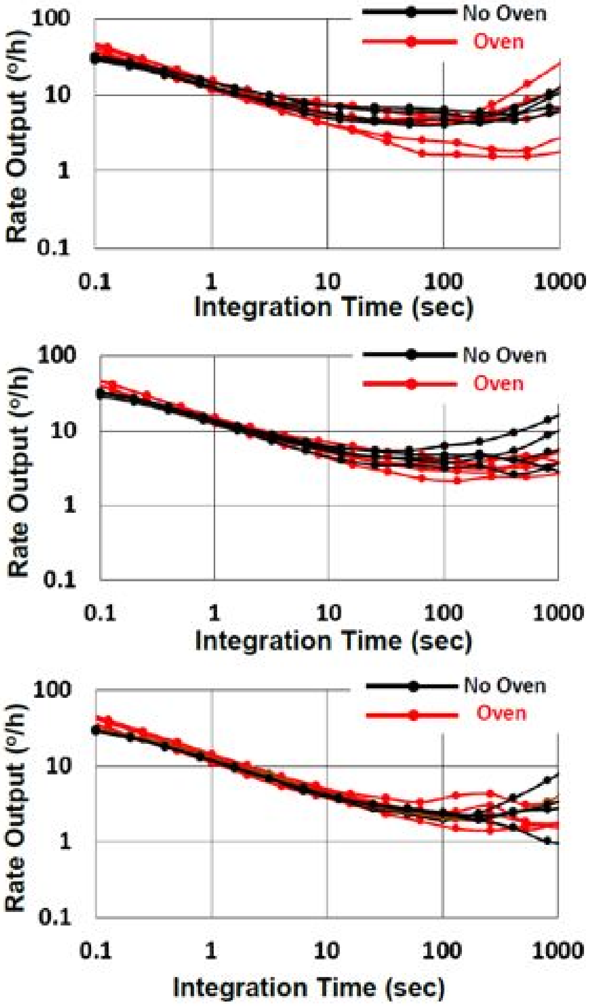

Figure 2.32: ADEV plots for five 3-axis gyroscopes in Invensense MPU-6050 without oven-contro (No Oven) and with oven-control (Oven). X-axis, Y-axis, and Z-axis gyroscopes from top to bottom.

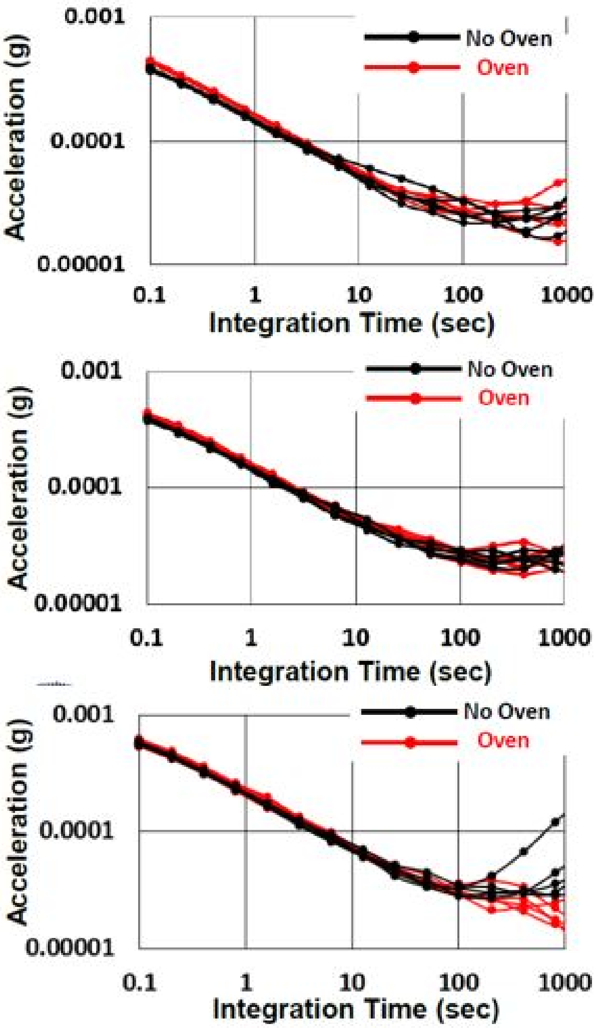

Figure 2.33: ADEV plots for five 3-axis accelerometers in Invensense MPU-6050 without oven-contro (No Oven) and with oven-control (Oven). X-axis, Y-axis, and Z-axis accelerometers from top to bottom.

Table 2.7: NOISE PERFORMANCE COMPARISON

Item	No Oven Gyroscopes	Oven Gyroscopes	No Oven Accelerometers	Oven Accelerometers
# of Samples	5	5	5	5
ARW/VRW ($^\circ/\sqrt{hr}$ or μg/$\sqrt{Hz}$)	0.22, 0.23, 0.21	0.24, 0.24, 0.21	150, 150, 220	170, 160, 230
Bias instability (°/hr or μg)	4.78, 3.81, 1.86	3.77, 2.94, 1.85	21, 22, 29	22, 22, 20

2.5.2 Performance Analysis during Thermal-Cycle

Prior to conducting a thermal-cycle test on the SOCIS over the commercial temperature span (-40 °C to 85 °C), an appropriate set temperature point needs to be determined first, because a low set temperature point would lead to an unstable operation of the oven-control system, while a high set temperature point would lead to the high power consumption. In order to determine the appropriate set temperature point, a thermal-cycle test on the SOCIS without oven-control was conducted, and the thermal resistance was measured based on the IMUs self-heating effect, as shown in Figure 2.34. Interestingly, the thermal resistance changed from 1200 K/W to 600 K/W as the surrounding temperature was changed from -40 °C to 85 °C. This indicates that the vacuum level inside the package changes as the surrounding temperature changes. We believe this is because the amount of outgassing from the silver epoxy and the epoxy molding compound (EMC) changes as the surrounding temperature changes. Fortunately, this change in the thermal resistance can allow the oven-control system to operate at a lower set temperature because the smaller thermal resistance will reduce the temperature rise from the self-heating effect at a higher surrounding temperature. Given that the power consumption of MPU-6050 and the thermal resistance of the SOCIS at 85 °C are around 10 mW and 600 K/W, respectively, the minimum set temperature point can be calculated as:

$$T_{set,min} = R_{TOT,85} \cdot P_{IMU,85} + T_{sur} = 600K/W \cdot 10mW + 85°C = 91°C. \qquad (2.21)$$

where $R_{TOT,85}$ is the total thermal resistance of the SOCIS at 85 °C, $P_{IMU,85}$ is the power consumed by MPU-6050 at 85 °C, and T_{sur} is the surrounding temperature. In order to ensure stable operation, 1 °C margin was given to the set temperature point. Therefore, the set temperature point for the SOCIS was determined to be 92 °C.

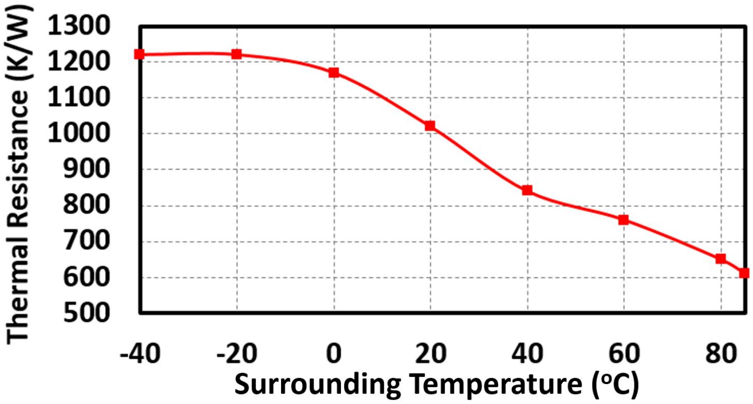

Figure 2.34: Thermal resistance of the SOCIS at different surrounding temperatures.

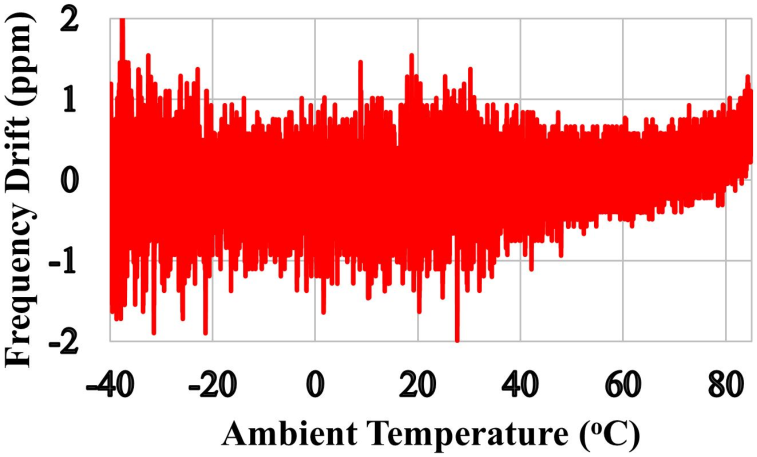

Figure 2.35: Frequency drift of the X-axis gyroscope in the SOCIS.

The IMU was then oven-controlled at 92 °C at room temperature, and stabilized in the same conditions for one hour prior to a thermal-cycle test to eliminate possible start-up drifts that are not relevant to the temperature change. After that, the IMU was thermal-cycled in an oven chamber where the temperature of the oven chamber was ramped from -40 °C to 85 °C at the rate of 1 °C/min. After the thermal-cycle test was completed, it was found that the average standard deviation (1 σ) of the IMU temperature is 7.8m °C and the corresponding frequency drift of the X-axis gyroscope during the same thermal-cycle test is ±2 ppm (pk-to-pk) over the entire temperature span (2.35). Furthermore, the root sum squared (RSS), which is one of the metrics for computing bias drifts in 3-axis navigation systems [63], is used to compare temperature-induced bias errors in the SOCIS with those in the regular IMU (i.e., non-ovenized IMU). The equation for the RSS method can be expressed as:

$$RSS = \sqrt{X_{drift}^2 + Y_{drfit}^2 + Z_{drift}^2} \tag{2.22}$$

where X_{drift}, Y_{drift}, and Z_{drift} are peak-to-peak temperature-induced bias drifts on the X-axis, Y-axis, and Z-axis inertial sensors, respectively.

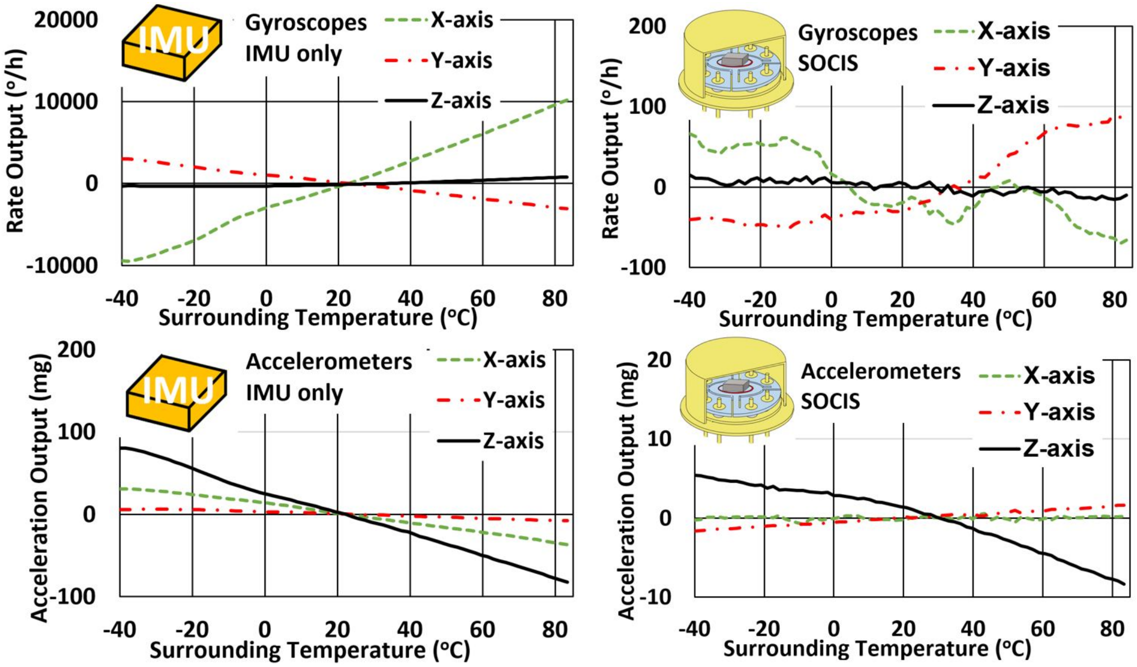

Figure 2.36: Bias drifts of the regular IMU (IMU only) and the SOCIS over the surrounding temperature.

Table 2.8: Quantitative comparison table for the bias drifts of the regular IMU (IMU only) and the SOCIS over the surrounding temperature.

Configuration	Gyroscopes Peak-to-peak bias drifts (°/h)				Accelerometers Peak-to-peak bias drifts (mg)			
	X	Y	Z	RSS	X	Y	Z	RSS
IMU Only (No Oven-Control)	20610	6486	1288	21650	72.22	14.91	170.6	185.9
Oven-Control	136.7	144.6	30.53	201.3	1.345	3.236	13.74	14.18

Figure 2.36 shows the measured bias drifts of the 6-axis IMU with and without the oven-control during the thermal-cycle test, and their total drifts and RSSs during

the thermal-cycle test are summarized in Table 2.8. When the 6-axis IMU was not oven-controlled (IMU Only), the total bias change was very high for both gyroscopes and accelerometers. Particularly for the gyroscopes, the X-axis gyroscope showed the largest bias drift, while the Z-axis gyroscope showed the smallest drift. The main difference between these two axes is their gyroscope mechanical structures, and we think that this is the main reason why the X-axis gyroscope is more susceptible to the temperature change than the Z-axis gyroscope [9]. In addition, although the X- and Y-axis gyroscopes have the same gyroscope structure with the Y-axis gyroscope being rotated by 90°, we observed that the temperature-induced bias drift in the X-axis gyroscope was three times larger than that in the Y-axis gyroscope. This is, however, not always the case, because we found from other MPU-6050 samples that the temperature-induced bias drifts in the Y-axis gyroscope were larger than the bias drifts in the X-axis gyroscope, or they were about the same in some other samples. Similarly, the structure of the Y-axis accelerometer is the same as that of the X-axis accelerometer but rotated by 90°, while the Z-axis accelerometer has a completely different structure. As a result, the Z-axis accelerometer showed the largest bias changes of all, and this was consistent for other samples. On the other hand, when the 6-axis IMU was oven-controlled at 92 °C (SOCIS), the X- and Y-axis gyroscopes showed comparable bias drifts, while the Z-axis gyroscope showed the smallest drift. Similarly, the oven-controlled X- and Y-axis accelerometers in the SOCIS showed comparable bias drifts, while the oven-controlled Z-axis accelerometer showed the largest drift. Finally, RSSs of the 3-axis gyroscopes and 3-axis accelerometers were reduced by 108 times (21650 °/h to 201.3 °/h) and 13 times (185.9 mg to 14.18 mg), respectively.

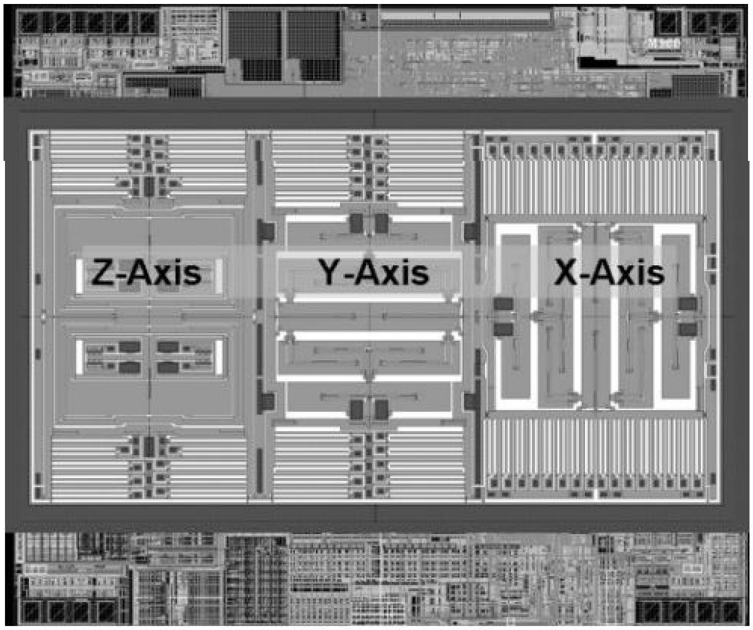

Figure 2.37: Geometry of Invensenses 3-axis gyroscopes [9].

After the analysis of a SOCIS was completed, seven more SOCISs and regular IMUs were prepared to find the variation from sample to sample. The SOCISs were oven-controlled at 80 °C and thermal-cycled from -40 °C to 70 °C at the rate of 1 °C/min. After that, the regular IMUs were also thermal-cycled in the same condition and the temperature-induced bias drifts of the regular IMUs were compared to those of the SOCISs. The total bias drifts of the SOCISs and the regular IMUs during the thermal-cycle tests are summarized in Figure 2.38, Figure 2.39, and Table 2.9. Furthermore, the temperature-induced bias drift (°/h/°C) of the SOCIS was compared with those of other state-of-the-art works and the comparison is shown in Figure 2.40. Please note that 1st order LMS calibration method was applied to the SOCIS in this comparison. From the result, it was found that the SOCIS with LMS calibration shows the best temperature-induced bias drift among all Si MEMS gyroscopes, and it is also comparable to those of the quartz MEMS gyroscopes, which are known to be less sensitive to the temperature effect than the Si MEMS gyroscopes, while power consumption of the SOCIS is one of the lowest.

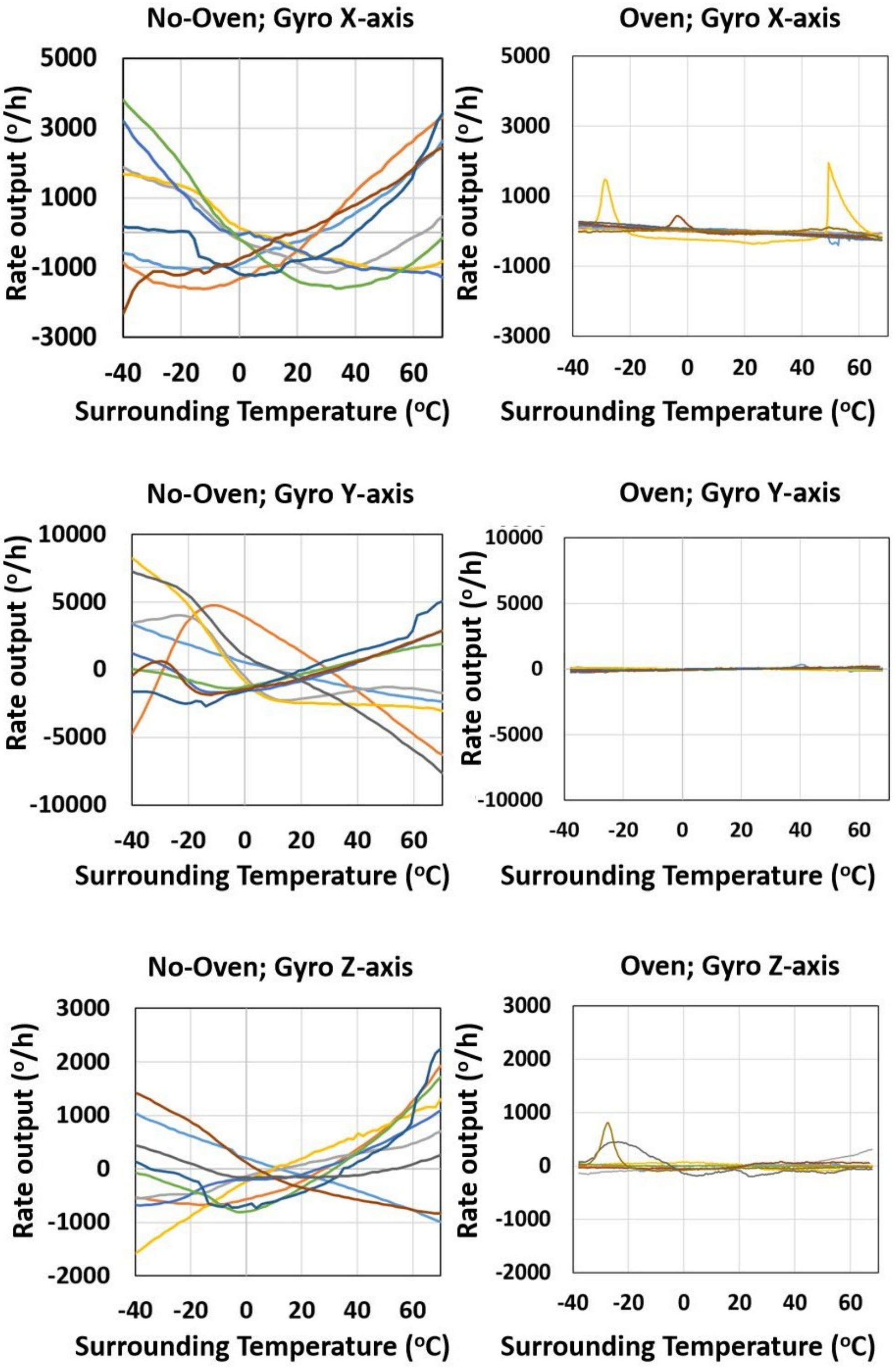

Figure 2.38: 3-axis Gyroscopes: Bias Drifts of eight regular IMUs and seven SOCISs.

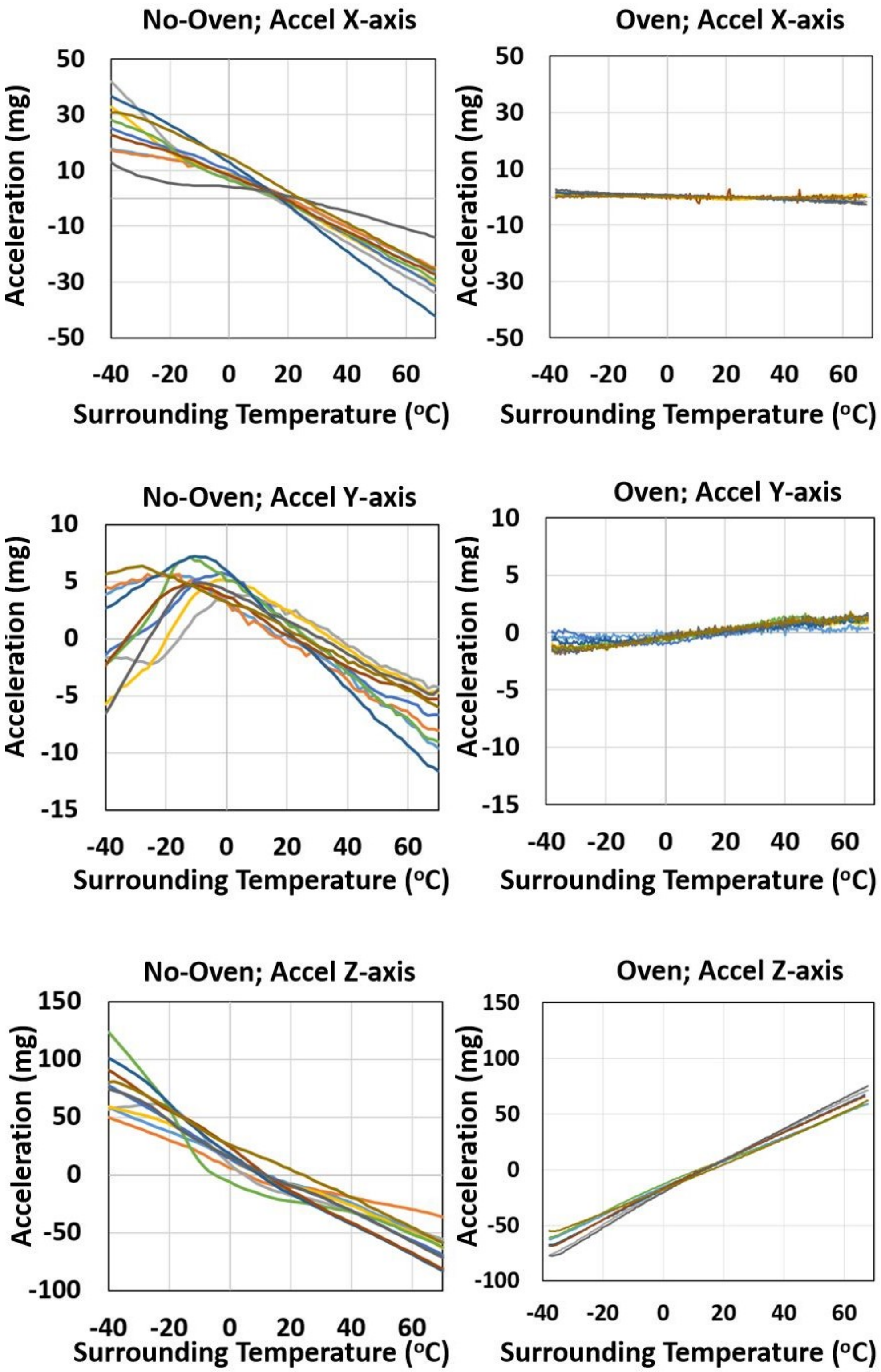

Figure 2.39: 3-axis Accelerometers: Bias Drifts of eight regular IMUs and seven SOCISs.

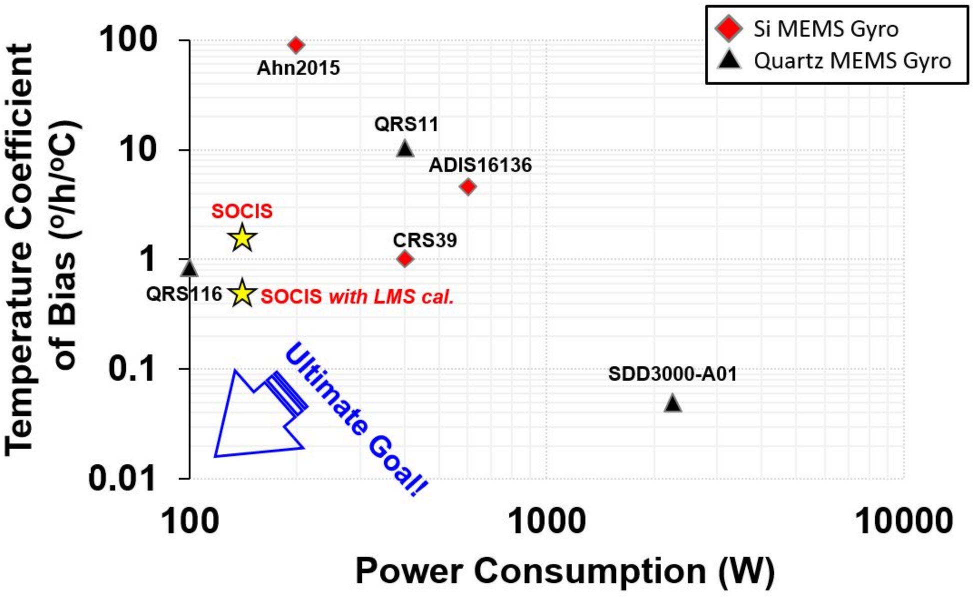

Figure 2.40: Performance comparison of the SOCIS with other state-of-the-art works [48, 64, 26, 65, 66, 67].

Table 2.9: Bias drifts of eight regular IMUs and seven SOCISs.

Condition	**Gyroscopes (°/h)**				**Accelerometers (mg)**			
	X	**Y**	**Z**	**RSS**	**X**	**Y**	**Z**	**RSS**
Regular IMU	±1906	±3588	±939.5	±4170	±25.5	±6.36	±65.2	±70.3
SOCIS	±315.9	±148.5	±172.5	±389.5	±1.60	±1.35	±65.7	±65.8
Improvement	6.0↑	24↑	5.4↑	11↑	16↑	4.7↑	1.01↓	1.1↑

From the results, it was found that RSSs of the 3-axis gyroscopes and the 3-axis accelerometers were reduced by 4.8 times and 7.6 times, respectively, which are relatively low reductions when compared to the reductions in the SOCIS that was tested for the first time. Furthermore, in some of the gyroscope units in the SOCISs, an unexpected change, or a "bump", was found during the thermal-cycle. Additionally, the bias drift in the Z-axis accelerometer was barely reduced even after the temperature of the accelerometer was precisely controlled at a constant temperature. Therefore, these non-ideal behaviors will be discussed in the following section.

2.5.3 Non-Ideal Behaviors in the SOCIS during Thermal-Cycle

Although the temperature effects on the 6-axis inertial sensors were improved by much after the inertial sensors were oven-controlled at a constant temperature in the SOCIS, we have found two non-ideal behaviors in the SOCISs during the thermal-cycle test. First, the temperature effect on the Z-axis accelerometer in the SOCIS was barely improved. Second, although the SOCIS reduces the temperature effect on the MEMS inertial sensors, some residual temperature-induced bias drifts still remain in the SOCIS and even a large "bump" was found on some gyroscopes. Therefore, this section will discuss these two non-ideal behaviors of the SOCIS in detail.

2.5.3.1 High Zero-g Output in the Oven-Controlled Z-axis Accelerometers

Based on the thermal-cycle test results of the SOCISs, we have found much higher zero-g outputs (i.e., bias drifts) of the Z-axis accelerometers than other two axes accelerometers. Furthermore, the temperature effect on the Z-axis accelerometers in the SOCISs was improved almost negligibly. In order to analyze this behavior, we have prepared 25 SOCISs across several batches, oven-controlled them at 80 °C, and thermal-cycled from -40 °C to 70 °C. The total bias drifts of the SOCISs during thermal-cycle tests were then plotted over available variables including thermal resistance, the voltage across the heater (heater voltage), process variations, test conditions, and stress sensitivities. Among these variables, a distinct correlation was found only when the total bias drifts of the Z-axis accelerometers in the SOCISs were plotted over the heater voltage difference between the voltage across the heater at T_{sur} of

-40 °C and the voltage across the heater at T_{sur} of 70 °C (Figure 2.41). On the other hand, when the total bias drifts of the Z-axis accelerometers during the thermal-cycle tests were plotted over other variables, no noticeable correlation was found. One example is shown in Figure 2.42 where the total bias drifts of the Z-axis accelerometers are plotted over the thermal resistance of the SOCIS. Therefore, although it is not certain how the heater voltage difference affects the temperature effect on the Z-axis accelerometer in the SOCIS, it is certainly desired to design a heater that has a low electrical resistance. The heater voltage difference can be calculated as:

$$V_{h,diff} = \sqrt{\frac{R_{heater} \cdot (T_{sur,max} - T_{sur,min})}{R_{th}}} \tag{2.23}$$

where R_{heater} is the electrical resistance of the heater, $T_{sur,max}$ is the maximum surrounding temperature, $T_{sur,min}$ is the minimum surrounding temperature, R_{th} is the total thermal resistance of the SOCIS, and $V_{h,diff}$ is the voltage difference between the heater voltages required to control to a temperature set point at $T_{sur,max}$ and at $T_{sur,min}$. Equation 2.23 is then plotted over R_{heater} at different R_{th} values and shown in Figure 2.43, given that $T_{sur,max}$ is 70 °C and $T_{sur,min}$ is -40 °C. Based on this plot, it was found that a smaller heater voltage difference can be obtained by reducing the electrical resistance of the heater and/or increasing the thermal resistance of the SOCIS. Therefore, the electrical resistance of the heater will need to be determined based on the given thermal resistance of the SOCIS and the required temperature-induced bias drift of the Z-axis accelerometer.

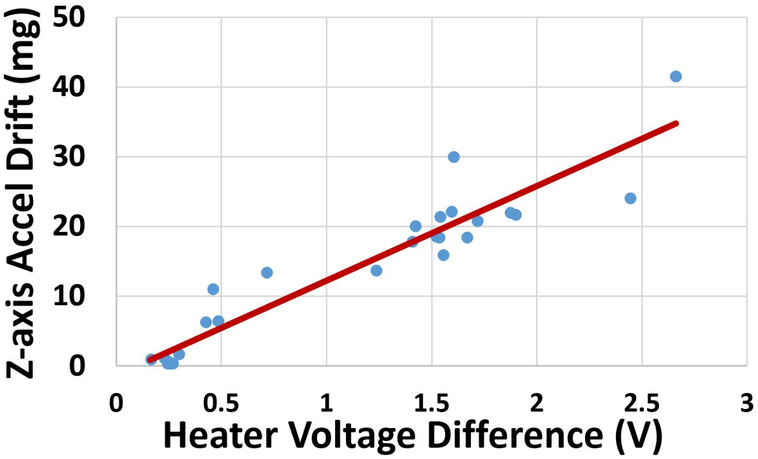

Figure 2.41: Total temperature-induced bias drifts of the Z-axis accelerometers in the SOCISs over the difference between the required voltages across the heater to control to a temperature set point at T_{sur} of -40 °C and T_{sur} of 70 °C.

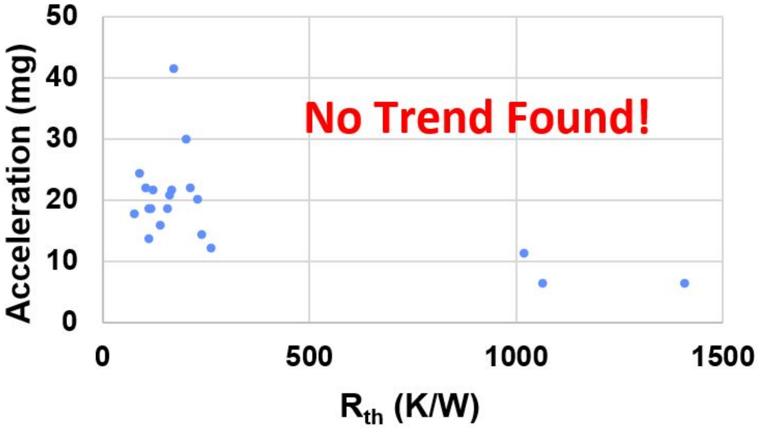

Figure 2.42: Total temperature-induced bias drifts of the Z-axis accelerometers over the thermal resistance of the SOCIS.

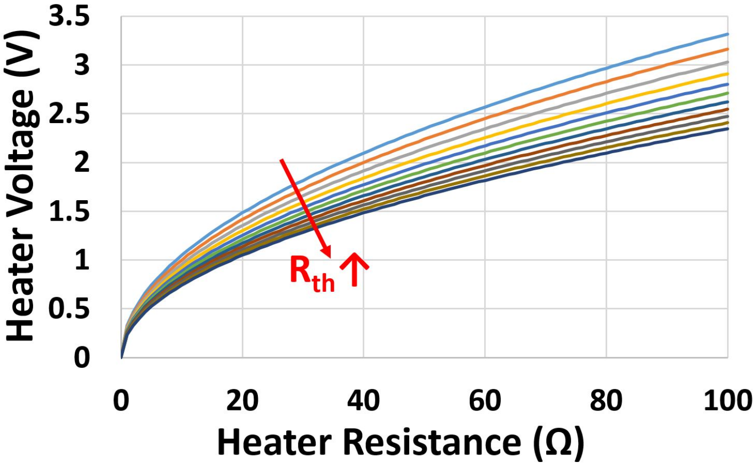

Figure 2.43: The difference between the required voltages across the heater to control to a temperature set point at T_{sur} of -40 °C and T_{sur} of 70 °C vs. the heater resistance at different total thermal resistances of the SOCIS.

2.5.3.2 Residual Temperature-Induced Bias Drifts in the SOCIS

The basic underlying assumption in the oven-control system is that if the temperature of the MEMS inertial sensors is perfectly controlled, then temperature-induced bias drifts in the inertial sensors will be completely eliminated. From a set of thermal-cycle experiments in the last few sections, however, it was found that residual temperature-induced bias drifts still remain during thermal-cycle tests even though the temperature of the inertial sensors were controlled accurately within around ±0.05 °C (or $1\sigma = 8$ m°C).

We believe there are three possible causes for the residual temperature-induced bias drifts. First, discrete electronic components that are required for the operation of the MEMS inertial sensors can be affected by the temperature fluctuation to cause the bias drift, as they are not oven-controlled. Second, the coefficient of thermal expansion (CTE) mismatch between the epoxy molding compound (EMC) package of the commercial IMU (7.9 ppm/K), silicon MEMS devices (2.6 ppm/K), and isolation stage (3.3 ppm/K) can cause temperature-induced stress on the inertial sensors. Finally, the low thermal conductivity of the glass isolation stage can create large temperature differences across the isolation stage, which in turn can cause temperature-induced stress on the MEMS inertial sensors. Furthermore, the temperature differences and stress will change as the surrounding temperature changes. In this section, details of the three possible causes for the residual temperature-induced bias drifts will be discussed.

Effect of Discrete Electronic Components Although the MEMS inertial sensors are oven-controlled in the SOCIS, other discrete electronic components, such as large capacitors that could not be included in the IC for their large sizes and are required for stable operations of the inertial sensors, will experience a wide range of temperature change, and this may cause the temperature-induced bias drifts in the SOCIS. Among the ICs that require large capacitors, a charge pump is the most critical component that would most significantly affect the bias drifts in the MEMS gyroscopes, since it provides a stable bias voltage for the gyroscopes [68]. Therefore, the effect of the bias voltage on the bias drifts of the gyroscopes and the effect of the temperature on the bias voltage will be examined.

In order to understand the effect of the bias voltage on the gyroscopes, the discrete capacitor was disconnected from the charge pump, and a lab power supply was directly connected to the charge pump to override the bias voltage. The voltage at the power supply was then changed from 15V to 35V to observe how the resonant frequencies and rate outputs of the 3-axis gyroscopes change. The results are shown in Figure 2.44, and they are normalized so that the average value of each of the plots is set to 0 ppm for the resonator frequencies and 0 °/h for the rate outputs. From the results, it was found that the resonant frequencies and the rate outputs change significantly as the bias voltage changes. The total changes in the resonant frequencies of the 3-axis gyroscopes range from 1000 to 1400 ppm, while the total changes in the rate outputs of the 3-axis gyroscopes range from 15,000 °/h to 60,000 °/h and those changes are nonlinear.

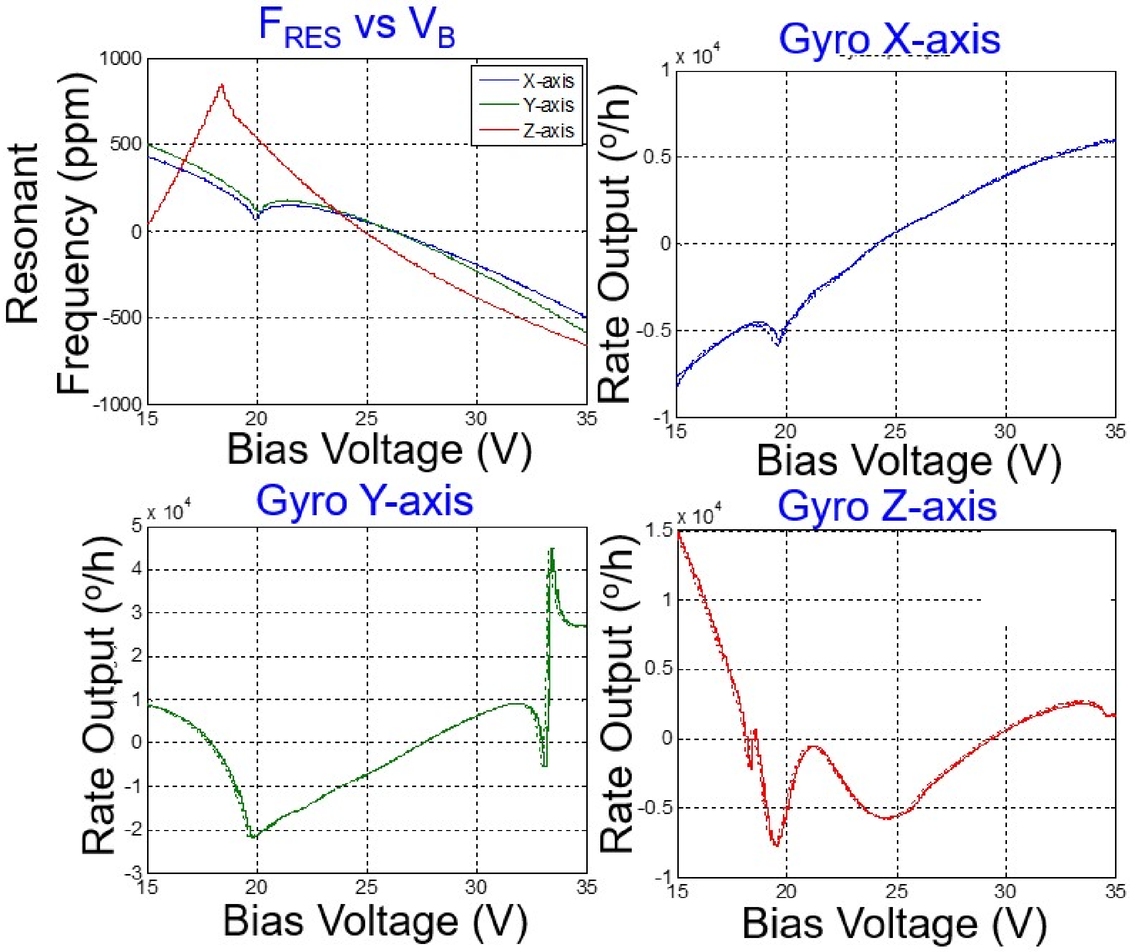

Figure 2.44: The sensitivity of resonant frequency and gyroscope rate output on the bias voltage.

Next, in order to understand the effect of the bias voltage during a thermal-cycle test, a thermal-cycle test was conducted at the bias voltage of 21 V, and the same test was repeated at 23 V, 25 V, 27V, and 29 V. The results are shown in Figure 2.44. Note that DC offsets in all results were eliminated to compare the results more effectively.

As a result, it was found that the temperature-induced bias drifts at different bias voltages show a consistent profile during the thermal-cycle tests. Therefore, as long as the bias voltage does not change during the thermal-cycle test, the temperature-induced bias drifts will be consistent regardless of the absolute value of the bias voltage.

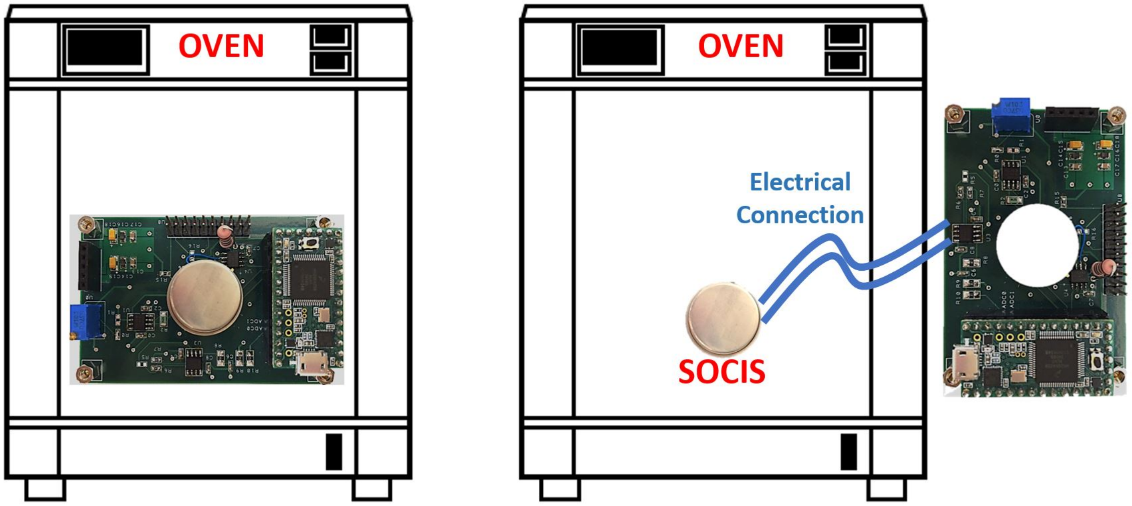

Figure 2.45: Normal test setup for a thermal-cycle test (left) and new test setup (right) to evaluate temperature effect on the discrete electronic components.

After the effect of the bias voltage on the gyroscopes was examined, another experiment was prepared in which the SOCIS was placed in the oven chamber for a thermal-cycle test while the PCB, which contains discrete electronic components for operations of the gyroscopes, was placed outside the oven chamber, in order to exclude the temperature effect on the electronic components, as shown in Figure 2.45. After that, the thermal-cycle test was conducted where the surrounding temperature changed from 0 °C to 60°C and the MEMS inertial sensors were oven-controlled at 80 °C. The outputs of the inertial sensors in the normal test setup (Figure 2.45(left)) and the new test setup (Figure 2.45(right)) are shown in Figure **??**. From the results, it was found that the temperature-induced bias drifts in both test setups are almost identical, although the outputs from the new test setup showed a higher noise level due to long electrical connections through which the SOCIS is electrically connected to the PCB. This indicates that the charge pump provides a stable bias voltage when the external capacitor for the charge pump is exposed to a wide range of temperature fluctuation.

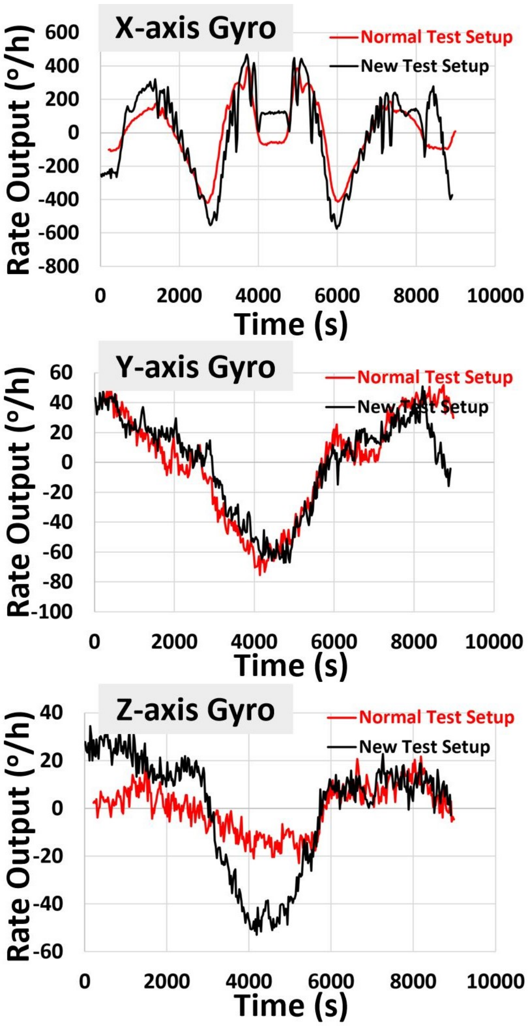

Figure 2.46: The outputs of the inertial sensors in the normal test setup and the new test setup.

Effect of Temperature Differences across the Isolation Stage In the SOCIS, the isolation stage is made of a thermally low-conductive material, usually around 1 W/m·K or less for low heat loss from the inertial sensors to the surrounding. This approach, however, can potentially cause temperature-induced stress on the inertial sensors due to temperature differences across the isolation stage when the surrounding temperature is much lower than the oven set temperature and changes over time. This temperature-induced stress can be negligible for the transducers that are relatively robust to mechanical stress, such as the crystal oscillator in the OCXO, but MEMS inertial sensors are known to be susceptible to the stress effect. Figure 2.47 shows the temperature distribution on the isolation stage and Figure 2.48 shows the calculated temperature differences between the side and the center of the isolation stage, and the temperature-induced stresses on the bottom surface of the MEMS inertial sensors as the surrounding temperature changes from -40 to 70 °C. According to the simulation results, the change in the maximum temperature-induced stress (δstress) is approximately 21 kPa and the change in the average temperature-induced stress (δstress) is approximately 8.3 kPa, or 0.13 N. In order to translate the stress to the bias drift, a test setup was prepared as shown in Figure 2.49, where a load is directly applied on the surface of MPU-6050 using a pressing bar to imitate the temperature-induced stress and stress is calculated using a strain gauge. It should be noted that since the inertial sensors are attached on the isolation stage through a small area in the center and the inertial sensors are oven-controlled at a constant value while the temperature distribution on the isolation stage alone changes to be deformed, it is reasonable to say that the stress experiment prepared in Figure 2.49 is a valid method to evaluate the temperature-induced stress on the inertial sensors. Based on the experimental result shown in Figure 2.50, it was found that the average stress change of 8.3 kPa can produce bias drifts up to 1,300 °/h during the thermal-cycle test.

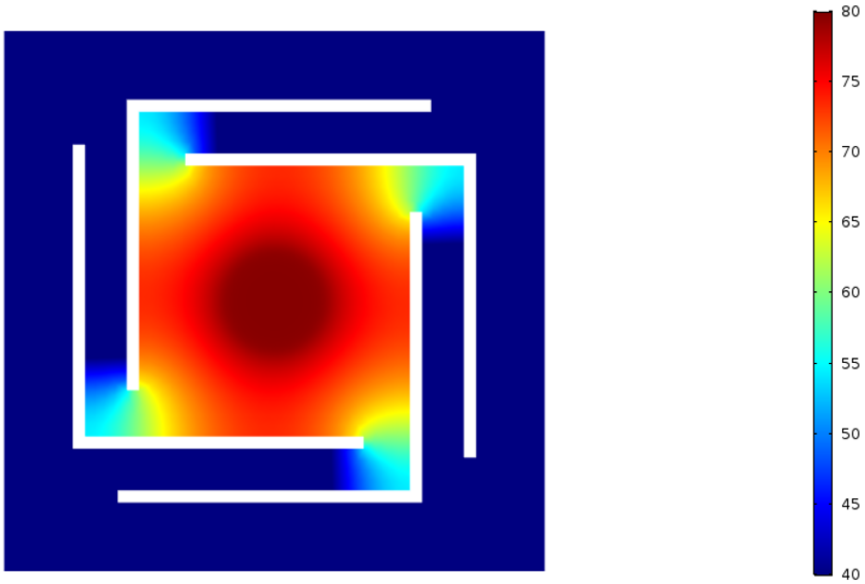

Figure 2.47: Temperature distribution on the isolation stage.

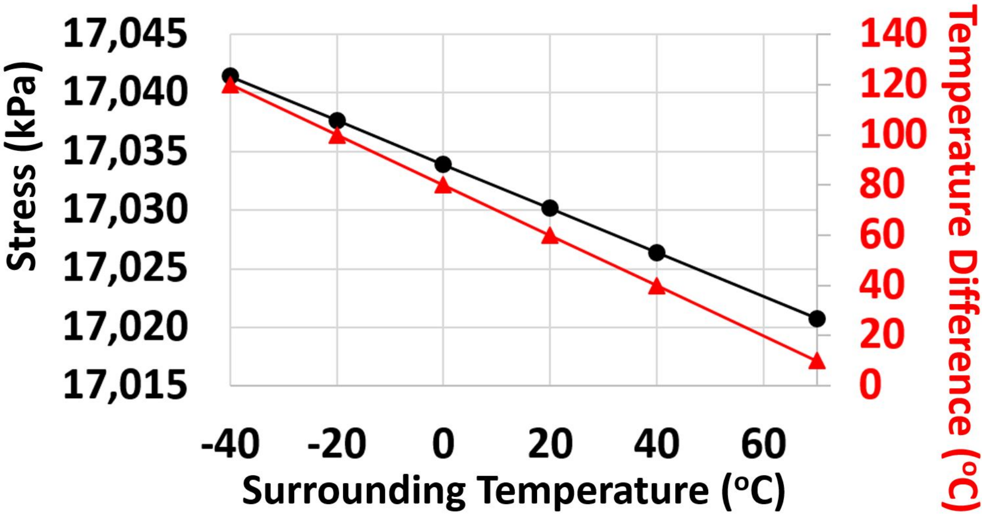

Figure 2.48: Simulation results: temperature differences between the side and the center of the isolation stage, and maximum temperature-induced stresses on the bottom surface of the IMU over the surrounding temperature.

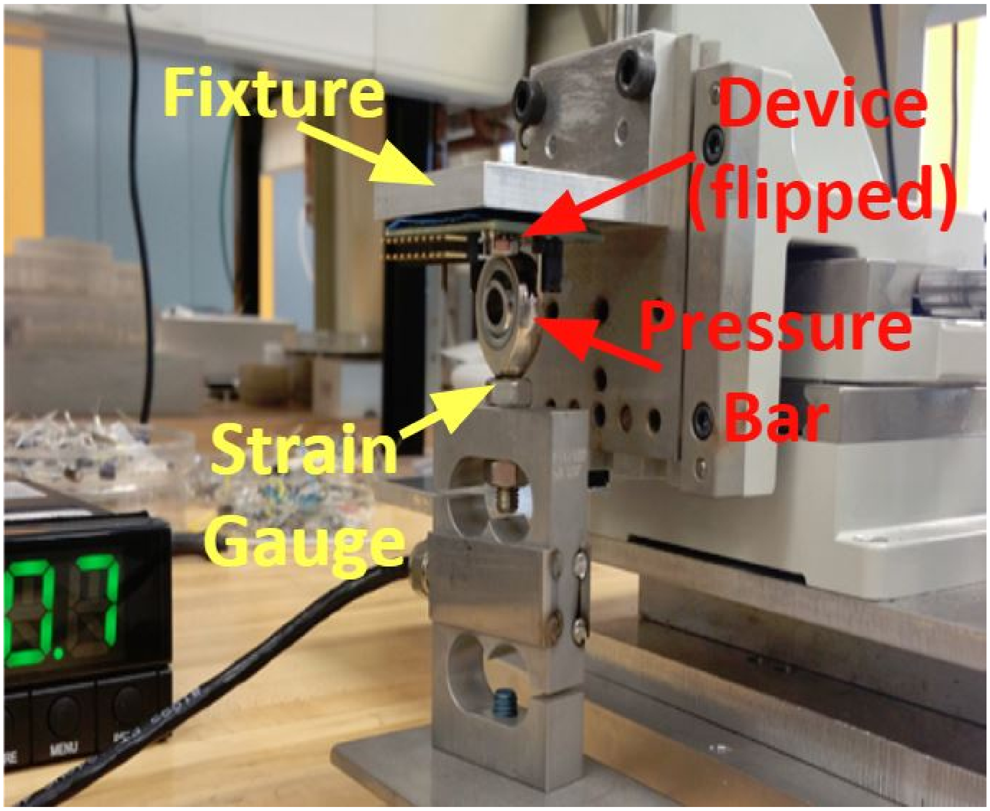

Figure 2.49: A test setup for measuring a mechanical stress effect on the bias drifts of the 3-axis gyroscopes in MPU-6050.

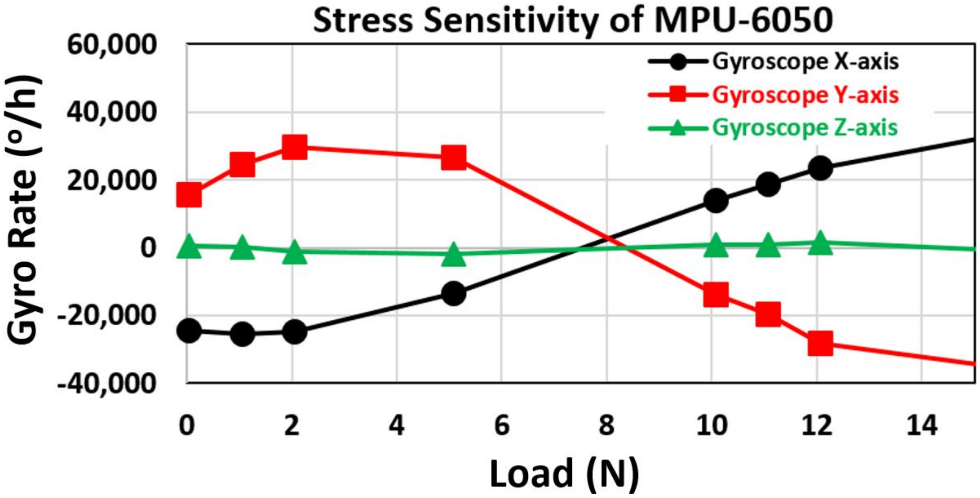

Figure 2.50: Experiment results: rate output vs mechanical stress on MPU-6050.

2.5.4 PCB Bending Stress on MEMS inertial sensors and SOCIS

As mentioned in the previous chapter, MEMS inertial sensors are susceptible to stress effect and one of the most common stresses during the INS operation is the PCB bending stress [37]. Therefore, it is important to quantify how susceptible the MEMS inertial sensors that were used in this study, MPU-6050, to the PCB bending stress through experiments. In order to quantify the PCB bending stress effect on the inertial sensors, a special PCB was designed, as shown in Figure 2.52. This PCB is designed as a cantilever beam where one end is anchored on a fixture (i.e., the main PCB) while the other end is suspended to have a high degree of flexibility and thus to induce a high strain on the PCB and the inertial sensors. A SOCIS is placed closer to the suspended end where the effect of the strain-induced stress can be observed clearly. Furthermore, two strain gauges (L2A-06-015LW-120 by VPG Micro-Measurements) are mounted on the front and back sides of the PCB right next to the SOCIS on the same transversal axis to measure the exact strain that would be induced on the SOCIS. For the strain measurements using the strain gages, a Wheatstone half-bridge was used as shown in Figure 2.51 where R_1 and R_4 are the strain gages while R_2 and R_3 are nominal resistors.

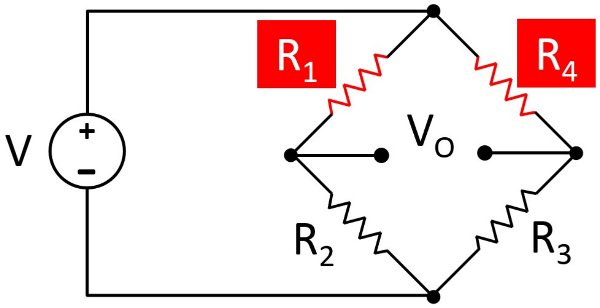

Figure 2.51: A Wheatstone half-bridge circuit for the strain gages. R_1 and R_4 are strain gages, while R_2 and R_3 are nominal resistors.

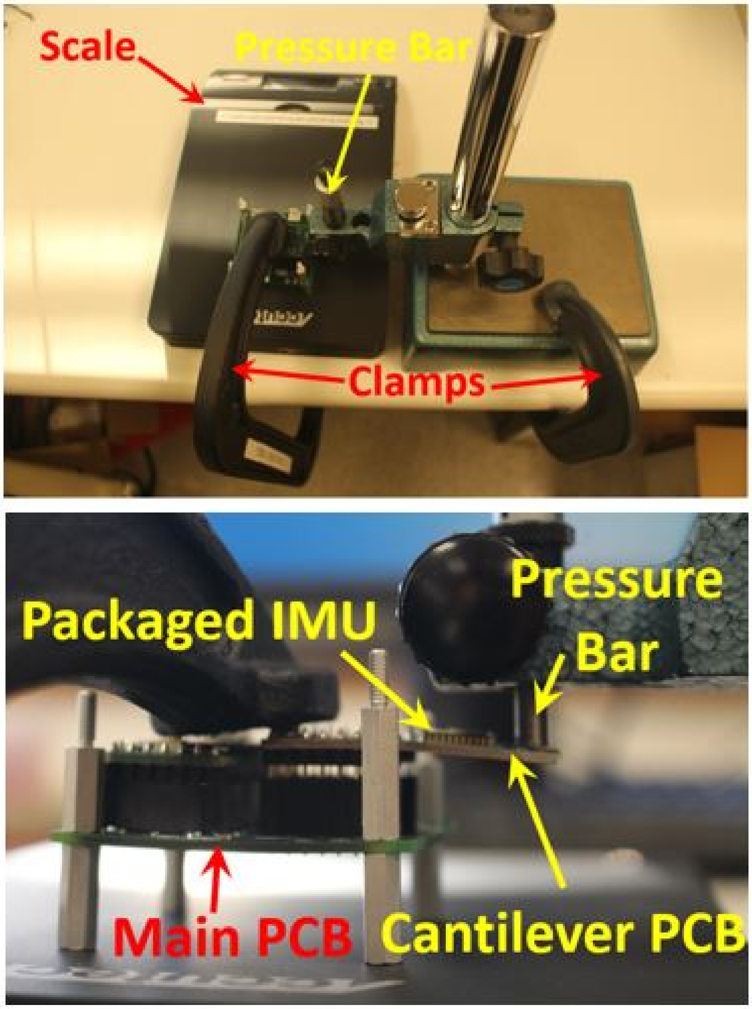

Figure 2.52: PCB Stress test setup: bird view (top) and side view (bottom).

Next, in order to induce the bending force on the cantilever PCB, we prepared a test setup as shown in Figure 2.52. One side of the cantilever PCB was fixed on the main PCB through electrical pins, and they were placed on a digital scale to measure an applied weight, which then would be converted to a force later. Furthermore, the fixed end of the cantilever PCB was fixed on a table by using a clamp to prevent it from being flipped over during the test. Finally, the suspended end of the cantilever PCB was pressed down by using a pressure bar to induce the weight from 0 to 2000 grams with an increment of 400 grams. In order to understand the effect of the PCB bending stress on the MEMS inertial sensors with and without the isolation stage, regular MPU-6050s (i.e., without the isolation stage) and SOCISs using MPU-6050s (i.e., with the isolation stage) were prepared and soldered on the cantilever PCBs. The measured strain value from the stain gage at each weight is converted to stress values as:

$$\sigma = E \cdot \epsilon \tag{2.24}$$

where σ is the PCB stress, E is Youngs modulus of the PCB, and ϵ is the PCB strain measured from the strain gages. The test results for eight 3-axis gyroscopes in MPU-6050s with the isolation stage and another eight 3-axis gyroscopes in MPU-6050s without the isolation stage are shown in Figure 2.53. Furthermore, the average bias drifts of the eight 3-axis gyroscopes during the experiment are summarized in Table 2.10. As shown, the bias drifts of the X-, Y-, and Z-axis gyroscopes were improved by 37, 18, and 92 times, respectively.

On the other hand, the test results from the 3-axis accelerometers in MPU-6050 were not analyzed, because the gravity factor is observed in all 3-axis accelerometers as the cantilever PCB is pressed down, and thus distinguishing the bias outputs measuring gravity from the bias drifts caused by the strain-induced stress is very difficult. Therefore, the PCB bending stress effect was analyzed on the 3-axis gyroscopes only.

Table 2.10: Averaged bias drifts of eight 3-axis gyroscopes during PCB bending experiments.

8 IMUs without isolation stage			8 IMUs with isolation stage		
X-axis	Y-axis	Z-axis	X-axis	Y-axsi	Z-axis
4930 $^\circ/h$	2420 $^\circ/h$	4274 $^\circ/h$	134 $^\circ/h$ (37x $\downarrow$)	135 $^\circ/h$ (18x $\downarrow$)	46.7 $^\circ/h$ (92x $\downarrow$)

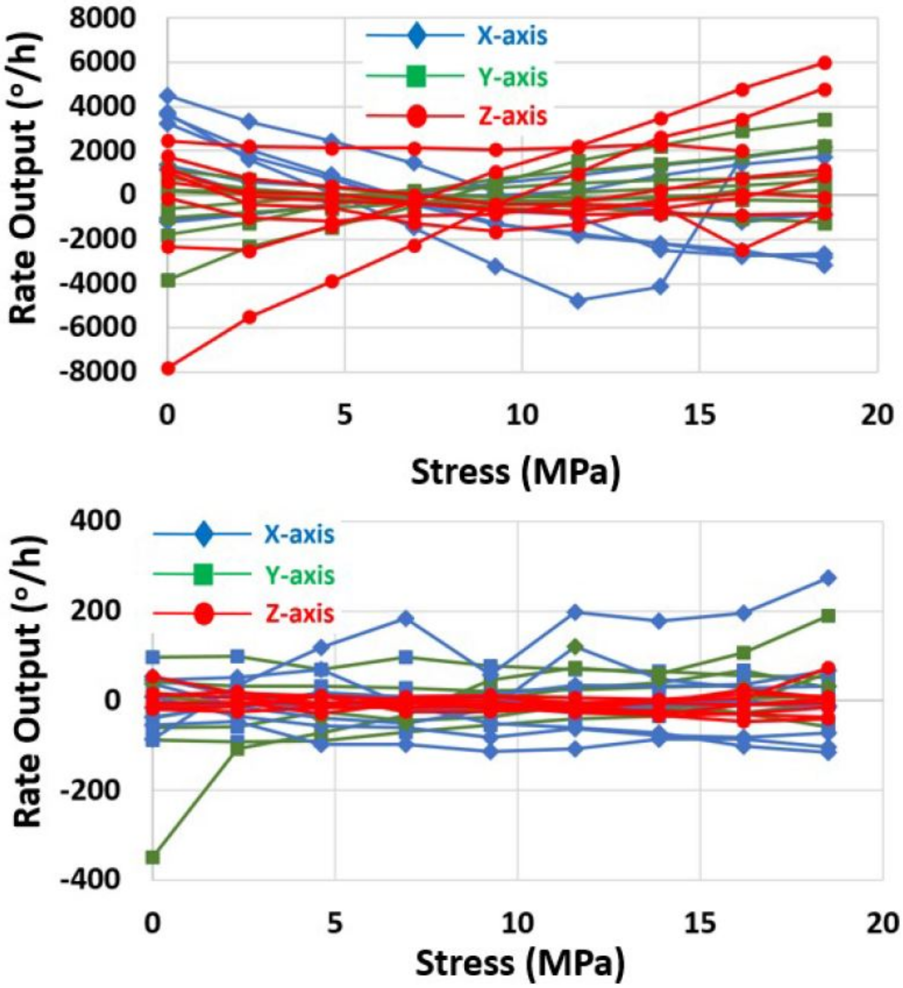

Figure 2.53: PCB Stress test results: without the isolation stage (top) and with the isolation stage (bottom). Note that the vertical scale of the bottom plot is 20x smaller than that of the top plot.

2.5.5 Temperature-Induced Position Error in Inertial Navigation System using SOCIS

In this section, an INS using the SOCIS is modeled to compute position errors over time in a hypothetical circumstance where temperature changes abruptly by 1.5 °C at time equal to zero. Such a hypothetical circumstance is a reasonable scenario that can happen when the system is moved from inside a building to outside during winter or summer, assuming that the temperature inside the building is well maintained to a moderate level. Furthermore, INSs using a standard Invensense MPU-6050 and an ideal MPU-6050, of which the noise level is the same as the standard one but the temperature effect is eliminated, are also modeled, and the position errors of these INSs are computed in the same condition and compared with the errors of the INS using the SOCIS. Noise metrics and the temperature-induced errors for each INS simulation are summarized in Table 2.11. Each INS simulation was repeated 50 times and averaged to calculate 3D position errors for 60 seconds. The 3D position errors for 60 seconds are plotted in Figure 2.54 and the position errors of the INSs at 60 seconds are summarized in Table 2.13. According to the simulation results, the INS using the ideal inertial sensors generated a position error of 22.7 m after 60 seconds. Furthermore, the INSs using the standard inertial sensors and the SOCIS generated the position errors of 83.5 m and 31.1 m, respectively, after 60 seconds. In other words, when compared with the INS using the ideal inertial sensors, the INSs using the standard inertial sensors and the SOCIS were degraded by a factor of 3.7 and 1.4, respectively. Finally, the position error of the INS using the SOCIS was improved by a factor of 2.7 than the position error of the INS using the standard inertial sensors.

Table 2.11: Gyroscopes noise and temperature-induced errors for standard inertial sensors, SOCIS, and ideal inertial sensors.

Metric		**Gyroscopes**		
		X	**Y**	**Z**
Temperature -induced error	**Standard**	±1906 $°/hr$	±3588 $°/hr$	±939.5 $°/hr$
	SOCIS	±500 $°/hr$	±712 $°/hr$	±83 $°/hr$
	"Ideal"	±0		
Noise performance	**Standard**	0.22 $°/\sqrt{hr}$ 4.78 $°/hr$	0.23 $°/\sqrt{hr}$ 3.81 $°/hr$	0.21 $°/\sqrt{hr}$ 1.86 $°/hr$
	SOCIS	0.24 $°/\sqrt{hr}$ 3.77 $°/hr$	0.24 $°/\sqrt{hr}$ 2.94 $°/hr$	0.21 $°/\sqrt{hr}$ 1.85 $°/hr$
	"Ideal"	0.24 $°/\sqrt{hr}$ 3.77 $°/hr$	0.24 $°/\sqrt{hr}$ 2.94 $°/hr$	0.21 $°/\sqrt{hr}$ 1.85 $°/hr$

Table 2.12: Accelerometers noise and temperature-induced errors for standard inertial sensors, SOCIS, and ideal inertial sensors.

Metric		**Accelerometers**		
		X	**Y**	**Z**
Temperature -induced error	**Standard**	±25.5 μg	±6.36 μg	±65.2 μg
	SOCIS	±1.08 μg	±0.95 μg	±8.6 μg
	"Ideal"	±0		
Noise performance	**Standard**	150 $\mu g/\sqrt{Hz}$ 21 μg	150 $\mu g/\sqrt{Hz}$ 22 μg	220 $\mu g/\sqrt{Hz}$ 29 μg
	SOCIS	170 $\mu g/\sqrt{Hz}$ 22 μg	160 $\mu g/\sqrt{Hz}$ 22 μg	230 $\mu g/\sqrt{Hz}$ 20 μg
	"Ideal"	170 $\mu g/\sqrt{Hz}$ 22 μg	160 $\mu g/\sqrt{Hz}$ 22 μg	230 $\mu g/\sqrt{Hz}$ 20 μg

Table 2.13: Temperature Effect on Inertial Navigation System with 1.5 °C thermal-shock

Unit	**Position error after 60 s (m)**
Standard IMU	83.5
SOCIS	31.1
”Ideal” IMU	22.7

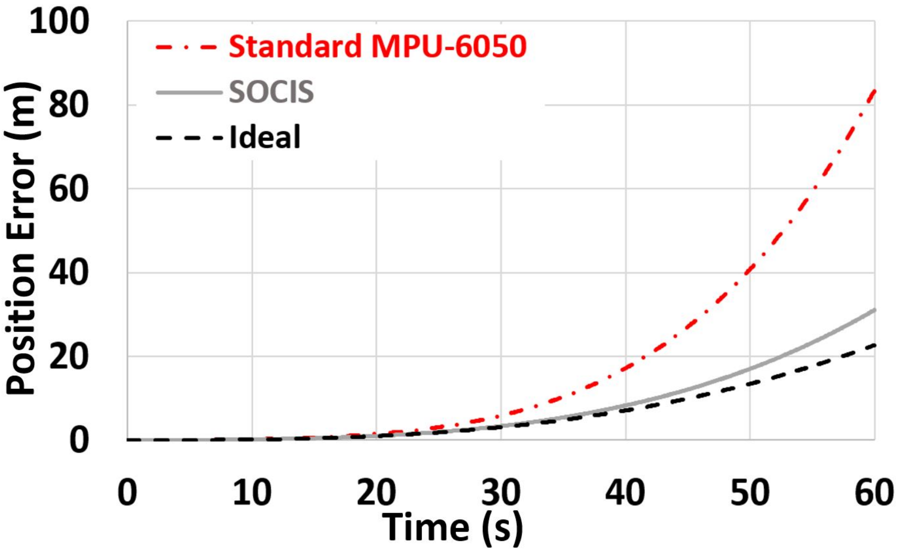

Figure 2.54: Position errors in INSs using a regular IMU, OCIS, and ideal IMU.

2.6 Limitations of the SOCIS

In previous sections, it was found that the temperature-induced stress due to temperature differences across the isolation stage would be the main contributor to temperature-induced error in the SOCIS during a thermal-cycle test. In order to minimize the temperature differences across the isolation stage, a high thermal conductivity material needs to be used for fabricating the isolation stage. However, this is not practical in the SOCIS, because the isolation stage has to be made of thermally low-conductive material to provide a good thermal isolation capability.

Another limitation of the SOCIS is a low degree of the design flexibility for the isolation stage, which limits the design to suspended beam structures (e.g., crab-leg structure) because a single isolation stage should be able to provide good thermal and mechanical isolation capabilities simultaneously. This will be disadvantageous in an application where the SOCIS is exposed to high-g impacts since the suspended beam structure of the isolation stage is known to be susceptible to the shock impact.

CHAPTER III

Double Isolation Stage Oven-Controlled Inertial Sensors

The SOCIS in Chapter II has successfully mitigated environmental effects on the MEMS inertial sensors including the effects of temperature and mechanical stress with significantly reduced power consumption by using a single micro-machined isolation stage [57, 44, 36]. In this system, however, the design flexibility of the isolation stage is greatly limited, due to trade-offs between the thermal and mechanical isolation capabilities [36]. Accordingly, the structure of the isolation stage has to unavoidably use a suspended beam structure, such as a crab-leg structure, and therefore, the design becomes vulnerable to high-g shock impacts. Furthermore, since the isolation stage is made of low thermal conductivity material, temperature differences across the isolation stage will be high and change as the surrounding temperature changes, causing temperature-induced stress on inertial sensors. Finally, the fabrication process for such an isolation stage will be more complicated yet less sophisticate than the standardized fabrication process for silicon and the material will be less robust against a shock impact that silicon. Therefore, in this chapter, a new method to address these limitations and disadvantages of the SOCIS, the double isolation stage oven-controlled inertial sensors (DOCIS), is proposed and its details will be discussed.

3.1 Double Isolation Stage Oven-Controlled Inertial Sensors

As an effort to address the limitations of the SOCIS, a double isolation stage oven-controlled inertial sensors (DOCIS) is proposed in this chapter. In the DOCIS, as the name indicates, two isolation stages—thermal isolation stage and mechanical isolation stage—are utilized to isolate thermal and mechanical effects from the MEMS inertial sensors independently. The mechanical isolation stage is a micro-machined structure made of silicon, while the thermal isolation stage is a thin substrate made of low thermal conductivity material.

The design and the fabrication steps for the mechanical isolation stage are almost identical to those of the isolation stage in the SOCIS, except that the mechanical isolation stage in the DOCIS is made of silicon. On the other hand, in order to design the thermal isolation stage, selecting an appropriate material for the isolation stage is one of the most important processes. Among many available materials, the aerogel was selected for its extremely low thermal conductivity of 0.01-0.03 $W/m \cdot K$. The most typical aerogel is silica aerogel and is formed by reducing the density of silicon by more than 80% through the sol-gel process [69]. However, the mechanical durability of the silica aerogel tends to degrade proportionally compared to that of silicon, thus making the material less preferable in certain applications where the aerogel can be exposed to a high mechanical impact. In order to address this issue, a few studies have developed a cross-linked polyimide (PI) aerogel where the aerogel is cross-linked with polyimide to enhance mechanical durability while thermal conductivity remains comparable to that of the silica aerogel [69]. More details on the aerogel will be discussed in later sections.

The schematic of the DOCIS is shown in Figure 3.1. A thin PI aerogel substrate is first attached to an LCC package to provide thermal insulation. After that, an RTD and a heater are deposited and patterned on a silicon substrate, while the bottom surface of the silicon substrate is patterned and dry-etched (DRIE) to form an array of square bonding pads, through which the attachment of the silicon substrate on the aerogel substrate is established. The purpose of the array of square bonding pads is to reduce the contact area between the silicon and the aerogel substrates so that heat loss from the silicon substrate across the aerogel substrate can be minimized. The silicon substrate is then optionally dry-etched to form a suspended beam structure on each side to provide a mechanical isolation capability, and attached on the aerogel substrate using adhesive. After this, a MEMS inertial sensor is attached on the silicon isolation stage using adhesive, and electrical connections between the MEMS inertial sensor and electrical pads of the LCC package are established using thin bonding wires to minimize heat loss through electrical connections. Finally, a thin-film getter is deposited on a package lid, and the LCC package is vacuum-sealed.

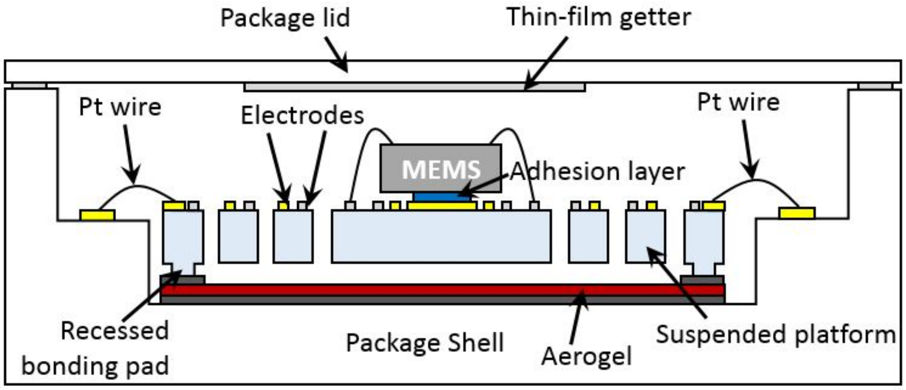

Figure 3.1: Schematic of the DOCIS.

The DOCIS is expected to provide three beneficial outcomes: small or negligible temperature differences across the mechanical isolation stage, a high degree of design flexibility for the mechanical isolation stage, and reduced mounting stress.

3.1.1 Temperature Differences across the Isolation Stage in the DOCIS

In order to understand the effect of thermal conductivity of the isolation stage on the temperature-induced stress on the MEMS inertial sensors, a set of simulations was conducted where the MEMS inertial sensors were controlled at 80 °C while the surrounding temperature was thermal-cycled from -40 $^{\circ}C$ to 70 $^{\circ}C$. Furthermore, in the simulations, the mechanical isolation stage in the DOCIS was designed to be the same as the isolation stage in the SOCIS for a direct comparison.

Figure 3.2(a) shows the temperature distribution on the silicon mechanical isolation stage at the surrounding temperature of -40 °C. Also, Figure 3.2(b) shows the temperature difference between the highest temperature, which is measured at the center of the isolation stage, and the lowest temperature, which is measured around the side and the corner of the isolation stage, over the surrounding temperature. Finally, Figure 3.3 shows the temperature-induced stress on the top surface of the MEMS inertial sensors (σ_{IMU}) over the surrounding temperature. Based on the simulation results, it was found that not only the temperature differences were reduced significantly, but the stress on the inertial sensors, $\Delta\sigma_{IMU}$ is also reduced significantly by a factor of 62 (i.e., from 21 kPa to 0.34 kPa), when compared to $\Delta\sigma_{IMU}$ in the SOCIS in Chapter II. Therefore, these simulation results suggest that the DOCIS would generate much lower temperature-induced bias drifts than the SOCIS does.

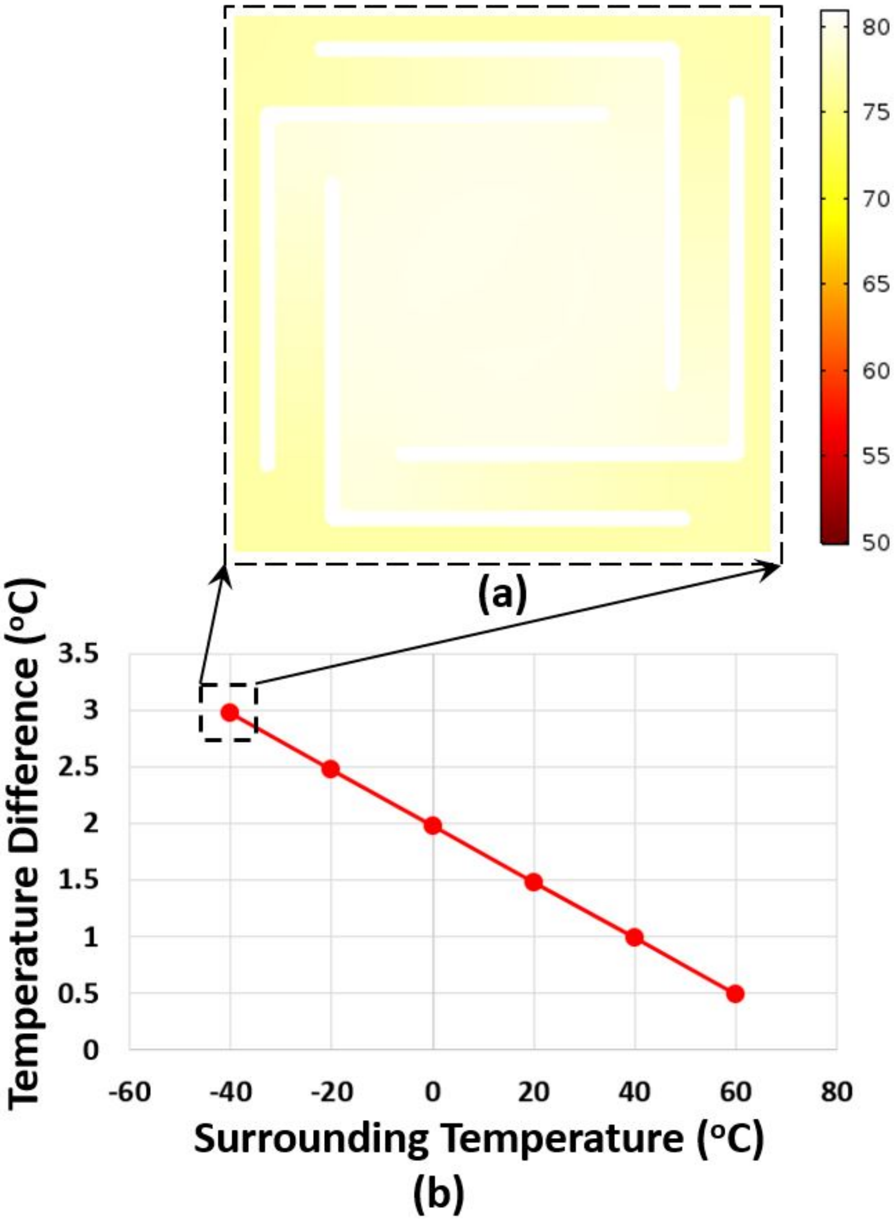

Figure 3.2: (a) Temperature distribution on the silicon mechanical isolation stage in the DOCIS at -40 °C and (b) the temperature difference over the surrounding temperature.

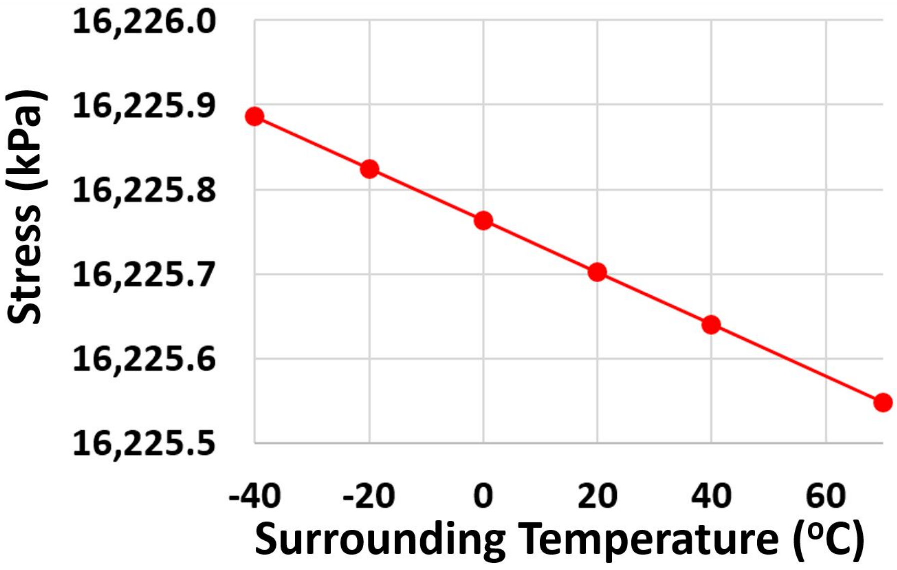

Figure 3.3: Stress on the MEMS inertial sensors in the DOCIS over the surrounding temperature.

Additionally, in order to generalize the effect of thermal conductivity of the isolation stage on the temperature-induced stress on the MEMS inertial sensors, the thermal conductivity of the material of the thermal isolation stage was changed from 0.03 $W/m \cdot K$ to 130 $W/m \cdot K$ and $\Delta\sigma_{IMU}$, which is the difference between the stress at the surrounding temperature of -40 °C and the stress at the surrounding temperature of 70 °C, was calculated at each thermal conductivity. As shown in Figure 3.4, $\Delta\sigma_{IMU}$ is inversely proportional to the thermal conductivity of the thermal isolation stage, and therefore a lower thermal conductivity is desirable for the material, of which the thermal isolation stage is made, to reduce the temperature-induced stress on the MEMS inertial sensors.

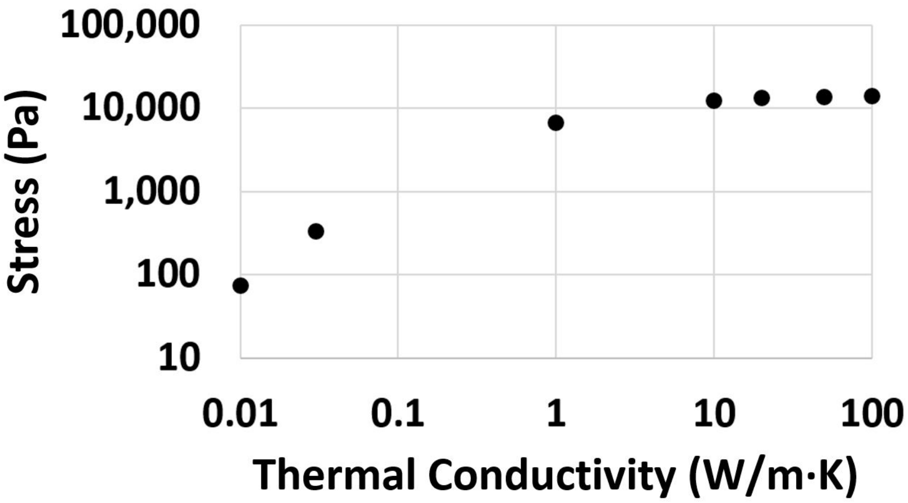

Figure 3.4: $\Delta\sigma_{IMU}$ on the MEMS inertial sensors over the thermal conductivity of the isolation stage.

3.1.2 Design flexibility of the Mechanical Isolation Stage in the DOCIS

Unlike the SOCIS where both thermal and mechanical effects on the MEMS inertial sensors are isolated by a single isolation stage, the thermal and mechanical effects are isolated by two individual isolation stages in the DOCIS, respectively. As a result, various designs will be available for the mechanical isolation stage. Figure 3.5 shows how the thermal resistance of the SOCIS and the DOCIS changes as the length of the crab-leg beams increases. From this simulation result, it was confirmed that the thermal resistance of the SOCIS changes dramatically with the length of beams, while the change in the thermal resistance of the DOCIS is almost negligible. Therefore, this indicates that the design of the mechanical isolation stage in the DOCIS will be much more flexible than that in the SOCIS and more design variations will be possible as shown in Figure 3.6.

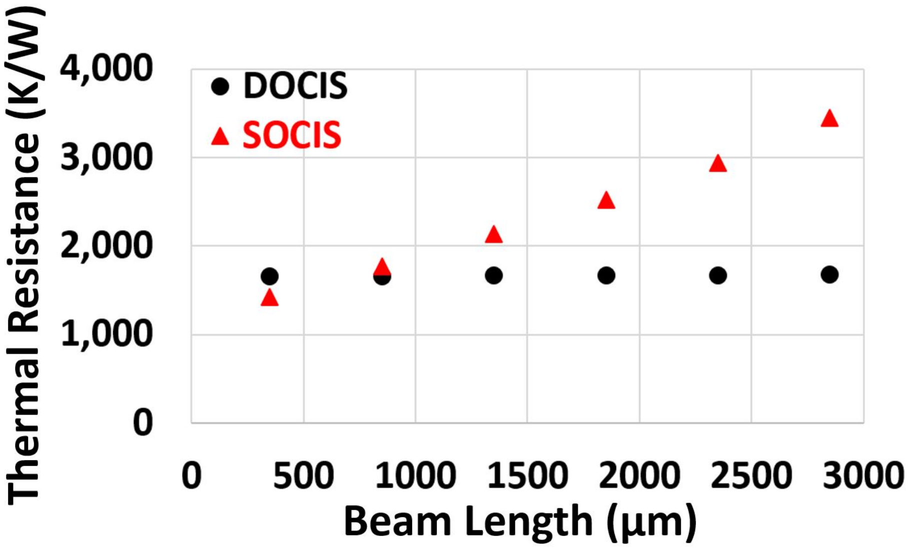

Figure 3.5: Thermal resistance of the SOCIS and DOCIS over the length of crab-leg beams.

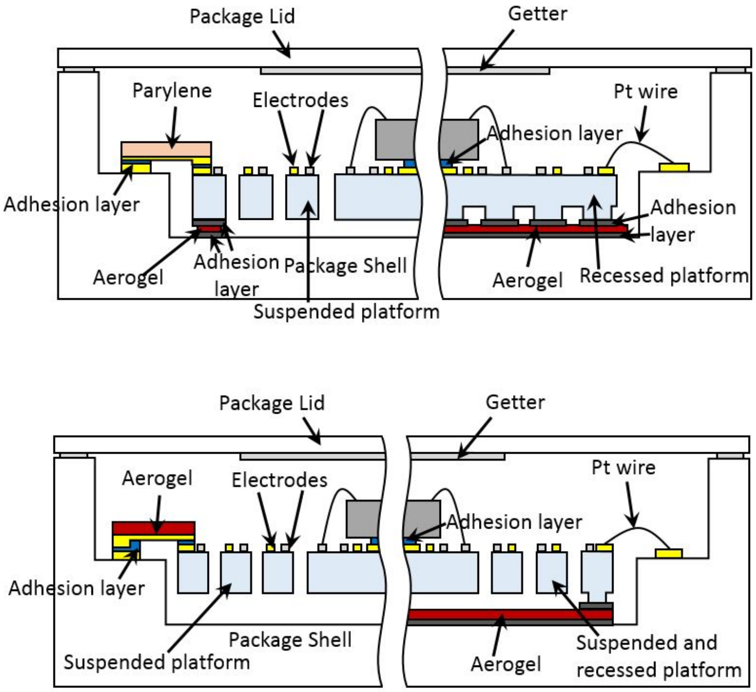

Figure 3.6: Examples of design variations for the DOCIS.

3.1.3 Mounting Stress on Inertial Sensors in the DOCIS

Another potential advantage of the DOCIS over the SCOIS is reduced mounting stress on the MEMS inertial sensors. Since most MEMS inertial sensors are made of silicon, if an isolation stage, on which the inertial sensors are attached, is made of a different material other than silicon, such as glass in the SOCIS, then CTE mismatch between the two materials can induce initial mounting stress on the inertial sensors. As a result, the mounting stress may degrade the performance of the inertial sensors. Furthermore, this type of stress will not be reversible nor compensatable. On the other hand, because the isolation stage in the DOCIS is made of silicon, the mounting stress on the MEMS inertial sensors will be smaller.

In order to verify this, the mounting stress in the SOCIS, where the CTE mismatch between the silicon MEMS inertial sensor die (2.6 ppm/K) and the glass substrate (3.2 ppm/K) is 0.6 ppm/K, was compared with the mounting stress in the DOCIS in a simulation. As a result, it was found that the mounting stress in the DOCIS (i.e., the maximum stress on the interface between the IMU and the adhesive) is 16.2 MPa at the surrounding temperature of -40 °C, and that in the SOCIS is 16.5 MPa at the same surrounding temperature, while the IMU was oven-controlled at 80 °C and the reference process temperature in the simulation was set to 150 °C, which is the curing process temperature for the adhesive used in this study. Therefore, the mounting stress on the MEMS inertial sensors in the DOICS was reduced by 300 kPa than that in the SOCIS. This stress would be further reduced by replacing the adhesive with a product that has a similar CTE as that of silicon, such as a glass frit.

3.2 Temperature Isolation Capability of the DOCIS

As discussed in previous sections, an individual temperature isolation stage, which is made of PI aerogel, is used to provide thermal isolation in the DOCIS. In this section, we will discuss more details about the temperature isolation stage and the overall temperature isolation capability of the DOCIS, including the material properties of aerogel and the thermal resistance analysis in the DOCIS.

3.2.1 Material Properties of Aerogel

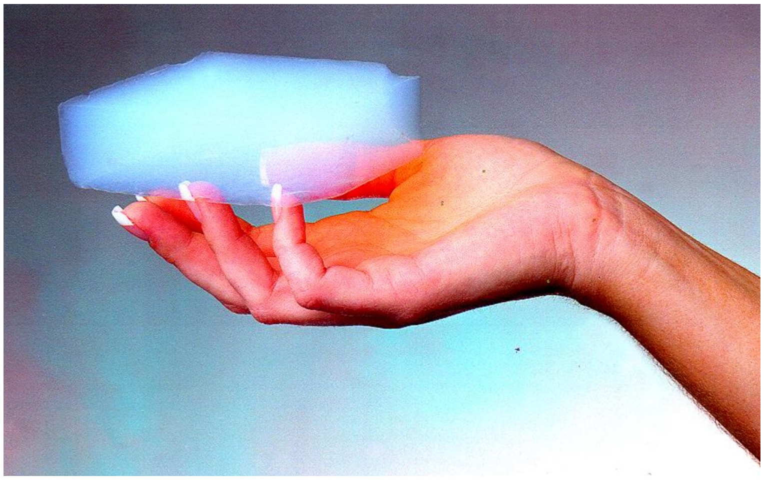

Figure 3.7: Porous silica aerogel [70].

Aerogel is one of the lightest materials known and can be made of various materials by replacing more than 80-90% of the material with air, which makes the aerogel a porous solid material. Figure 3.7 shows the most typical example of the aerogel—silica aerogel—which is made of silicon. The porosity of the material is achieved through a process called the sol-gel process shown in Figure 3.8. In this process, silicon (sol) is liquefied to form a precursor, and the precursor is then hydrolyzed and condensed to form a solid frame network (gel). If the gel is dried in the ambient environment to evaporate the liquid in the gel, the solid frame network will collapse due to capillary force and thus form a very dense material called silica xerogel. If the xerogel is heated at a certain condition, this can form a very dense ceramic. On the other hand, if the gel goes through a process called supercritical drying, during which the gel is in a supercritical phase and thus becomes a gas without evaporation, the gel turns into a silica aerogel. Figure 3.9 shows a phase diagram that describes the supercritical drying process. In general, materials exist in one of the three phases of solid (S), liquid (L), and gas (G), and different materials exhibit different phase diagrams. Since the phase is a function of the pressure and temperature, if either of the two variables changes, then the phase of the material may also change. Typical phase changes include evaporation (L → G), condensation (G → L), freezing (L → S), melting (S → L), sublimation (S → G), and deposition (G → S). Among these phase changes, evaporation and condensation between gas and liquid would happen until the pressure and temperature reach the critical point, beyond which those two-phase changes would not happen anymore. Instead, the material becomes a supercritical fluid (SCF) where distinct liquid and gas phases do not exist anymore. Furthermore, if the pressure level surrounding the material in the SCF phase were dropped with no change in temperature, then most particles in the material will become a gas. Finally, this gas is cooled down to room temperature to become silica aerogel. Since the supercritical drying process does not involve the evaporation process, which would collapse the frame network, the remaining frame network will maintain its original structure, while most particles of the material will become gases during the supercritical drying. Therefore, the material will become extremely porous, and the physical properties, such as thermal conductivity, will change significantly, while its chemical properties will remain the same. The density of silica aerogel is normally below 20 % of that of silicon, and thermal conductivity is reduced by three to four orders of magnitude. Therefore, even a thin silica aerogel substrate will be able to provide good thermal insulation, as shown in Figure 3.10.

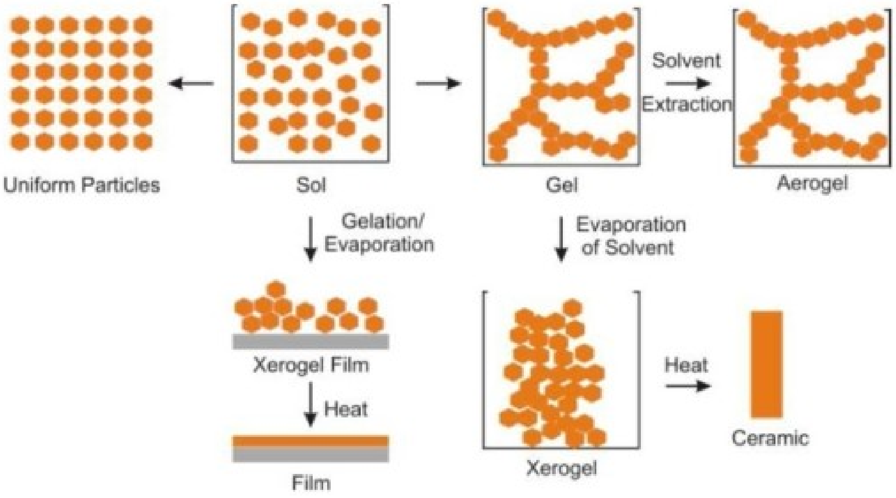

Figure 3.8: Sol-gel process [71].

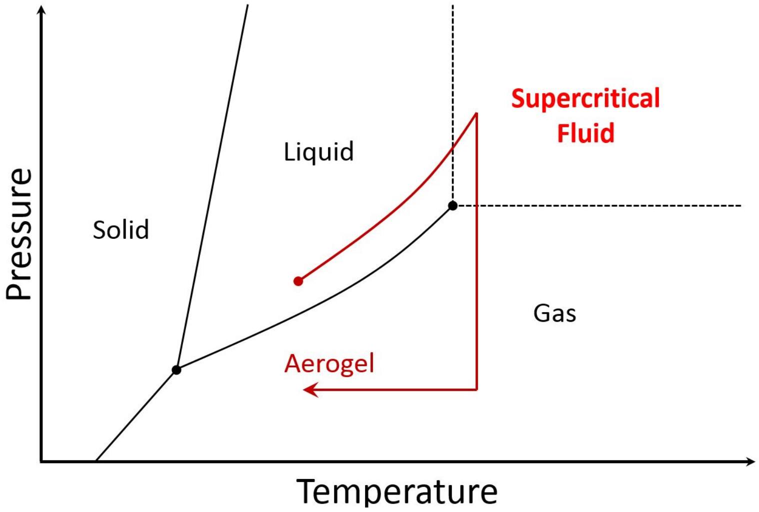

Figure 3.9: Critical dehydration process in a phase diagram.

Figure 3.10: Extremely low thermal conductivity of silica aerogel [70].

Silica aerogel, however, becomes fragile as the density reduces, and this makes the silica aerogel not suitable for applications where the aerogel is exposed to high mechanical impacts. In order to address this issue, some studies made efforts to use inherently stronger materials than silicon to make stronger aerogels but the Young's modulus and mechanical yield strength of these aerogels were not very much improved [72]. On the other hand, there have been studies to reinforce the silica aerogel structure by "cross-linking" the aerogel with polyimide [69]. Cross-linking is a process in which molecular chains in one material are linked to other molecular chains in another material through a physical or chemical process. As a result, the cross-linking process enhanced the mechanical strength of silica aerogel by more than two orders

Table 3.1: PI aerogel properties [73].

Property	Value	Property	Value
Thermal Conductivity	0.03 W/m·K	Adhesive Bonding	Yes
Density	0.2 g/cm^3	Cuttable, Sewable	Yes
Temperature Limit	240 °C	Metallizable	Yes
Tensile Strength	8.1 MPa	Young's Modulus	76 MPa
CTE	20 ppm/°C	Surface Resistivity	$>10^{13}\Omega/sqaure$

of magnitude [69].

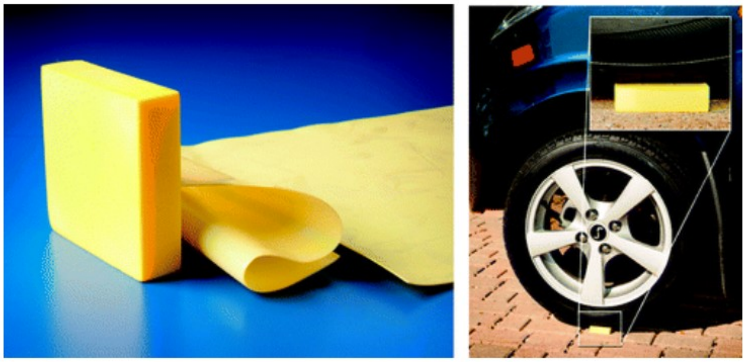

Figure 3.11: PI aerogel [69].

Cross-linked PI aerogel, developed by NASA Glenn Research Center, is shown in Figure 3.11. PI aerogel is mechanically robust and a low thermal conductivity material. Furthermore, the material can be machined and is waterproof so that dry/wet processes or a bonding process using wet adhesives can be conducted on this material, if necessary. The material properties are summarized in Table 3.1.

To summarize, the PI aerogel is expected to provide the following advantages:

- A thin layer of a PI aerogel substrate will be able to provide a good thermal isolation capability due to its extremely low thermal conductivity.
- A thin layer of a PI aerogel substrate will be able to survive high shock impacts.
- The PI aerogel substrate can be attached by using eutectic or adhesive bonding methods.

- Thin-film metal layers can be deposited and patterned on the PI aerogel substrate.
- The PI aerogel substrate can be machined and cut to an appropriate size.
- High-temperature fabrication/assembly processes can be performed for the PI aerogel.

3.2.2 Thermal Resistance Analysis of the PI Aerogel Substrate

Since the contact area between the mechanical isolation stage and the aerogel temperature isolation stage is equal to the area of the array of square bonding pads, which are formed by etching the bottom surface of the mechanical isolation stage, the thermal resistance due to the heat loss through the aerogel isolation stage can be calculated as follows:

$$R_{ag} = \frac{1}{n_{pad}} \cdot \frac{t_{ag}}{k_{ag} A_{ag}} \tag{3.1}$$

where R_{ag} is the thermal resistance due to the heat loss through the aerogel isolation stage, n_{pad} is the number of the square bonding pads, t_{ag} is thickness of the PI aerogel in m, k_{ag} is the thermal conductivity of the PI aerogel in $W/m \cdot K$, A_{ag} is the contact area between one of the square bonding pads and the PI aerogel in m^2, and sizes of the bonding pads are assumed to be the same. According to Equation 3.1, if the number or the size of the bonding pads increases, then the thermal resistance will decrease. Furthermore, if the thickness of the aerogel substrate increases, then the thermal resistance will increase as well.

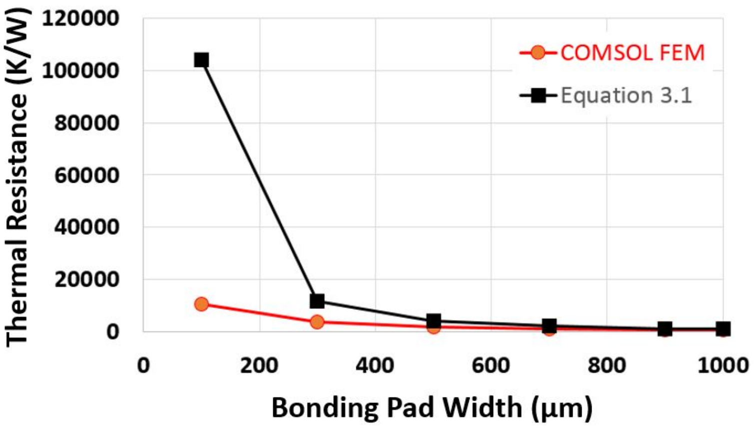

Figure 3.12: Calculated thermal resistances using Equation 3.1 and COMSOL FEM simulation.

In order to verify the analysis, a COMSOL Multiphysics FEM simulation was conducted to compute the thermal resistance of the aerogel isolation stage and compare the result with the calculated thermal resistance using Equation 3.1. The results are shown in Figure 3.12 where it was found that the calculated thermal resistance using Equation 3.1 does not match the thermal resistance computed using the FEM simulation. This is because the heat that was generated from the heater transfers not only through the aerogel substrate in a vertical direction, but also along the aerogel substrate in a horizontal direction. Therefore, although the actual contact area between the mechanical isolation stage and the aerogel temperature isolation stage is small, the effective contact area will be much larger than the actual contact area. Figure 3.13 describes two examples that have the same actual contact area but different effective area. The substrates in Figure 3.13(a) and (b) consist of PI aerogel alone, and PI aerogel coated with a 3000 μm-thick Au layer on the aerogel (i.e., it will have a higher thermal conductivity than that of PI aerogel), respectively. In Figure 3.13(b), due to the high thermal conductivity of the Au layer, heat spread in the longitudinal direction is significant that the effective width, w_{eff}, becomes much larger than the width of a pad, w_{pad} and comparable to the width of the aerogel substrate, w_{sub} (i.e., $w_{pad} \ll w_{eff} \simeq w_{sub}$). On the other hand, in Figure 3.13(a), heat spread in the longitudinal direction is relatively narrower than that in Figure 3.13(b), and thus the effective width, w_{eff}, is smaller than the width of the aerogel substrate (i.e., $w_{pad} < w_{eff} \ll w_{sub}$). Therefore, the effective width will become smaller and closer to the actual contact width, as the longitudinal thermal conductivity of the substrate decreases, while it will become larger and closer to the substrate width, as longitudinal thermal conductivity in the substrate increases.

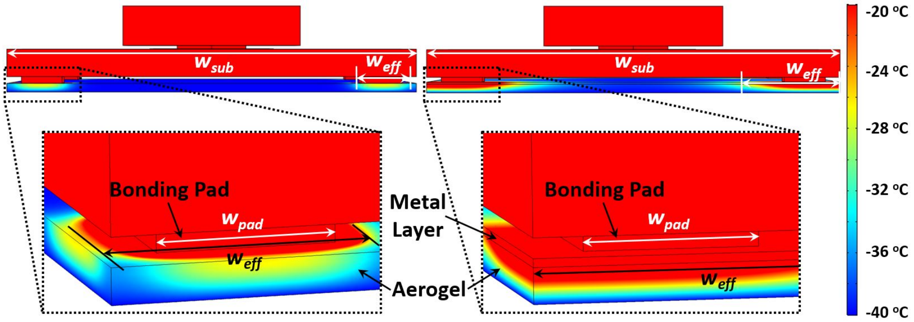

(a) (b)

Figure 3.13: Effective contact area: (a) PI aerogel alone, and (b) PI aerogel covered with metal layer.

The effective width, w_{eff}, of one of the square bonding pads can be expressed as:

$$w_{eff} = c \cdot w_{sub} (0 < c \leq 1) \tag{3.2}$$

where w_{eff} is the effective width of a bonding pad, w_{sub} is the width of a square aerogel substrate, and c is a scale factor that is determined by the thickness and thermal conductivity of the substrate. Furthermore, the thermal resistance through the bonding pads and the aerogel substrate can be calculated as:

$$R_{ag} = \frac{1}{n_{pad}} \cdot \frac{t_{ag}}{k_{ag} w_{eff}^2} = \frac{1}{n_{pad}} \cdot \frac{t_{ag}}{k_{ag} c^2 w_{sub}^2} \tag{3.3}$$

where k_{ag} is the thermal conductivity of the aerogel, and t_{ag} is the thickness of the aerogel substrate. Assuming the thickness of the aerogel substrate is 125 μm, the thermal resistance of the configuration in Figure 3.13(b) was calculated and plotted over the width of each of the bonding pads as shown in Figure 3.14. From the result, it was found that the thermal resistance is significantly affected by the actual contact area.

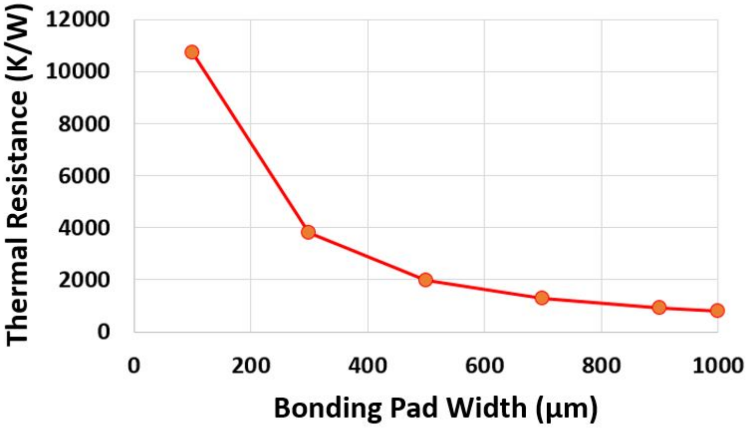

Figure 3.14: Thermal resistance vs the width of each of the bonding pads for Figure 3.13(b).

On the other hand, assuming a 3000 $\mathring{A}$-thick Au metal layer is deposited on the 125 μm-thick PI aerogel for eutectic bonding as in Figure 3.13(a) and the number of bonding pads is four, the thermal resistance of the configuration in Figure 3.13(a) was calculated and plotted over the width of each of the bonding pads and the result is shown in Figure 3.15. According to the result, the effect of the actual contact area on the total thermal resistance in this configuration was much less significant than that in Figure 3.13(b), due to the presence of the 3000 $\mathring{A}$-thick Au layer.

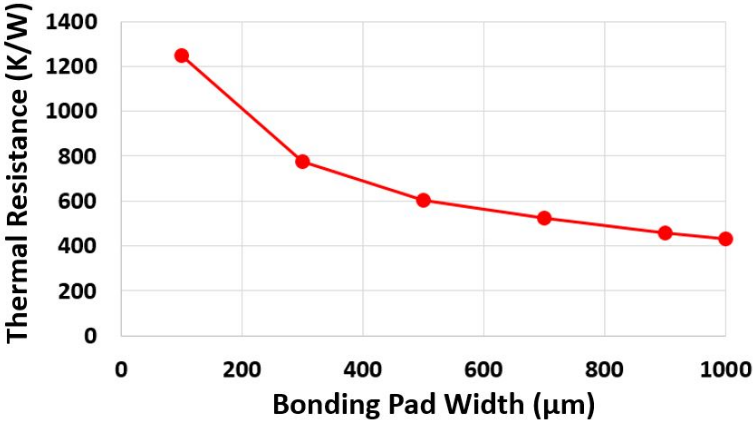

Figure 3.15: Thermal resistance vs width of each of the bonding pads for Figure 3.13(a).

Furthermore, in order to understand the effect of the thickness of the deposited metal layer on the thermal resistance, the thickness of the metal layer was changed from 100 to 1000 Åand the thermal resistance was measured in a simulation, and the result is shown in Figure 3.16. In this simulation, the number and the width of each of the bonding pads were four and 500 μm, respectively. Therefore, the width of the bonding pads and the thickness of the metal layer should be as small as possible to obtain high thermal resistance.

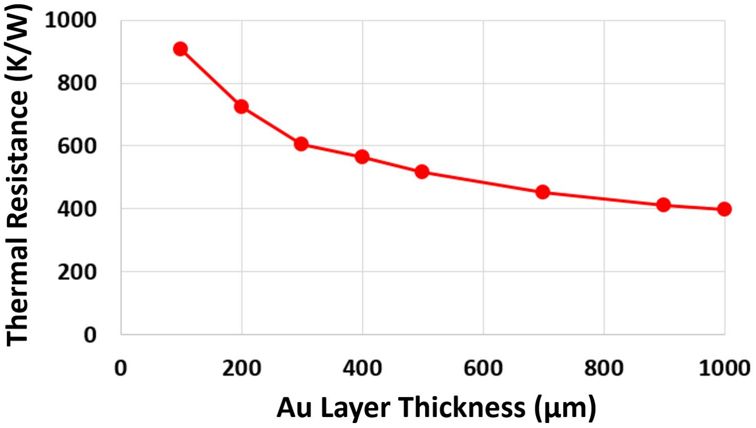

Figure 3.16: Thermal resistance vs thickness of Au layer on the aerogel substrate.

Finally, although the PI aerogel substrate was not machined in this study for a simpler fabrication process, the aerogel substrate can be patterned to the size of the bonding pads to eliminate heat spread along the length of the substrate, as shown in Figure 3.17. A dry-etching was conducted on PI aerogel in a plasma etching tool (ICP RIE by Oxford Instruments) and etched surface of the PI aerogel was measured using a profilometer (Dektak XT Surface Profilometer by Bruker Corporation). Test setup and results are shown in Figure 3.18 where the left half of the surface is covered by Kapton tape for a reference surface to which the uncovered surface is compared after being etched. As a result, it was found that the etching rates of PI aerogel are 1 $\mu m/min$ and 2 $\mu m/min$ at etching powers of 100W and 200 W, respectively.

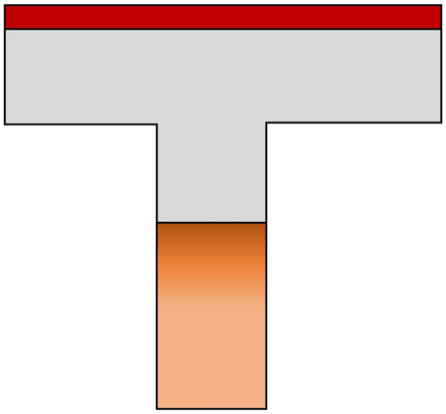

Figure 3.17: Patterned aerogel to minimize heat spread along the length of the substrate.

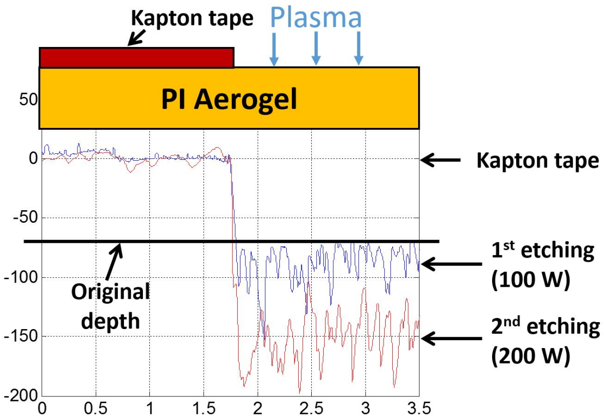

Figure 3.18: Surface profile of the PI aerogel using Dektak XT Surface Profilometer at etching powers of 100 W and 200 W.

3.2.3 Thermal Resistance Analysis of Electrical Connections

Significant heat loss can also occur through electrical connections that are established to operate the MEMS inertial sensors, and this loss may become significant. Therefore, in order to minimize heat loss, the thermal resistance of electrical connections will need to be analyzed. The thermal resistance of the electrical connections can be calculated as:

$$R_{ec} = \frac{1}{n_{wire}} \cdot \frac{l_{wire}}{k_{wire}A_{wire}} \tag{3.4}$$

where n_{wire} is the number of electrical wires, l_{wire} is length of wires, k_{wire} is thermal conductivity of wires, and A_{wire} is cross-section area of wires. In this equation, the length of all wires is assumed to be the same. According to Equation 3.4, thermal resistance is proportional to the length of wires, and inversely proportional to the number, thermal conductivity, and cross-section area of wires. Among these variables, the length of wires is generally predetermined by the size difference between the package and the MEMS inertial sensors, and by the required number of electrical connections for operation of the MEMS inertial sensors, heater, and RTD. Therefore, in order to increase the thermal resistance, the thermal conductivity and cross-section area of wires need to be decreased. As a result, the electrical connections are established by using 0.5-mil platinum bonding wires that have a thermal conductivity of 72 W/m·K. When compared with a 1-mil aluminum bonding wire, which is one of the most typical bonding wires, these wires are half as thick and a third as thermally conductive as the aluminum bonding wires.

As an alternative method for electrical connections, a ribbon cable made of parylene and thin-film metal layers can also be used to minimize heat loss through electrical connections [74]. For simpler fabrication and assembly processes, however, a 0.5-mil platinum bonding wire was used in this study.

3.2.4 Total Thermal Resistance Through Solid Conduction

Using Equation 3.3 and 3.4, the total thermal resistance due to heat loss through solid conduction can be calculated as:

$$R_{tot} = R_{ag} \parallel R_{ec} = \frac{R_{ag} \cdot R_{ec}}{R_{ag} + R_{ec}} = \frac{t_{ag} l_{wire}}{t_{ag} n_{wire} k_{wire} \pi (\frac{d_{wire}}{2})^2 + l_{wire} n_{pad} k_{ag} w_{eff}^2} \tag{3.5}$$

Based on this equation, the total thermal resistance due to heat loss through solid conduction is calculated for an example where the thickness (t_{ag}) and thermal conductivity (k_{ag}) of the aerogel substrate are 125 μm and 0.03 W/m·K, and the length (l_{wire}), number (n_{wire}), thermal conductivity (k_{wire}), and diameter (d_{wire}) of the bonding wires are 5 mm, 18, 72 W/m·K, and 19 μm, respectively. Furthermore, the number of bonding pads (n_{pad}) is four, the shape of the bonding pads are assumed to be a square, and no metal layer is deposited on the aerogel substrate. The result is shown in Figure 3.19 where the total thermal resistance is plotted as the width of each of the bonding pads changes from 100 to 1000 μm. Furthermore, in order to understand the effect of the bonding wires on the total thermal resistance, the thermal resistance of the aerogel substrate alone (i.e., without electrical connection), which was calculated in previous sections, was also plotted on the same graph. From the simulation results, it was found that as the width of the bonding pads increases, the total thermal resistance decreases in a quadratic manner. Moreover, when the width of the bonding pads is small, the electrical connections affect the total thermal resistance significantly, while their effect on the total thermal resistance gradually decreases as the width increases.

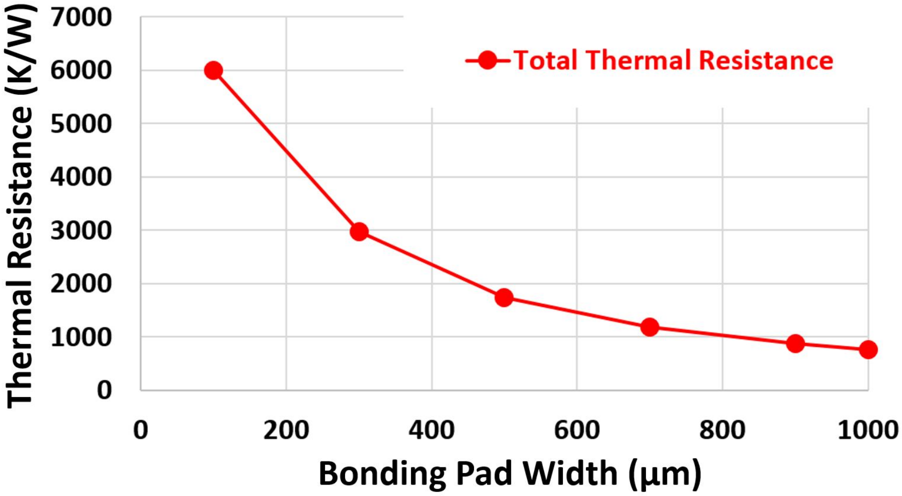

Figure 3.19: Thermal resistance with and without 18 electrical connections over the width of each of the bonding pads.

Similarly, another simulation was conducted where the width of the bonding pads is fixed at 100 μm, and other simulation conditions are the same as those in the previous simulation except the number of electrical connection wires was changed from 0 to 40. The width of the bonding pads was then increased to 900 μm by an increment of 200 μm to repeat the same simulation at each width. From the simulation results, it was found that as the width of the bonding pads increases, the total thermal resistance becomes less dependent on the number of electrical connection wires because, from a certain width, heat loss through the aerogel substrate becomes comparable to heat loss through the electrical connections. Therefore, a desired thermal resistance value should be obtained by adjusting the width of the bonding pads according to the number of bonding wires that are required for the operation of the MEMS inertial sensors.

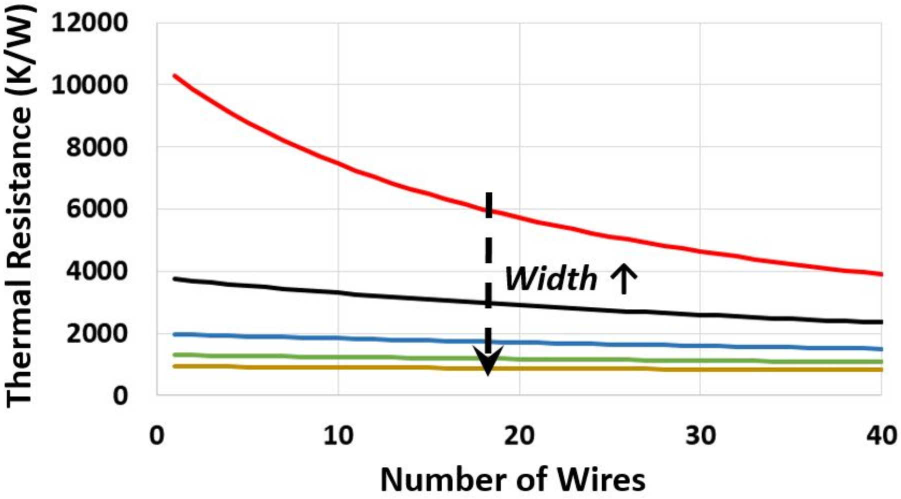

Figure 3.20: The total thermal resistance over the number of electrical connection wires at various widths of the bonding pads.

3.3 Fabrication and Assembly of the DOCIS

One of the main advantages of the proposed DOCIS is that the fabrication and assembly processes are straightforward and simple. Figure 3.21 shows the fabrication process flow for the silicon mechanical isolation stage in the DOCIS, and Figure 3.22 shows the assembly process flow for the DOCIS. In order to fabricate the silicon mechanical isolation stage, a 500 μm-thick silicon wafer is prepared and a 0.5 μm oxide layer (SiO_2) is deposited on the wafer using an evaporator (EvoVac evaporator by Angstrom Engineering Inc.) to prevent a short circuit between metal lines that will be deposited in later steps (Figure 3.21 (a)). The wafer is then spin-coated using SPR 220 3.0 at 3 krpm, and developed for 7 seconds using a mask plate and photolithography (MA/BA 6 by SUSS MicroTec SE). After that, a Ti/Au (100/3000 Å) layer is deposited on the wafer using an evaporator (Enerjet Evaporator by Denton Vacuum Inc.), and patterned using the ultrasonic lift-off process in PRS-2000 at 80 °C for 20 minutes to form a heater and other electrical connections on the wafer (Figure 3.21 (b)). The wafer is then again spin-coated using SPR 220 3.0 at 3 krpm, and developed for 7 seconds using a mask plate and photolithography (MA/BA 6 by SUSS MicroTec SE), on which a Ti/Pt (200/1000 Å) layer is deposited using an evaporator (Enerjet Evaporator by Denton Vacuum Inc.) and patterned using the ultrasonic lift-off process in PRS-2000 at 80 °C for 20 minutes to form an RTD (Figure 3.21 (c)). After deposition and patterning processes are completed, the wafer is turned upside down, spin-coated using SPR 220 3.0 at 1 krpm, developed for 13 seconds using a mask plate and photolithography (MA/BA 6 by SUSS MicroTec SE), soft-baked at 115 °C for 120 seconds, and mounted on a blank wafer. After being mounted on the blank wafer, the bottom surface of the silicon wafer is dry-etched using a DRIE tool (Pegasus 4 by SPTS Technologies Ltd.) to form bonding pads (Figure 3.21 (d)). From a set of trials, it was found that the etch rate is 3.45 μm/min using LNF Recipe 1 at 20 °C, and thus in order to form 100 μm-deep square bonding pads, the wafer can be etched for 29 minutes or so. In the next step, suspension springs, or crab-legs, are formed on the silicon wafer by detaching the blank wafer from the silicon wafer in DI water, flipping the wafer back, spin-coating SPR 220 3.0 at 875 rpm on the wafer, developing SPR for 30 seconds using a mask plate and photolithography (MA/BA 6 by SUSS MicroTec SE), and mounting the silicon wafer on the blank silicon wafer for dry-etching processes. After that, the SiO_2 layer, which was deposited on the silicon wafer in step (a), is dry-etched first using a glass etcher (LAM 9400 SE) to expose the area for spring patterns on the silicon wafer, and then the exposed area on the silicon wafer is dry-etched using a DRIE tool (Pegasus 4 by

SPTS Technologies Ltd.) (Figure 3.21 (e)). After the etching process is completed, the wafer is detached from the blank wafer by soaking it in DI water for 1 hour and gently sliding the wafer off. Finally, the wafer is diced using a dicing tool (ADT 7100 Dicing Saw).

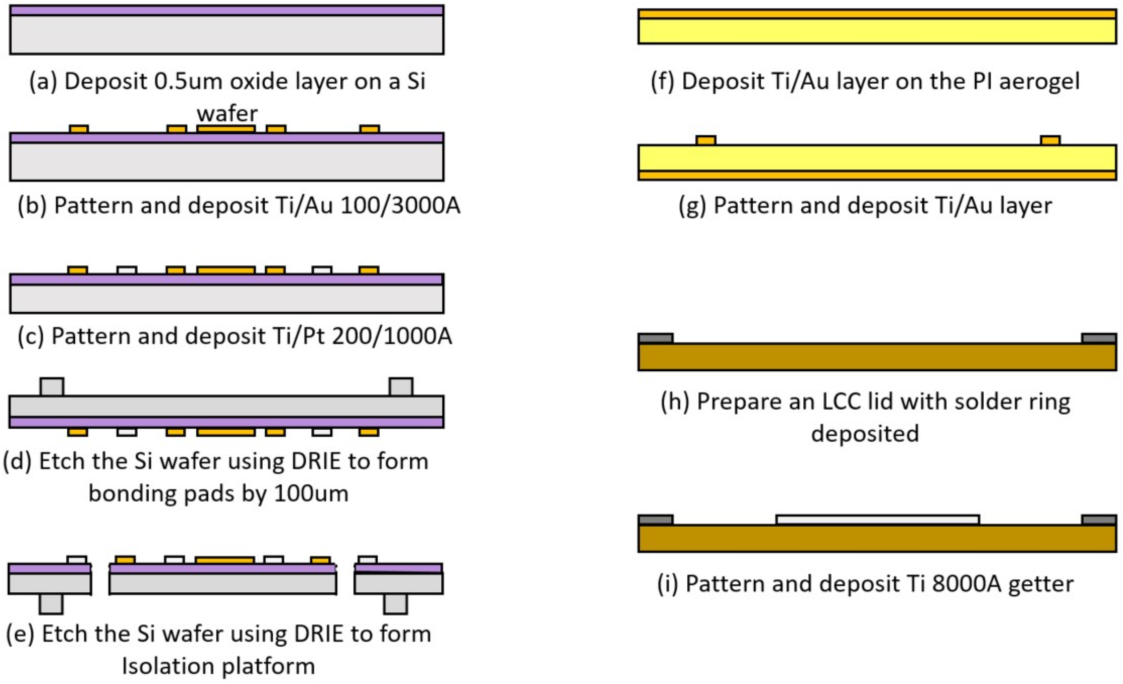

(a) Deposit 0.5um oxide layer on a Si wafer

(b) Pattern and deposit Ti/Au 100/3000A

(c) Pattern and deposit Ti/Pt 200/1000A

(d) Etch the Si wafer using DRIE to form bonding pads by 100um

(e) Etch the Si wafer using DRIE to form Isolation platform

(f) Deposit Ti/Au layer on the PI aerogel

(g) Pattern and deposit Ti/Au layer

(h) Prepare an LCC lid with solder ring deposited

(i) Pattern and deposit Ti 8000A getter

Figure 3.21: The fabrication flow of a silicon mechanical isolation stage in the DOCIS.

After the fabrication of the silicon mechanical isolation stage is completed, a metal layer of Ti/Au (200/3000 Å) is deposited on the bottom surface of the PI aerogel using an evaporator (Enerjet Evaporator by Denton Vacuum Inc.) for eutectic bonding onto a 44-pin LCC package (LCC04438 by Spectrum Semiconductor Materials Inc.). The intermediate layer used for eutectic bonding is Au-Sn preform (Au 80 % – Sn 20 %) (Figure 3.21 (f)). The PI aerogel is then flipped back to deposit a patterned Ti/Au (200/3000 Å) layer on the top surface using a silicon shadow mask and an evaporator (Enerjet Evaporator by Denton Vacuum Inc.) (Figure 3.21 (g)). The pattern of the metal layer is made the same as the pattern of the bonding pads so that the silicon isolation stage is aligned well to the center of the aerogel substrate. Also, a combo lid for the LCC package (CL-62010 by Spectrum Semiconductor Materials, Inc.), on which an Au-Sn solder ring is welded along the perimeter of the lid, is prepared for vacuum-sealing the LCC package in a later step (h). A thin-film getter, a Ti (8000 Å) layer, is then deposited in the center of the lid (i).

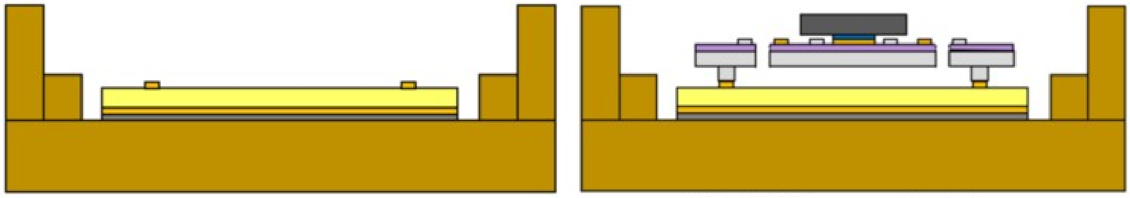

(j) Attach the aerogel onto an LCC package using Au-Sn preform

(l) Attach MEMS sensors on the platform using adhesive

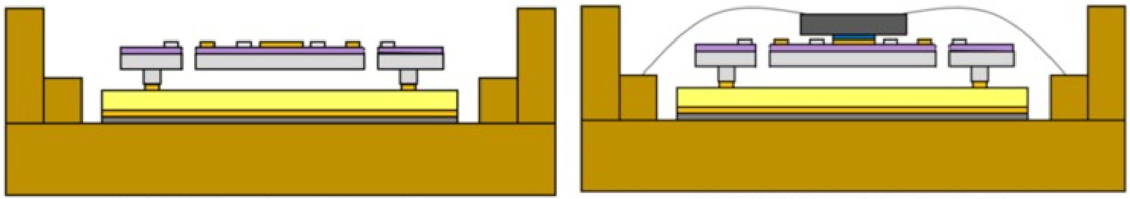

(k) Attach the isolation platform on the aerogel using adhesive

(m) Wire-bonding using Pt bonding wire

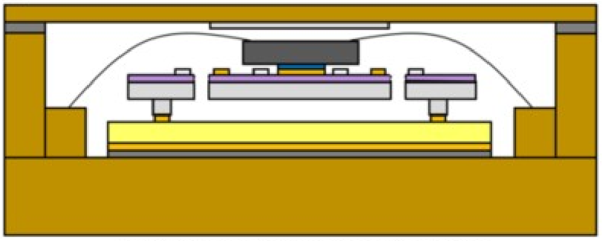

(n) Vacuum-seal the package using Au-Sn preform and Ti getter

Figure 3.22: The assembly flow of the DOCIS.

The fabrication processes are then followed by the assembly process, which is shown in Figure 3.22. The aerogel substrate is first attached to the LCC package using the Au-Sn preform and a wafer bonder (EVG 520IS by EVGroup) (j). In this step, if the solder preform overflows, the solder may climb up along the sidewall of the aerogel, which would then reduce the thermal resistance of the aerogel substrate significantly. In order to prevent the solder preform from overflowing, therefore, a small piece of a solder preform needs to be used. In this specific example where the dimension of the aerogel substrate is 10 mm x 10 mm, it was found from a set of trials that the solder preform having a dimension of 8 mm x 8mm does not overflow. After the aerogel substrate is attached on the LCC package, the bonding pads of the silicon isolation stage are attached to the aerogel substrate by using silver epoxy (ABLEBOND 84-1 LMI by Henkel) (k). This adhesive is used for its low out-gassing, low curing temperature (150 °C), and short curing time (1 hour). A MEMS IMU, Invensense MPU-6050, is then attached to the silicon isolation stage using the silver epoxy (l), and electrical connections are established by using 0.5-mil platinum bonding wires and a wedge wire bonder (4523D, Kulicke & Soffa) (m). In this step, since platinum is a hard material, the electrical connections using the Pt bonding wires cannot be made at room temperature. Instead, the wire-bonding process needs to be conducted at 100 °C or above. Finally, the package is outgassed for 2 hours, the TI getter is activated, and the LCC package is vacuum-sealed using a wafer bonder (EVG 520IS by EVGroup). During the outgassing process, the LCC package and the lid are exposed to a condition where the package temperature is 250 °C and surrounding pressure level is 100 μTorr for 2 hours. In the getter activation and vacuum-sealing processes, the LCC package and the lid are then exposed to a condition where the package temperature is 340 °C and the surrounding pressure level is 10 μTorr for 20 minutes. After the vacuum-sealing process is completed, the temperature and the pressure are decreased to the default temperature of the wafer bonder (i.e., 50 °C) and atmospheric pressure, respectively. Temperature profile for the getter activation and vacuum-sealing processes is shown in Figure **??**.

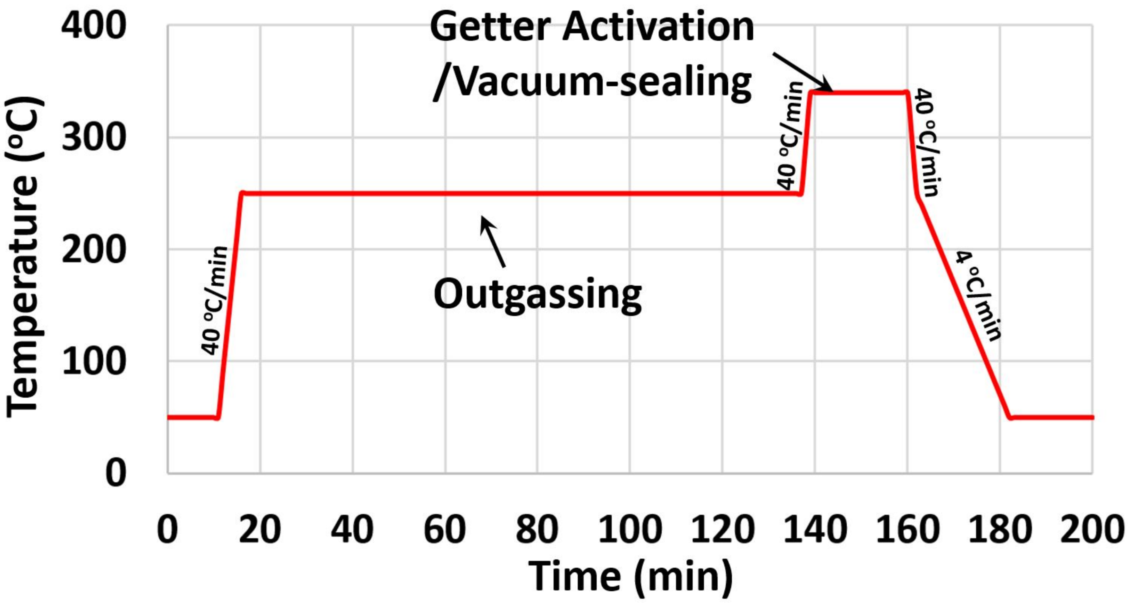

Figure 3.23: Temperature profile for the getter activation and vacuum-sealing processes for the DOCIS.

3.4 Simulation and Experiment Results of the DOCIS

Figure 3.24 and Figure 3.25 show the geometries of the silicon isolation stage and the assembled DOCIS in the COMSOL simulation tool, respectively. The geometry of the silicon isolation stage was used to compute the resonant frequency of the mechanical isolation stage, and the geometry of the assembled DOCIS to compute the total thermal resistance of the DOCIS. The size of the silicon isolation stage is 6000 μm x 6000 μm x 500 μm (W x L x H) and the number, the width, and the height of bonding pads are four, 600 μm, and 100 μm, respectively. The cavity size of the 44-pin LCC package where the thermal and mechanical isolation stages are attached is 12 mm x 12 mm (W x L) and the size of the thermal isolation stage is 10 mm x 10 mm x 0.125 mm (W x L x H). According to the simulation result, the first mode (up-down motion) of the resonant frequency of the mechanical isolation stage was found to be around 1.9 kHz, while the second and third modes (tilting modes in pitch and roll axes) are both around 3.2 kHz (Figure 3.26). Furthermore, the thermal resistances at different pressure levels are shown in Figure 3.27, from which it was found that the thermal resistance reaches a plateau around 1,700 K/W at 1m Torr.

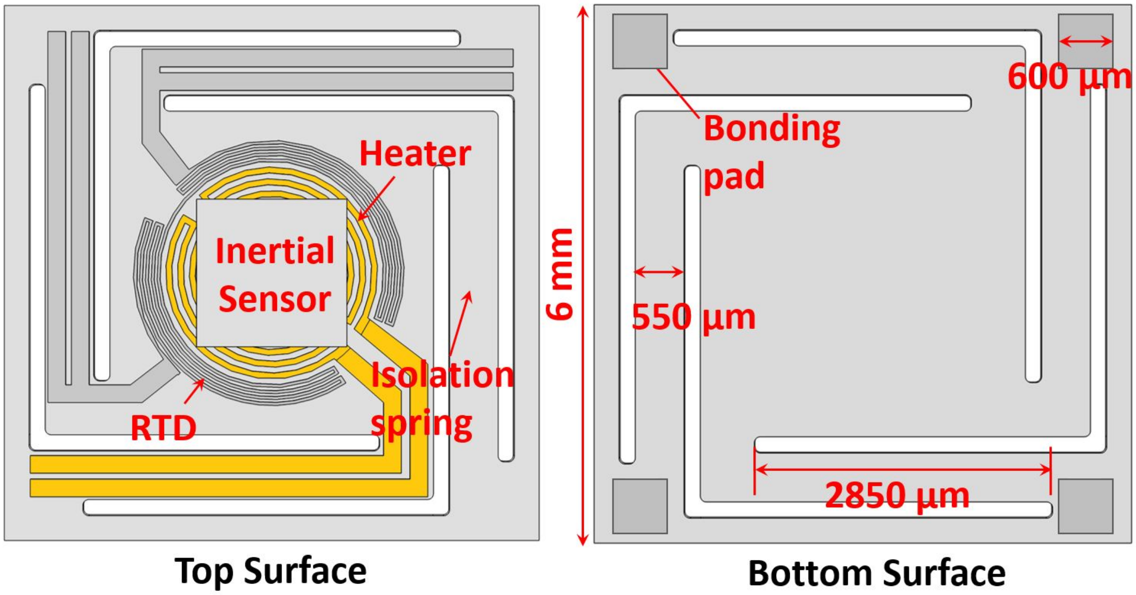

Figure 3.24: Geometry of the mechanical isolation stage.

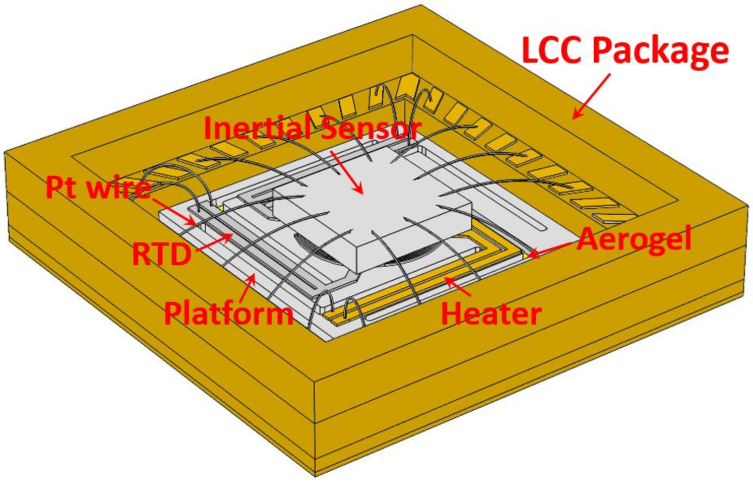

Figure 3.25: Geometry of the DOCIS.

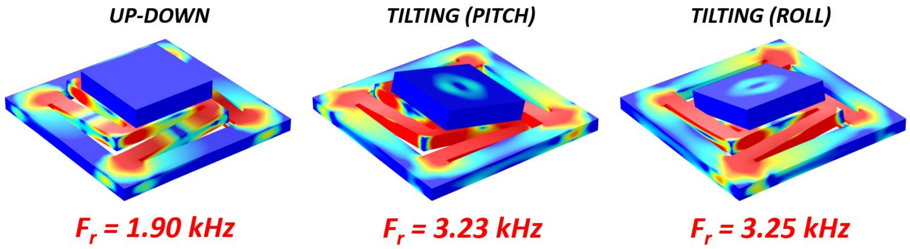

Figure 3.26: Resonant frequency of the isolation platform: simulation results.

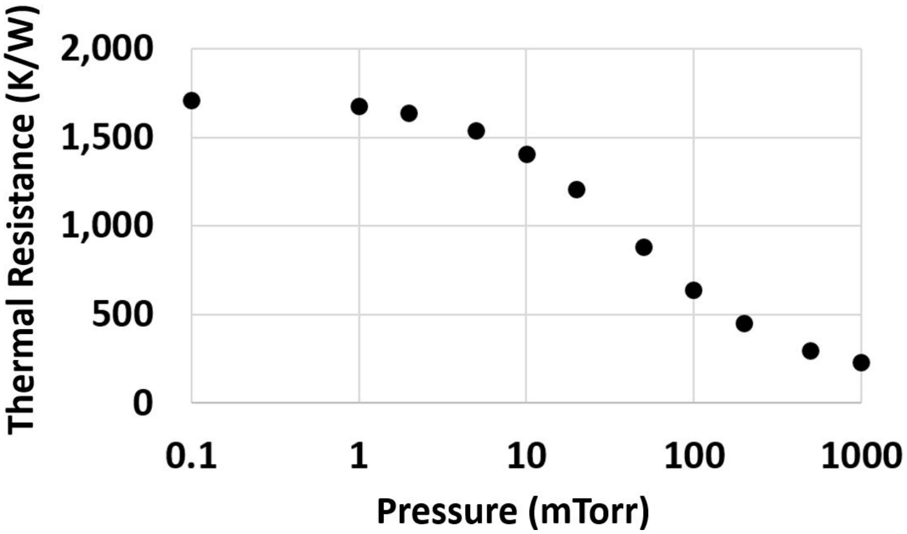

Figure 3.27: Simulation: thermal resistances of the DOCIS over pressure.

Next, Figure 3.28 shows the assembled DOCIS before it was vacuum-sealed. The assembled DOCIS was placed in a vacuum probe station (FWP6 by Lake Shore Cryotonics, Inc.) to measure the thermal resistance of the DOCIS at different pressure levels. At atmospheric pressure, the thermal resistance was very low, and as the pressure went down, the thermal resistance was increased exponentially until it reached a plateau around 1,700 K/W at 1 mTorr. Finally, the measurements were compared with the simulations, as shown in Figure 3.29, and it was found that the simulation results match the experimental results well.

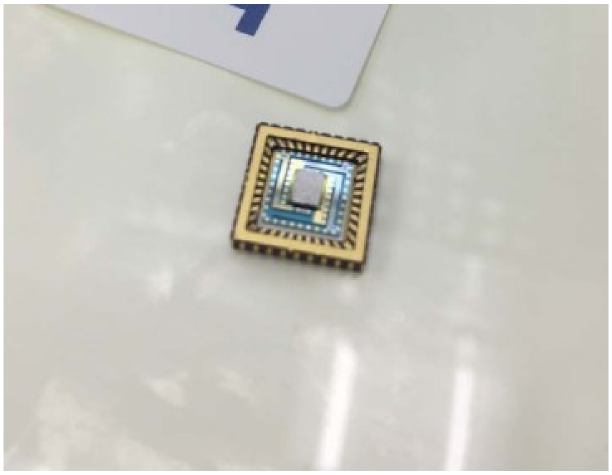

Figure 3.28: Assembled DOCIS.

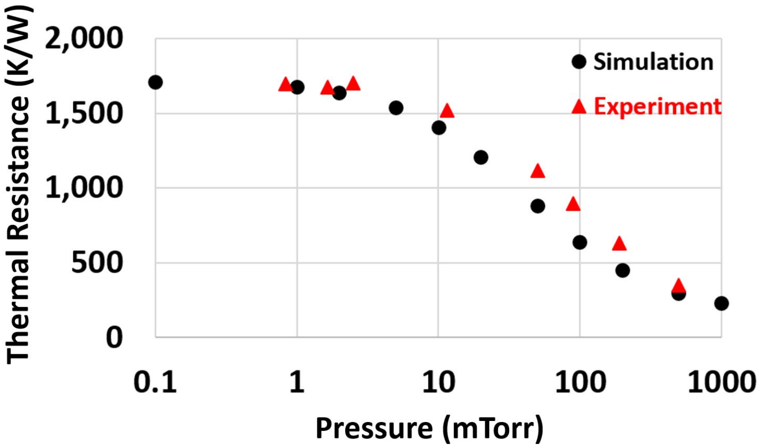

Figure 3.29: Simulated and Measured thermal resistances of the DOCIS over pressure.

3.5 Summary and Remaining Problems of the DOCIS

In this chapter, as a method to address the issues that the SOCIS has, such as high-temperature difference across the isolation stage and limited design flexibility of the isolation stage, the double isolation stage oven-controlled system (DOCIS) was proposed. In the proposed DOCIS design, the mechanical isolation stage was made of silicon, rather than glass in the SOCIS, to provide a small temperature difference across the isolation stage, while a thermal isolation stage made of aerogel was added to provide a good thermal isolation capability. As a result, the addition of the thermal isolation stage in the system was able to allow the mechanical isolation stage to be more flexible. Furthermore, in order to confirm its good thermal and mechanical isolation capabilities, including temperature, vibration, and stress, simulations and experiments were conducted.

First, the thermal resistance of the DOCIS was estimated by conducting thermal resistance analyses of two main heat loss paths, the aerogel substrate, and the electrical connections. In the thermal resistance through the aerogel substrate, the contact area of the bonding pads with the aerogel substrate, the thermal conductivity of aerogel, and the thickness of a metal layer that may be deposited on the aerogel substrate for eutectic bonding were critical variables that determine the effective contact area of the bonding pads with the aerogel substrate. Based on the effective contact area, the thermal resistance due to heat loss through the aerogel substrate could be calculated and compared with the thermal resistance computed by using a COMSOL FEM simulation tool. Next, as heat loss through electrical connections were found to be non-negligible, the thermal resistance due to the heat loss through electrical connections was also analyzed where it was found that a thinner and longer wires made of a material that has a lower thermal conductivity should be used to minimize the heat loss. As a result, 0.5-mil platinum wires were used to replace 1-mil aluminum wires, which is the most widely used bonding wire. The total thermal resistance was then calculated and verified through a set of experiments that experimental results match the calculation results. After the thermal resistance analyses were completed, an analysis for the vibration isolation capability was conducted by using the COMSOL FEM simulation tool. The simulation result showed that the resonant frequency of the mechanical isolation stage is around 3.1 kHz, which is well above the bandwidth of the inertial sensors and thus will not interfere with the measurement of the inertial sensors. Therefore, it is expected that the isolation stage would filter any unwanted vibration whose frequency is slight over 3.1 kHz along Z-axis (i.e., up-down motion). Furthermore, the temperature-induced stress effect on the inertial sensors was analyzed through simulations and it was verified that the stress effect would be much less than that of the SOCIS. Finally, detailed fabrication and assembly process flows of the DOCIS were introduced.

The proposed DOCIS, however, has a few remaining problems that need to be addressed in the future. One problem is reduced bonding strength between the aerogel substrate and the silicon mechanical isolation stage. As the bonding area between the aerogel and the silicon stage was significantly reduced by forming bonding pads at the bottom surface of the silicon stage, the bonding strength is expected to be reduced proportionally, which would then reduce the system reliability. For the silver epoxy that was used in this study (ABLEBOND 84-1LMI by Loctite), the unit die shear strength is 4.75 $kg \cdot f/mm^2$ when it was used to bond a silicon die to an Ag/Cu lead frame substrate [75]. Also, according to [76], since silver adhesives show a consistent unit die shear strength in MPa, it is valid to assume that the shear strength will be linearly proportional to the contact area. Therefore, the total shear strength of the bonding pads of the DOCIS can be calculated as:

$$F_{sh} = \tau \cdot A = 4.75kg \cdot f/mm^2 \cdot 1.44m^2 = 6.84kg \cdot f = 67N. \tag{3.6}$$

where F_{sh} is the total shear strength of the bonding pads, τ is the unit shear strength, and A is the bonding area. A more detailed study on the bonding strength will be discussed in the next chapter.

For future works, the simulation results on the vibration isolation and temperature-induced stress isolation capabilities need to be verified through experiments. In the verification process for the temperature-induced stress isolation capability, it is recommended to eliminate the plastic package (i.e., EMC) that covers IMUs, because the plastic package could add unexpected stress, which cannot be distinguished from the temperature-induced stress caused by temperature differences across the isolation stage.

CHAPTER IV

Oven-Controlled Birdbath Shell Resonator

In this chapter, the double isolation stage oven-controlled inertial sensor (DOCIS) for the birdbath (BB) shell resonator, which is one of the best performing MEMS gyroscopes, will be designed. However, prior to designing the DOCIS, non-ideal properties of the birdbath shell resonator, including inconsistent performance during and after vacuum-sealing process, temperature effect, stress effect, high-g shock impact, and bias voltage effect on performance of the resonator, will be discussed first to understand the properties that the BB shell resonator is susceptible. Then, simulations of the oven-controlled BB shell resonator will be conducted to prove that the proposed DOCIS for the BB shell resonator can mitigate the non-ideal properties that would otherwise degrade the performance of the resonator significantly.

4.1 Non-Ideal Properties of the Birdbath Shell Resonator

4.1.1 Inconsistent Performance During and After Vacuum-Sealing Process

The vacuum-sealing process is a critical step for the BB shell resonator, since the quality factor of the shell resonator, which is a direct measure of the performance, depends heavily on the pressure level around the resonator. In other words, the quality factor of the shell resonator degrades significantly as the pressure level around the resonator becomes higher due to fluidic interaction with the resonator [77].

Figure 4.1 shows the overall packaging process for the shell resonator, in which the vacuum-sealing process occurs in the last step. Step#1 through Step#4 prior to the vacuum-sealing process in Step#5 are included in the packaging process to 1) establish an electrical sensing for the displacement of the outer rim of the shell resonator, 2) reduce the stress that is introduced in the electrode-coating process in Step#1 and the die-attachment process in Step#3, and 3) eliminate potential outgassing contaminants inside the package. Furthermore, in order to understand the effect of each step on the performance, the ring-down time, which is directly proportional to the quality factor, was measured after each process step is completed. The ring-down times in this study are measured at the frequencies of the wine-glass modes (i.e., n=2 mode) [77].

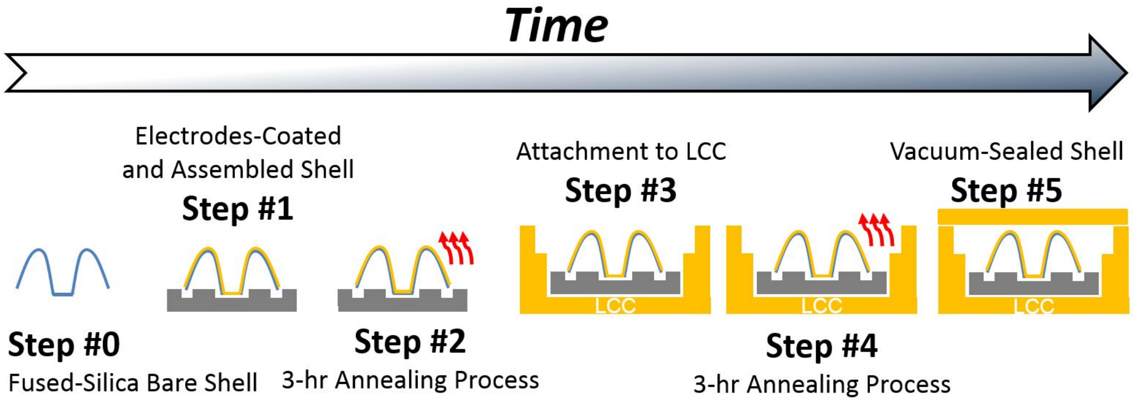

Figure 4.1: Vacuum-Sealing Process Flow.

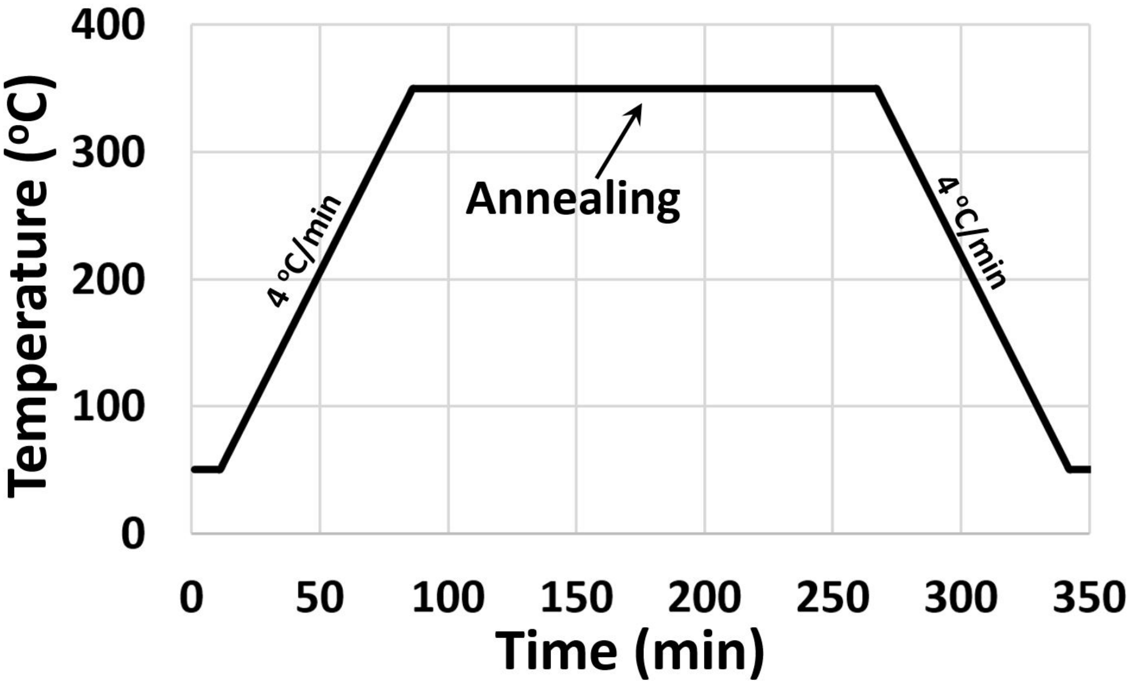

Figure 4.2: Temperature profile for the 3-hr annealing process.

In Step #0, a fused silica shell resonator is prepared in a blow torch station as in [30]. Because the resonator is made of an electrically insulating material, fused silica, a metal layer should be deposited on the resonator to convert the physical displacement of the rim of the shell resonator to the electrical signal. Therefore, a Ti/Au (100/500 Å) metal layer is sputtered on the top surface of the resonator using a sputter deposition tool (Lab 18-2 by Kurt J. Lesker Company) (Step #1) [30]. In order to measure the ring-down time of the shell resonator after electrode-coating, the shell resonator is temporarily attached on a silicon substrate using a crystal bond adhesive (Crystalbond 509 by Structure Probe, Inc.), and the attached shell resonator is then placed in a laser Doppler vibrometer (LDV) test setup (LDV system by Polytec, Inc.), as shown in Figure 4.3, where the attached shell resonator is actuated at the resonant frequencies in the wine-glass mode by a piezo actuator and the displacement of the rim of the shell, is measured by a laser from the microscope lens. After the measurement is completed, the shell resonator is detached from the silicon substrate at an elevated temperature using a hot air solder blower, and permanently attached on an electrode substrate. The electrode substrate is made from a silicon-on-insulator (SOI) wafer, and the silicon in the substrate has extremely low electrical resistance to form a conductive plate of a capacitor with the other plate being the rim of the electrode-coated shell resonator, through which the displacement of the shell resonator can be detected [30]. The permanently attached, or assembled, shell resonator is then annealed at 350 °C for 3 hours using 5% H_2 forming gas at 200 Torr (Step #2), and the temperature is ramped up and down at the rate of 4 °C/min (Figure 4.2). In order to measure the ring-down time after the annealing process in Step #2, the assembled shell resonator is placed in a vacuum probe station (FWP6 by Lake Shore Cryotronics, Inc.), as shown in Figure 4.6. In Step #3, in order to die-attach the assembled shell resonator on an LCC package (LCC04438 by Spectrum Semiconductor Materials, Inc.), Ti/Pt/Au (100/300/3000 Å) metal layers are deposited on the bottom glass surface of the electrode substrate. The metal layer is deposited on a small area in the center of the electrode substrate by using a shadow mask to minimize potential mounting stress on the shell resonator [38]. Then an Au-Sn preform (Au 80 % – Sn 20 %) is prepared and placed between the LCC package and the assembled shell resonator for eutectic bonding (Figure 4.4(a)). The temperature of the package is then raised up to 340 °C at the rate of 40 °C/min, the pressure around the package is decreased to 100 μTorr. The temperature and pressure conditions are maintained for 20 minutes to melt the Au-Sn preform and dropped back to initial temperature and pressure values of 50 °C and atmospheric pressure, respectively. The attached shell resonator is then wire-bonded using 1-mil aluminum wires and a wedge bonding tool (4523D by Kulicke and Soffa Industries, Inc.) (Figure 4.4(b)). After the wire-bonding process is completed, the ring-down time of the shell resonator is measured in the vacuum probe station again, and another annealing process is conducted at 350 °C for 3 hours using 5% H_2 forming gas at 200 Torr where the temperature is ramped up and down at the rate of 4 °C/min (Step#4). Right after the annealing process, the ring-down time of the shell resonator is measured at various pressure levels in the vacuum probe station to estimate the pressure level inside the package after the package is vacuum-sealed in the following step. A few examples of the ring-down time over pressure are shown in Figure 4.7. During the measurements in this step, the magnitude of the signal at sensing electrodes needs to be maintained at nearly the same value at different pressure levels by adjusting the magnitude of the input signal at driving electrodes for reasonable comparisons of the ring-down times at different pressure levels. Furthermore, the temperature during the measurements needs to be maintained at a constant value to minimize the temperature effect. From the results in Figure 4.7, it was found that the ring-down time is heavily dependent on the pressure level at 0.2 mTorr or higher, and slowly reaches a plateau at the pressure level below 0.2 mTorr.

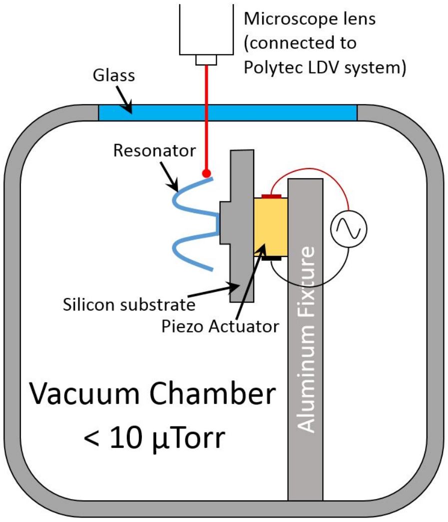

Figure 4.3: Ring-down time measurement using LDV station.

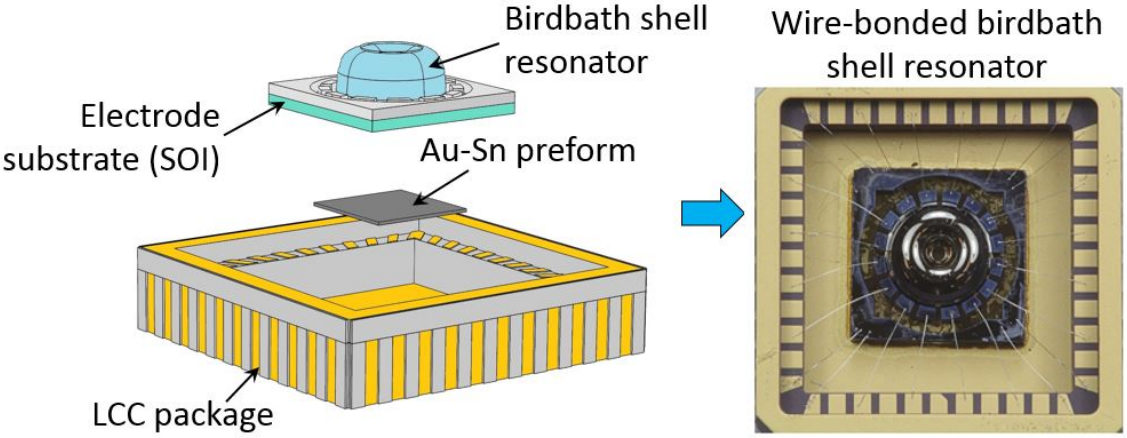

Figure 4.4: (a) shell resonator is attached to LCC package and (b) the resonator is wire-bodned to the LCC package pads.

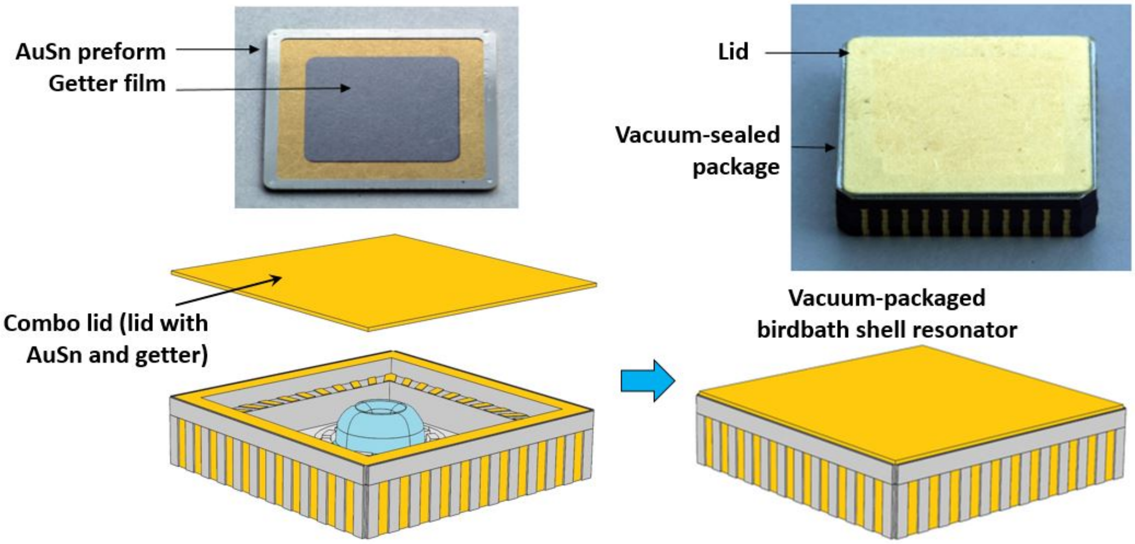

Figure 4.5: Vacuum-sealing process.

Finally, in Step#5, the LCC package is vacuum-sealed using a combo lid (CL-62010 by Spectrum Semiconductor Materials, Inc.) on which a thin Au-Sn (Au 80 % – Sn 20 %) preform is welded along the perimeter, as shown in Figure 4.5. Furthermore, to obtain low pressure in the package, a thin-film getter (Ti, 8000 Å) is deposited on the center of the combo lid [78]. In order to activate the getter and melt the Au-Sn preform on the lid for sealing, the package is placed in a wafer bonder tool (EVG 520IS, EV Group), and the sealing condition is programmed as follows: the temperature and pressure are first ramped up to 250 °C at the rate of 40 °C/min and ramped down to 0.1 mTorr, respectively, and the same temperature and pressure are maintained for 2 hours for outgassing inside the package. Then, the temperature and pressure are ramped up to 340 °C at the rate of 40 °C/min and ramped down to 0.01 mTorr, respectively, and the same temperature and pressure are maintained for 20 minutes for getter activation and vacuum-sealing processes. Finally, the temperature is cooled down to 250 °C at the rate of 40 °C/min, and then at the rate of 4 °C/min thereafter until the temperature reaches 50 °C, while the pressure goes back up to atmospheric pressure. The temperature profile for the vacuum-sealing process is shown in Figure 4.8.

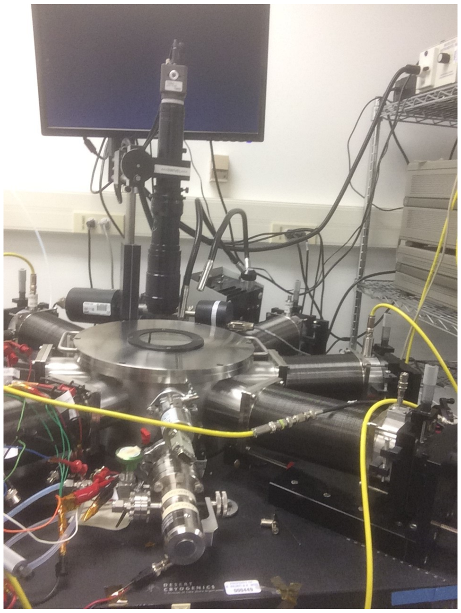

Figure 4.6: Test setup for ring-down time measurement at different pressure levels.

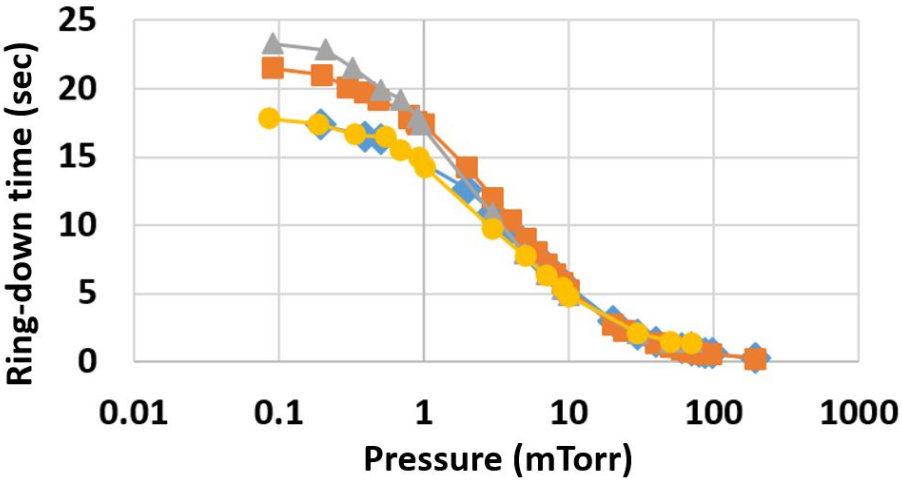

Figure 4.7: Ring-down time of assembled shell resonators measured in LakeShore probe station before the vacuum-sealing process.

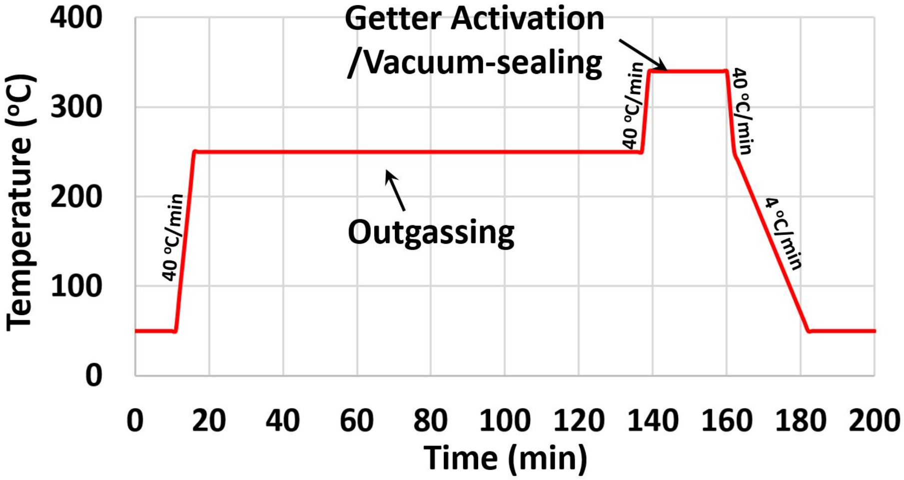

Figure 4.8: Temperature profile for vacuum-sealing process.

After the vacuum-sealing process is completed, the ring-down time of the vacuum-sealed package is measured to estimate the vacuum level inside the sealed package. If the estimated vacuum level is much higher than expected, or the ring-down time is much lower than expected, the ring-down time of the vacuum-sealed package is measured again in the vacuum probe station to check if the package is leaking.

In the first batch, a total of five shell resonators were vacuum-sealed, among which four shell resonators were found either having a pressure inside the LCC package around 1 ATM or leaking. As mentioned earlier, 8000 ÅTi getter was deposited on combo lids to obtain low pressure inside the package using a vacuum evaporator (Enerjet Evaporator). For the getter deposition, a silicon shadow mask was utilized to protect the Au-Sn solder preform layer on the combo lid from the getter material. Since this shadow mask was fabricated to be capable of depositing getter on multiple lids, the Ti getter was deposited on multiple lids simultaneously to reduce the fabrication cost. Consequently, some combo lids were used immediately after the getter was deposited, while the other lids were not used until later and stored in the cleanroom for several days before having been used for the vacuum-sealing process. We suspected that this might have caused the getter film to be corrupted due to the high reactivity of Ti, and thus the vacuum-level inside the LCC package in Batch #1 was high. In later batches, therefore, the vacuum-sealing process was carried out by using the lids on which an 8000 ÅTi getter was deposited immediately before the sealing process. As a result, later batches, Batch #2 and #3, showed 3.9 times higher yield than Batch #1 (i.e., from 20 % to 78 %, Figure 4.9), in which the pressure levels inside the packages were estimated to be lower than 0.1 mTorr. This indicates that the corrupted Ti getter was indeed the cause for the low yield in Batch #1.

Moreover, two unsuccessfully vacuum-sealed packages from each of the last two batches were also examined. The packaged resonator from Batch #2 had a descent ring-down time immediately after vacuum-sealed, but eventually, the ring-down time went down to less than 1 second. We suspect contaminant was left in the package that it outgassed after the package was vacuum-sealed over the course of time. On the other hand, the packaged resonator from Batch #3 was physically damaged during the packaging process due to mishandling.

Ring-down times of total 14 shell resonators throughout three fabrication batches were measured and the measurement results are summarized in Figure 4.9. In Step #0 where no metal layer is deposited on the shell resonator (or ”bare” shell), the ring-down times were measured by using a laser Doppler vibrometer (Polytec LDV system), and the average ring-down time was 46 seconds. After Ti/Pt metal layer was deposited on the shell resonator, a noticeable drop in the ring-down time was observed; the average ring-down time was decreased by a factor of 8.2 (i.e., 5.6 seconds). This large drop might have been caused by stress between the fused silica and the deposited metal layer, and by non-uniformity of the metal layer that may cause large energy loss in the resonator. Since the annealing process is frequently conducted to relieve contact stress between materials, a 3-hr annealing process using 5 % H_2 forming gas was conducted for the shell resonators in Step #2 [79]. As a result, the average ring-down time was improved by a factor of 1.7 (i.e., 9.5 seconds). The average ring-down time was improved again by a factor of 1.5, after the shell resonator was die-attached on LCC packages by using Au-Sn preforms. We think the die-attachment forms stronger anchor for the shell resonators, and thus reduces energy loss from the resonator through the anchor, which then leads to the improvement in the ring-down time. When another 3-hr annealing process was conducted after the die-attachment process, the ring-down time was improved by a factor of 1.1. Finally, after the shell resonators were vacuum-sealed, ring-down times of the shell resonators that were successfully vacuum-sealed were improved by a factor of 2.3, which is a higher factor than the improvements in other steps. This indicates that the average ring-down time of the vacuum-sealed shell resonators is much higher than the average ring-down time that was measured at the pressure level where the ring-down time reached a plateau before the resonators were vacuum-sealed. Therefore, another factor than the pressure level seems to affect the performance of the shell resonator during and after the vacuum-sealing process. Meanwhile, It should be noted that the resonators that have the ring-down time around zero at Step #5 in Figure 4.9 are either leaking or damaged during the vacuum-sealing process.

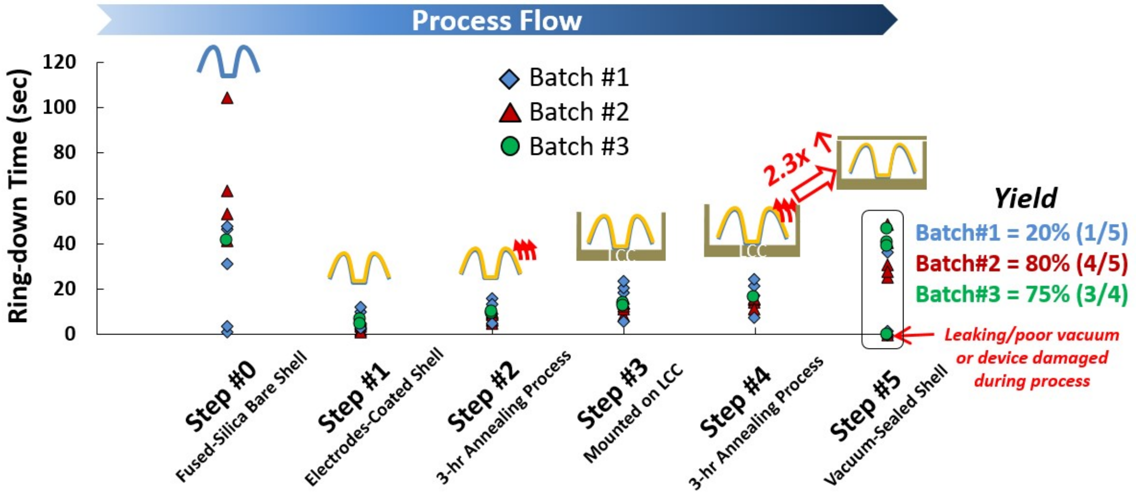

Figure 4.9: Performance variation during the vacuum-sealing process.

In order to understand the reason for the improved performance of the shell resonators after the vacuum-sealing process, the leaking packages were first examined to see if the ring-down times of these packages were also improved after the vacuum-sealing process. They were placed in the vacuum probe station (FWP6, LakeShore) in which the pressure level was reduced to lower than 100 μTorr, and the ring-down times of the resonators were measured. As a result, the measured ring-down times were almost identical to the ring-down times that were measured in Step #4. This indicates that the process condition during the vacuum-sealing, such as temperature and pressure level, is not the factor that improved the ring-down time after the vacuum-sealing process. Therefore, given that the ring-down times of the successfully vacuum-sealed shell resonators were improved after the vacuum-sealing process while those of unsuccessful resonators were not, the improvement is likely due to a factor that can be found in the vacuum-sealed shell resonators only. One possible theory is that a large pressure difference between inside and outside the package may cause stress distribution throughout the shell to change, and thus the ring-down time to change accordingly. However, further investigations should be conducted to understand the reason for the improvement.

After the packaging process and the leaking test were completed, long-term performance monitoring of four selected vacuum-sealed shell resonators was conducted at room temperature, and the results are shown in Figure 4.10. Unit #1 through #4 were monitored for 429 hours (17.9 days), 1850 hours (77.1 days), 1631 hours (68 days), 1593 hours (66.4 days), respectively. From the long-term performance monitoring, it was found that the ring-down time was increasing over time and reached a plateau after 100 hours (4.2 days) to more than 1000 hours (42 days). The continuous increase in the ring-down time after the vacuum-sealing process may be because the pressure inside the vacuum-sealed package decreases over time as the activated thin-film getter during the vacuum-sealing process continues to react with trapped gasses inside the package [27].

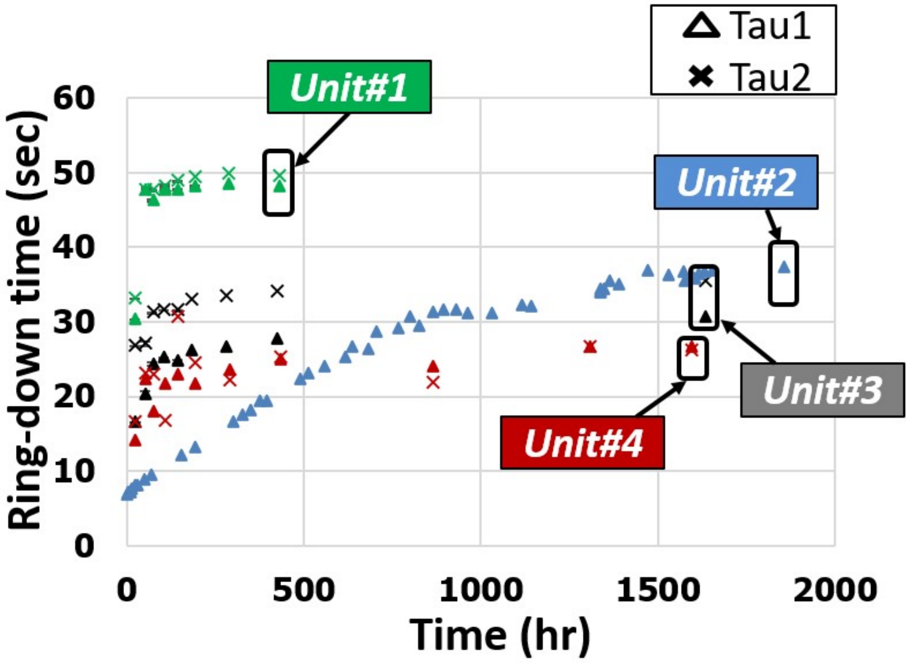

Figure 4.10: Performance monitoring after vacuum-sealing process.

4.1.2 Temperature Effect on BB Shell resonator

It is well known that the resonant frequency of the BB shell resonator, just like other MEMS resonators, changes significantly, when the temperature changes [80]. Temperature effect on the ring-down time of the BB shell resonator, however, has not been reported to date to the best of our knowledge. In this section, therefore, the temperature effect on the ring-down time of the BB shell resonator will be discussed.

In order to conduct an experiment to measure the temperature effect on the ring-down time of the shell resonator in a convection oven chamber, a printed circuit board (PCB) that measures output signals from the vacuum-sealed shell resonator was designed and fabricated, as shown in Figure 4.11, and Figure 4.12. The PCB includes a socket (IC120-0444-306, Yamaichi Electronics) in which a 44-pin vacuum-sealed package can be inserted and replaced by another package. Also, two differential trans-impedance amplifiers (TIA), DA1 and DA2, are designed using operational amplifiers (OPA656, Texas Instruments) to measure the capacitance change at sensing electrodes. In the TIA design, the quadrature signal (S1), which is sensed at the electrode located 90 ° away from the driving electrode (D1), was subtracted from the signal sensed at the sensing electrode (S2), which is located at the opposite side of the driving node (D1), to eliminate feedthrough signal in the signal at the sensing electrode (Figure 4.13). Next, the signal from the TIA is then read by an analog input pin in a microcontroller (Teensy 3.6, SparkFun Electronics) to record the signal and calculate the ring-down time. Furthermore, a constant current source (LM334MX, Texas Instruments) and a heater control circuit (Si4838DY, Vishay Siliconix) are soldered on the PCB to provide a constant current to an RTD and supply an appropriate amount of current to the heater, respectively. Finally, an external temperature sensor (TMP 112, Texas Instrument) is soldered on the PCB to provide surrounding temperature information.

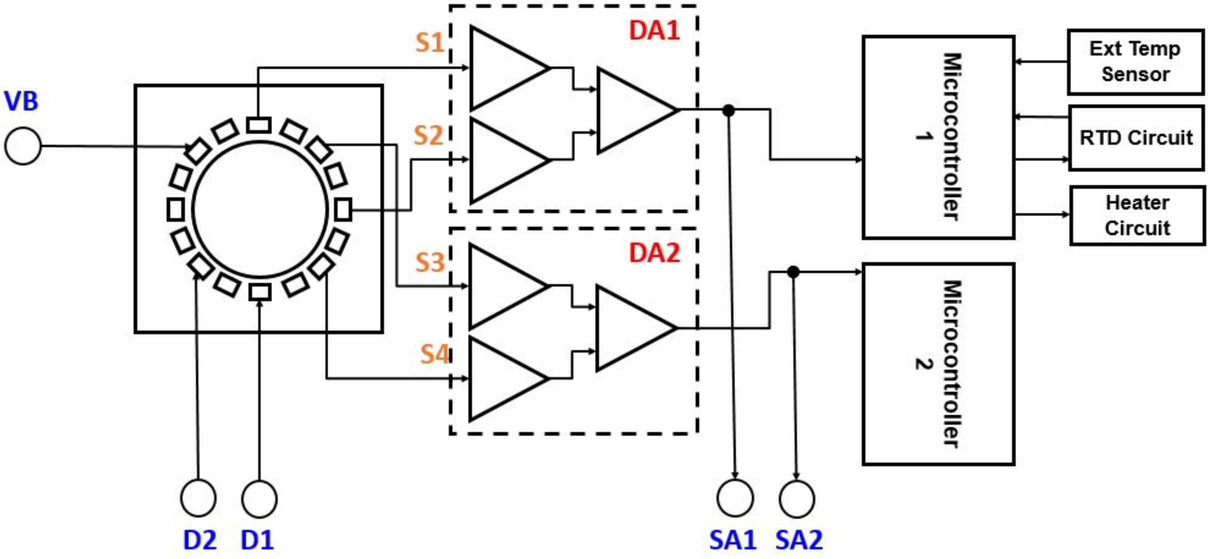

Figure 4.11: Schematic for the PCB.

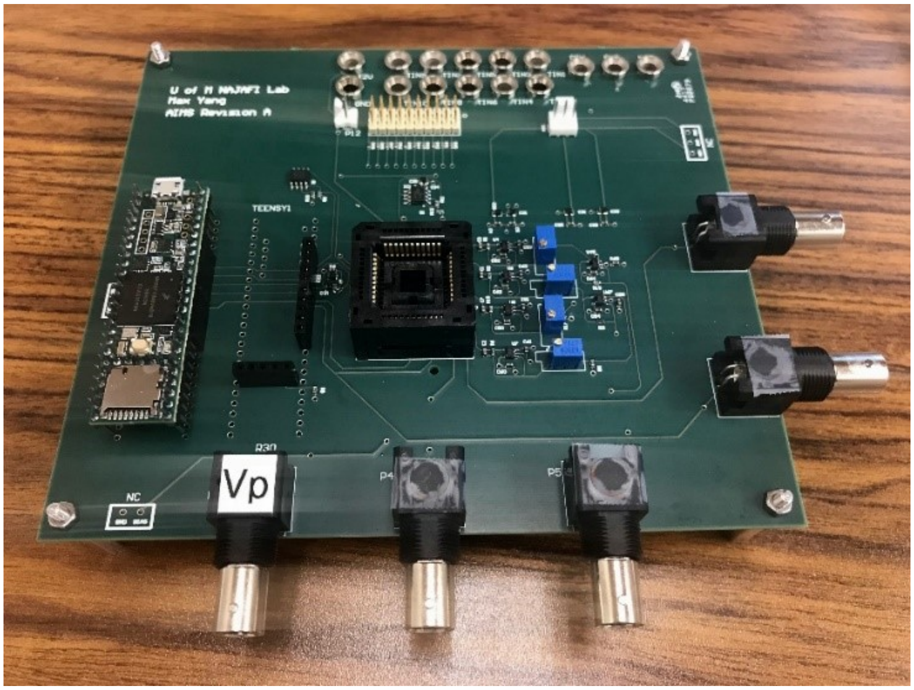

Figure 4.12: Fabricated and soldered PCB.

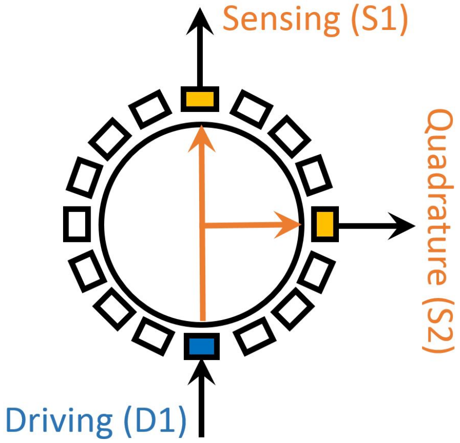

Figure 4.13: Driving and sensing electrodes for the BB shell resonator.

The test setup to measure the temperature effect on the vacuum-sealed shell resonators is shown in Figure 4.14. The manufactured PCB is placed in a convection oven chamber (ESPEC SH-240), and electrical connections are established through a feed-through hole on the sidewall of the chamber. The temperature was then changed from -20 °C to 60 °C with an increment of 10 °C, and the ring-down time measurement was conducted after the temperature was confirmed stabilized. Furthermore, the measurement at each temperature point was repeated five times to ensure that the shell resonator is stable. Measurement results of resonant frequencies and ring-down times of the four vacuum-sealed shell resonators are shown in Figure 4.15 and Figure 4.16, respectively. As shown, the resonant frequencies are almost linearly proportional to temperature, and temperature coefficient of frequency (TCF) ranges from 76.8 ppm/K to 98.2 ppm/K. Finally, the change in the ring-down time during the test was found ranging from 15 % to 81 %, and the temperature effect was found to be non-linear.

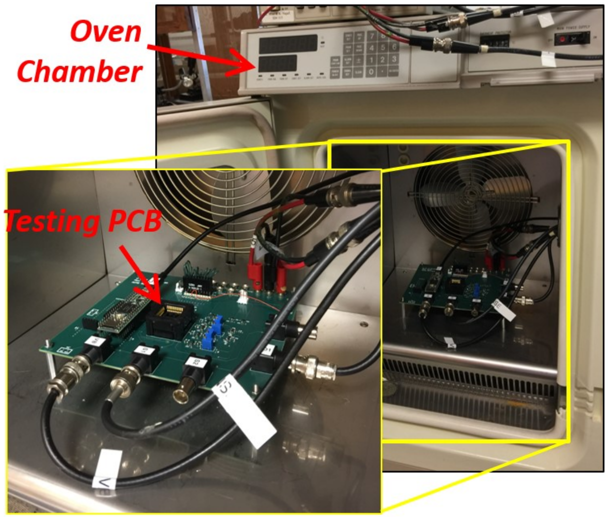

Figure 4.14: Test setup for thermal-cycle test.

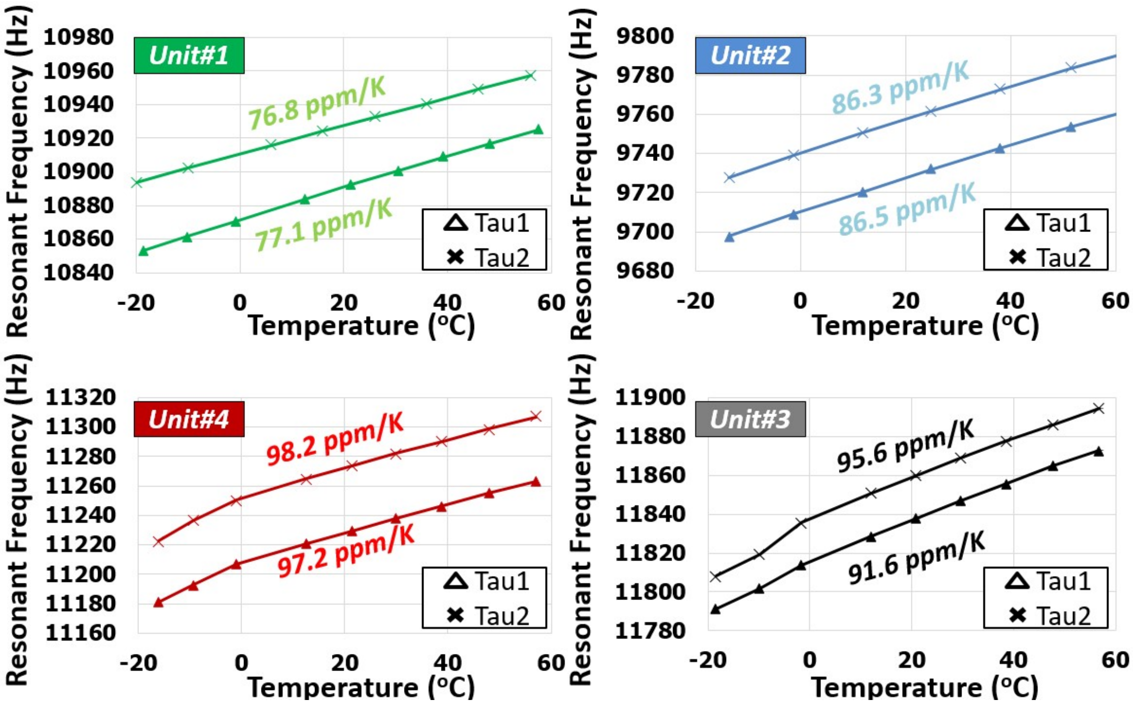

Figure 4.15: Resonant frequency test results of four shell resonators during thermal-cycle.

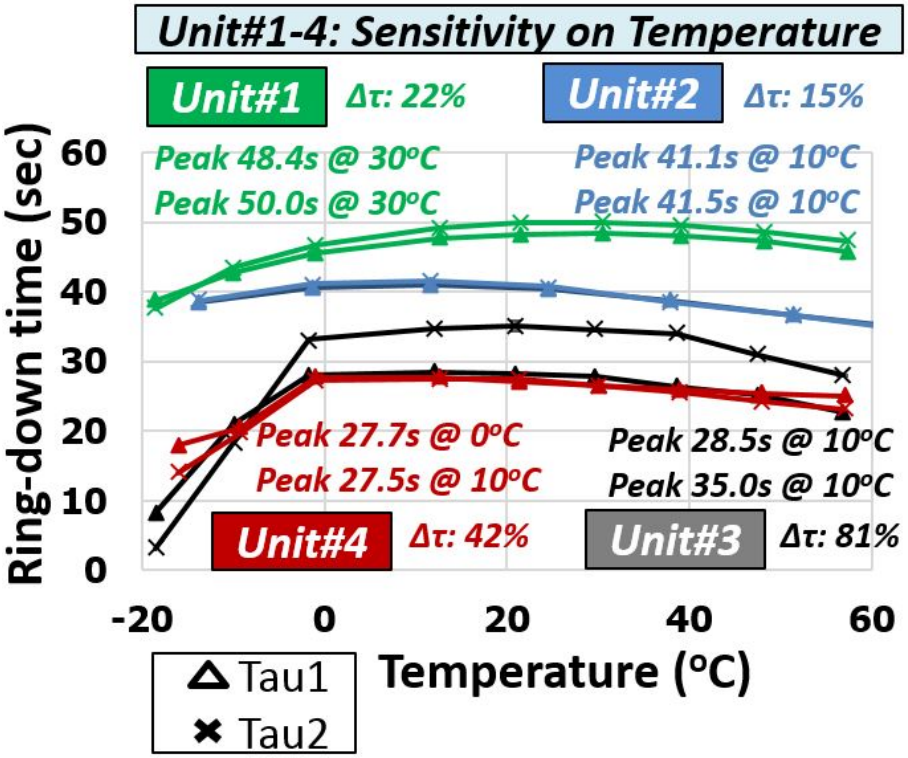

Figure 4.16: Ring-down time test results of four shell resonators during thermal-cycle.

4.1.3 Stress Effect on BB Shell resonator

As mentioned in the previous chapter, mechanical stress on most MEMS inertial sensors can result in undesirable errors in the measurement outputs, and as such, the BB shell resonator can be susceptible to mechanical stress as well. In order to understand the effect of mechanical stress, a test setup was prepared as shown in Figure 4.17 where direct stress is applied onto a vacuum-sealed shell resonator. In the test setup, the PCB, which was manufactured to measure the ring-down time of the vacuum-sealed shell resonators and described in the previous section, is first placed on an electronic scale, and force is applied onto the top surface of the vacuum-sealed package using a pressing tool. A screw knob of the pressing tool was adjusted to induce forces that correspond to 0 g, 400 g, 800 g, 1200 g, and 3000 g on the vacuum-sealed package. The stress on the package at each force was calculated as:

$$P = \frac{m \cdot g}{A} \tag{4.1}$$

where P is pressure in Pa, g is gravitational acceleration, 9.8 m/s^2, m is mass in kg, and A is contact area of the pressing tool on the LCC package in m^2. Ring-down times were then measured at different stress levels, and plotted over the stress as shown in Figure 4.18. From the result, it was found that the stress degraded the ring-down time of the shell resonator by 10-15 %, which is not very significant when compared with the temperature effect. It should be noted from the plot that the maximum ring-down time on the first resonant frequency (τ_1) was observed when no stress was applied on the package, while the maximum ring-down time on the second resonant frequency (τ_2) was observed when 400 kPa of stress was applied on the package.

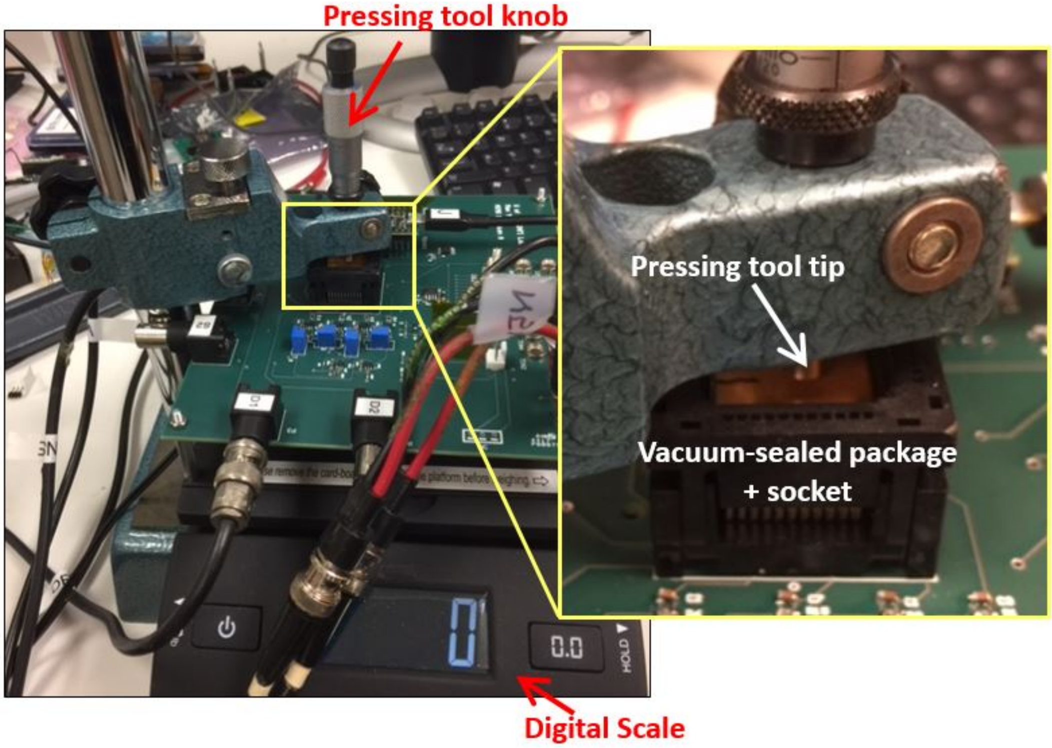

Figure 4.17: Test setup to measure stress effect on the vacuum-sealed shell resonator.

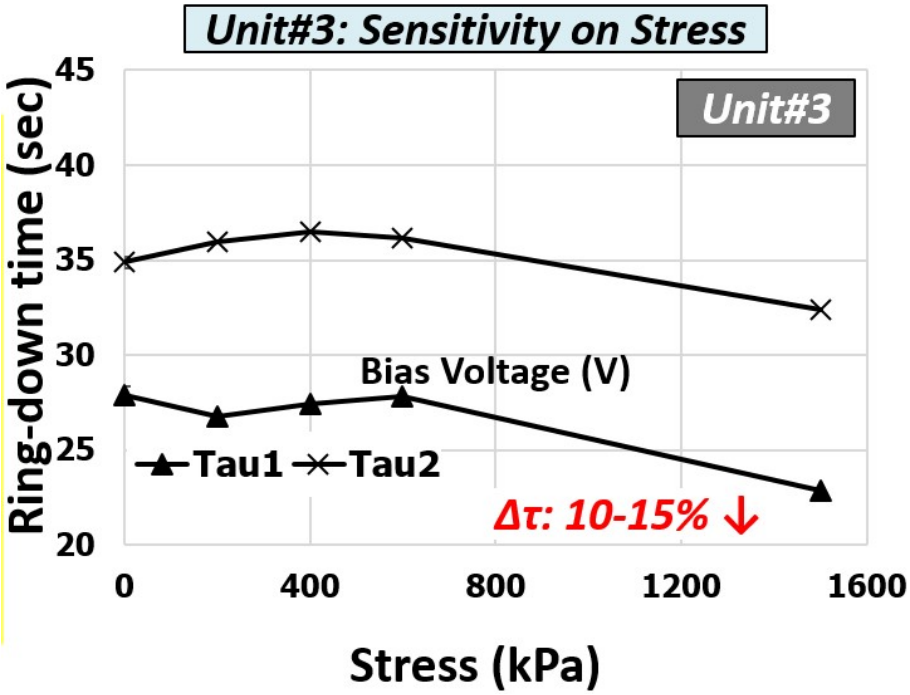

Figure 4.18: Stress effect on the vacuum-sealed shell resonator.

4.1.4 Shock Effect on BB Shell resonator

The shock effect is another important variable that needs to be considered in harsh environment applications [81]. In order to observe shock effect on the vacuum-sealed BB shell resonator, a test setup was prepared as shown in Figure 4.19, where a vacuum-sealed BB shell resonator is fixed on a vertically moving aluminum substrate by using Kapton tape, and a high-g shock impact is delivered to the resonator by dropping the aluminum substrate from a height that corresponds to 5,000 g. The dropping height was calculated by using the following Equation [82]:

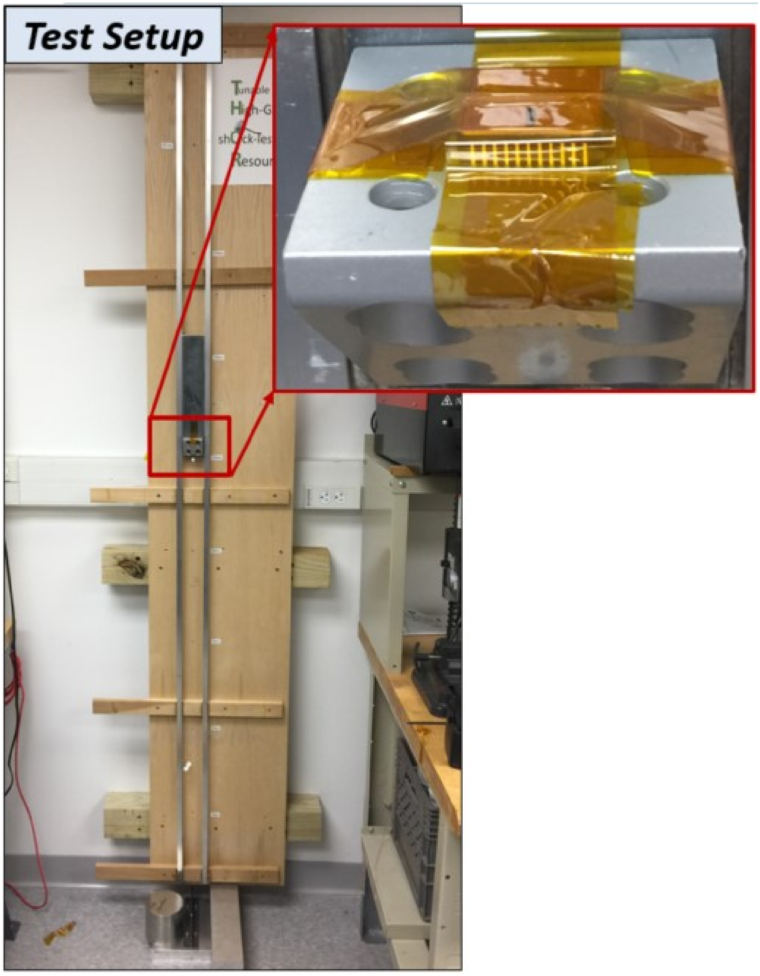

Figure 4.19: High g-shock test setup.

$$a = \sqrt{\frac{E \cdot A \cdot g \cdot d}{h \cdot m}} \tag{4.2}$$

where a is acceleration level of the substrate in m/s^2, E is Youngs Modulus of the substrate in Pa, A is an impact (or compressed) area during the shock test, g is gravitational acceleration, d is the height at which the substrate is dropped, h is the thickness of the substrate, and m is the total mass of the substrate and the packaged shell resonator. Given $E = 69GPa$ for the aluminum substrate, $a = 5,000g, A = 10^{-4}m^2, g = 9.8m/s^2, h = 0.05m$, and $m = 1kg$ in the test setup, the height for 5,000 g shock would be calculated as:

$$d = \frac{a^2 \cdot h \cdot m}{E \cdot A \cdot g} = 1.78m. \tag{4.3}$$

Figure 4.20 shows a cross-section of the vacuum-sealed BB shell resonator that was dropped in the 5,000 g shock impact test. As shown, this resonator was attached to the LCC package through a small fraction of the bottom surface of the assembled shell resonator by using Au-Sn preform to reduce mounting stress on the resonator. This makes the unattached portion of the bottom surface of the assembled shell resonator being suspended. Result of the 5,000 g shock impact test is shown in Figure 4.21. The shell resonator was found undamaged after the shock impact test. However, the glass area of the electrodes substrate where the silicon was etched away was found damaged. It was also found that the damaged area was outside the die-attachment region that the area was suspended before the shock impact test. In order to explain the damage on the suspended glass area, COMSOL FEM simulation was conducted where stress distribution on the electrodes substrate was computed when 5,000 g shock impact was induced on the package. The result is shown in Figure 4.22. The maximum von Mises stress of 13 MPa was found on the suspended glass area near four corners of the substrate, while the stress everywhere else on the glass was not as high. Since the glass (Pyrex 7740) tensile fracture could range from 6.9 MPa to 64 MPa according to [83], it is reasonable to conclude that the stress has caused the suspended glass area to break during the shock impact test.

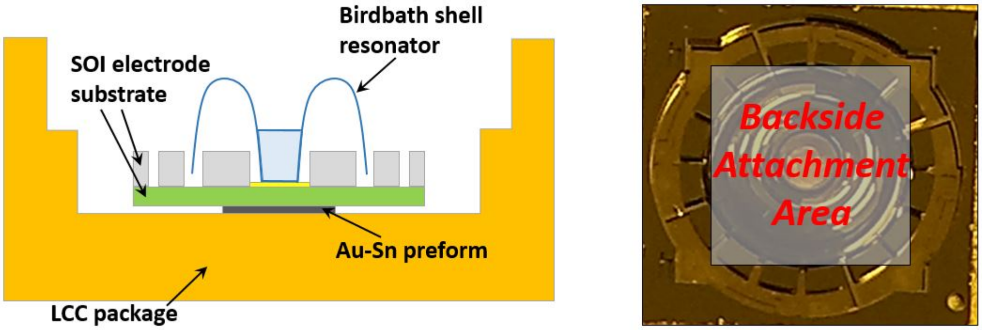

Figure 4.20: (a) Cross-section of the vacuum-sealed birdbath shell resonator, and (b) small attachment area.

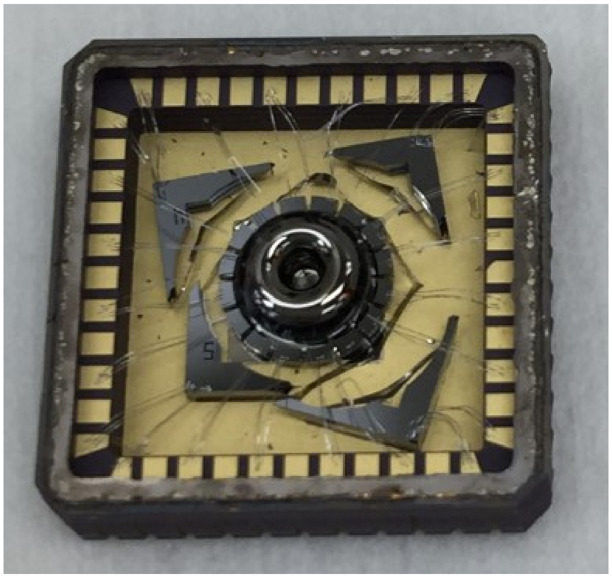

Figure 4.21: Damaged birdbath shell after 5,000 g shock test.

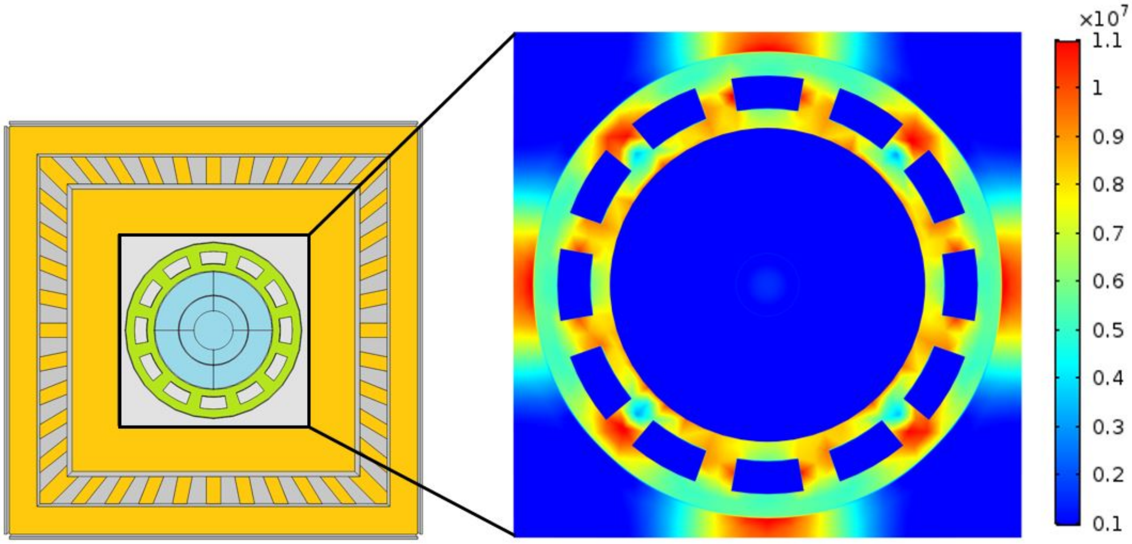

Figure 4.22: Simulation results: stress and displacement of the electrode substrate during 5,000g shock test.

In order to prevent the damage on the glass area on the substrate, therefore, the substrate was made not suspended by attaching the entire bottom surface of the substrate to the LCC package using Au-Sn preform, as shown in Figure 4.23. The 5,000 g shock impact test was then conducted in the same condition as the previous test, in which the packaged shell resonator was fixed on the aluminum substrate and the substrate was dropped to generate 5,000 g shock. As shown in Figure 4.24 the shell resonator and the substrate were found undamaged at this time. Furthermore, in order to understand the shock impact on mechanical properties and performance of the shell resonator, resonant frequencies and ring-down times before and after the shock impact test were measured and summarized in Table 4.1. During the measurements, the exact same test setup was prepared, including bias voltage on the substrate (100 V), temperature (295 K), locations of driving and sensing electrodes, and amplitude of the signal sensed from the sensing electrode. From the test result, it was found that the first resonant frequency (τ_1) changed by 30 ppm, while the second resonant frequency (τ_2) changed by 335 ppm after the shock impact test. Furthermore, the ring-down time at the first resonant frequency was increased by 40 %, while the ring-down time at the second resonant frequency was decreased by 34 %. A possible explanation for the change in the ring-down time is the change in the gap between the electrode and the rim of the shell resonator. In other words, if the gap changes, then the amplitude of the signal at the driving electrode has to be changed to generate a good level of amplitude in the signal at the sensing node, which then would cause the ring-down time to change [10].

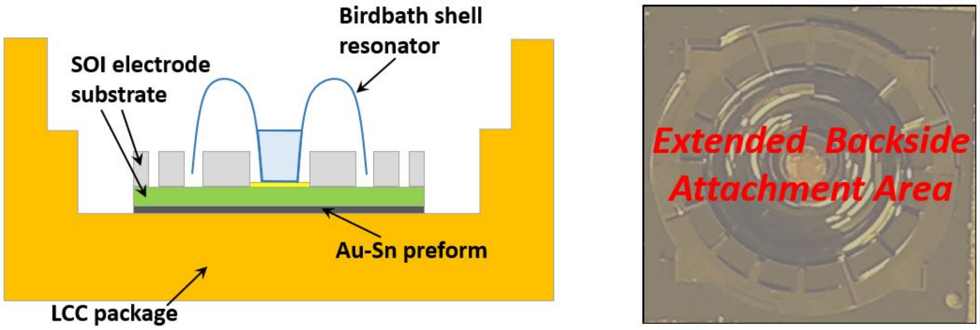

Figure 4.23: (a) Cross-section of the vacuum-sealed birdbath shell resonator, and (b) extended attachment area.

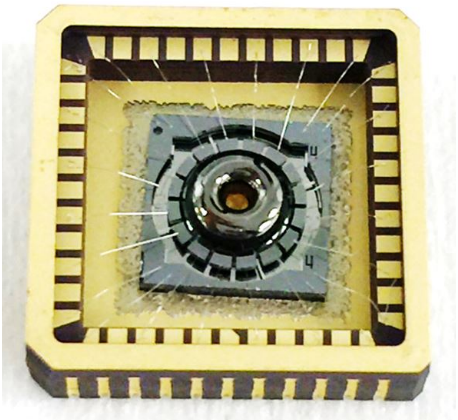

Figure 4.24: Undamaged birdbath shell after 5,000g shock test.

Table 4.1: Performance comparison between before and after the shock test

Condition	Resonant Frequency		Ring-Down Time	
	f_1 (kHz)	f_2 (kHz)	τ_1 (s)	τ_2 (s)
Before Shock Test	10.1071	10.1353	12.29	12.24
After Shock Test	10.1068 (30 ppm)	10.1319 (335 ppm)	17.16 (40% ↑)	8.11 (34% ↓)

4.1.5 Bias Voltage Effect on BB Shell resonator

The bias voltage, as discussed in Chapter II, affects the performance of the MEMS inertial sensors significantly by changing physical properties of the sensors, such as softness of the structure of the sensors, and thus this effect should be investigated on the BB shell resonator as well. In order to observe the bias voltage effect on the shell resonator, the bias voltage was changed from 30 V to 130 V, and the ring-down times at two resonant frequencies in the wine-glass mode were measured at each bias voltage. The results are shown in Figure 4.25. The two resonant frequencies were inversely proportional to the bias voltage. Also, the ring-down times at the first (τ_1) and second (τ_2) resonant frequencies were inversely proportional to the bias voltage and dropped by 50 % and 74 %, respectively, as the bias voltage was changed from 30 V to 130 V. To date, no study on the fused-silica BB shell resonator has reported the effect of the bias voltage on the ring-down time, and the reason for this effect is not clear. This can be due to the change in the gap between the electrode and the rim of the shell resonator, the change in the softness of the shell resonator, or the change in stress effect from the applied electric field at different bias voltages **??**.

Fortunately, the output voltage of commercially available charge pumps changes less than a few % [84], which corresponds negligible change in the performance of the shell resonator. Therefore, the bias voltage effect on the shell resonator will not be as significant as other environmental effects, including temperature and shock effects, by carefully choosing a well-designed charge pump.

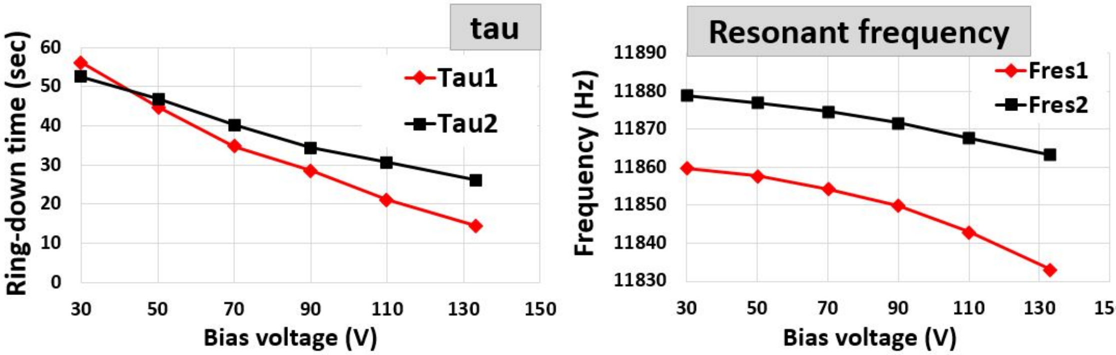

Figure 4.25: Ring-down time (left) and resonant frequency (right) over bias voltage.

4.2 Oven-Controlled Birdbath Shell Resonator

From the last few sections, four environmental effects—temperature, stress, shock, and bias voltage—on the vacuum-sealed BB shell resonator were investigated, through which it was found that the temperature and shock effects change the performance of the shell resonator much more than the stress and bias voltage effects do. Furthermore, designing a DOCIS that addresses all four environmental effects simultaneously is almost impossible since there will be many complicated trade-offs in the design. Therefore, a DOCIS packaging design that would mitigate the two most problematic environmental effects for the BB shell resonator, the temperature and shock effects, will be proposed and discussed in this section.

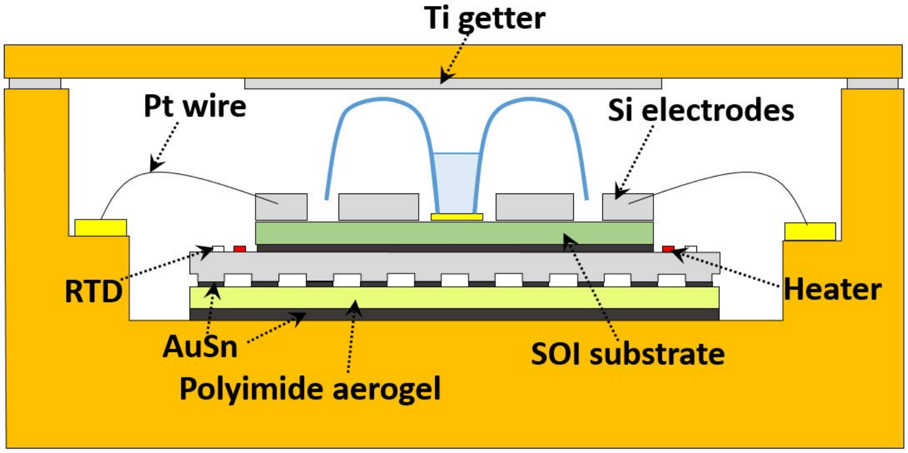

Figure 4.26: A proposed DOCIS design for the BB shell resonator.

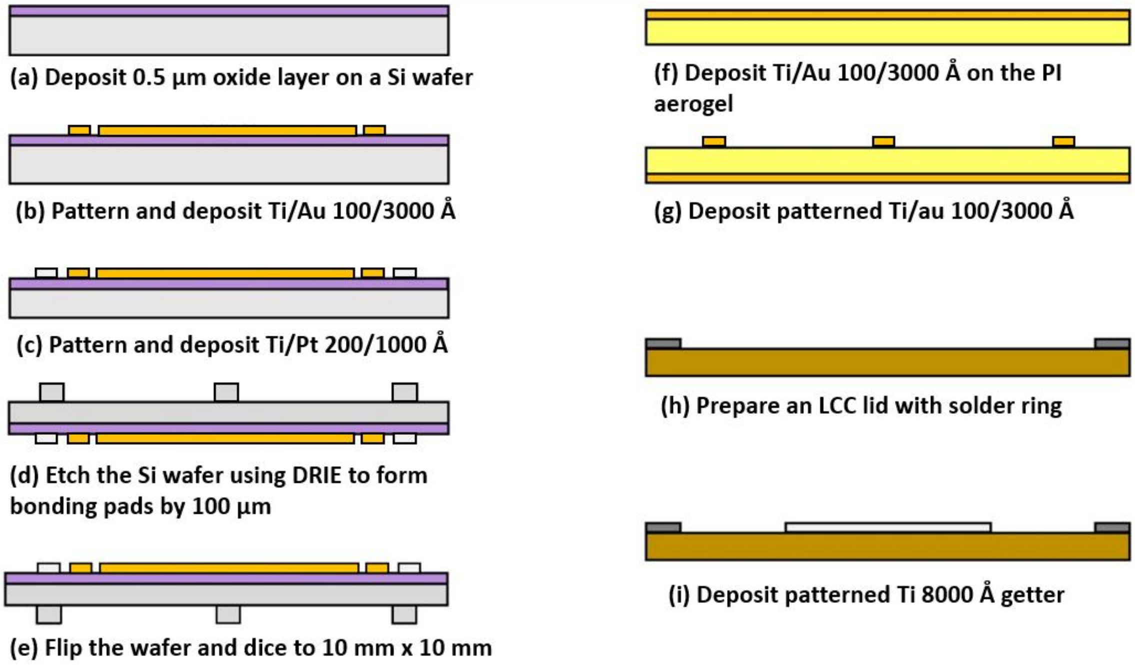
(a) Deposit 0.5 µm oxide layer on a Si wafer

(b) Pattern and deposit Ti/Au 100/3000 Å

(c) Pattern and deposit Ti/Pt 200/1000 Å

(d) Etch the Si wafer using DRIE to form bonding pads by 100 µm

(e) Flip the wafer and dice to 10 mm x 10 mm

(f) Deposit Ti/Au 100/3000 Å on the PI aerogel

(g) Deposit patterned Ti/au 100/3000 Å

(h) Prepare an LCC lid with solder ring

(i) Deposit patterned Ti 8000 Å getter

Figure 4.27: Fabrication process flow for the proposed DOCIS for the BB shell resonator.

Figure 4.26 shows a schematic of the proposed DOCIS packaging design. This design is similar to the DOCIS that was proposed in the previous chapter, except the silicon mechanical isolation stage is replaced with a silicon stage that does not include any suspended structures to prevent it from breaking due to high-g shock impact. The fabrication process flows for the silicon stage and the thermal isolation stage are shown in Figure 4.27. First, a 500 mm-thick silicon wafer is prepared and a 0.5 μm-thick oxide layer is deposited on the wafer to prevent electrical shortage between metal layers that will be deposited and patterned on the silicon wafer in later steps (a). The wafer is then spin-coated using SPR 220 3.0 at 3 krpm, developed for 7 seconds using a mask plate, deposited with Ti/Au (100/3000 Å) using an evaporator (Enerjet Evaporator), and patterned using the ultrasonic lift-off process in PRS-2000 at 80 °C for 20 minutes to fabricate a heater and electrical connections (b). This wafer is then again spin-coated using SPR 220 3.0 at 3 krpm, developed for 7 seconds using a mask plate, deposited with Ti/Pt (200/1000 Å) using an evaporator (Enerjet Evaporator), and patterned using the ultrasonic lift-off process in PRS-2000 at 80 °C for 20 minutes to fabricate a RTD (c). After the deposition and patterning are completed, the wafer is flipped upside down, spin-coated using SPR 220 3.0 at 1 krpm, developed for 13 seconds using a mask plate, soft-baked for 120 seconds, and mounted on a blank silicon wafer to dry-etch (STS Pegasus 4) to form bonding pads (d). The etch rate for this pattern was 3.45 μm/min using LNF Recipe 1 at 20 °C, and the wafer was etched for 29 minutes (i.e., 100 μm etching.) Finally, the wafer is diced using a dicing tool (ADT 7100 Dicing Saw) (e).

Simultaneously, a 12 mm x 12 mm x 250 μm aerogel substrate is prepared and the entire bottom surface of the substrate is metal-coated with a Ti/Au (100/3000 Å) layer using an electron beam evaporator (Enerjet Evaporator) (f). A patterned Ti/Au layer (100/3000 Å) is then deposited on the top surface of the substrate using a silicon shadow mask and an electron beam evaporator (Enerjet Evaporator) to align the silicon substrate on the aerogel (g). The aerogel substrate is then attached to the LCC package using an Au-Sn (Au 80 %- Sn 20 %) preform at 340 °C for 20 minutes to form eutectic bonding between the aerogel substrate and the LCC package. The prepared silicon stage in (e) is then attached to the aerogel sheet using silver epoxy adhesive (ABLEBOND 84-1 LMI, Henkel AG & Company). An assembled shell resonator is then attached to the silicon stage using an Au-Sn (Au 80 %-Sn 20%) preform at 340 °C for 20 minutes to for eutectic bonding between the assembled shell resonator and the silicon stage. The electrical wires are then connected from electrodes on the assembled shell resonator to electrical pins on the LCC package using 0.5-mil Pt wire. After the wire-bonding connections, an LCC combo lid (CL-62010, Spectrum Semiconductor Materials, Inc.), which has an Au-Sn solder ring welded along the perimeter, is prepared, on which a Ti (8000 Å) getter is deposited using the electron beam evaporator (Enerjet Evaporator) (h, i). Finally, the entire assembly is vacuum-sealed at 340 °C for 20 minutes and 250 °C for 2 hours to activate the getter in a wafer bonder (EVG 520IS, Semi-Automated wafer Bonding System). More detailed view of the oven-controlled BB shell resonators is shown in Figure 4.28.

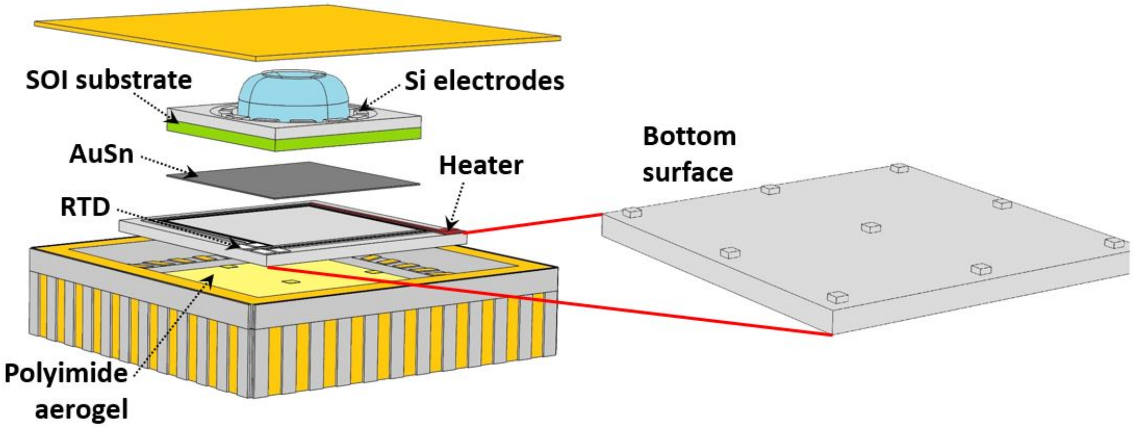

Figure 4.28: Bird view of the oven-controlled BB shell resonator.

In order to compute the thermal resistance of the DOCIS for the BB shell resonator, a COMSOL FEM simulation was conducted where the surrounding temperature (i.e., the package temperature) was set to 0 °C and an appropriate amount of Joule heating power was supplied to the heater on the isolation stage to control the temperature of the RTD to 80 °C. Furthermore, the pressure level inside the package was set to 0.1 mTorr. Figure 4.29 shows the thermal simulation result. As a result, the heater on the silicon stage consumed 72 mW to maintain the RTD temperature at 80 °C at the surrounding temperature of 0 °C. Therefore, the expected thermal resistance of the DOCIS would be 1,111 K/W.

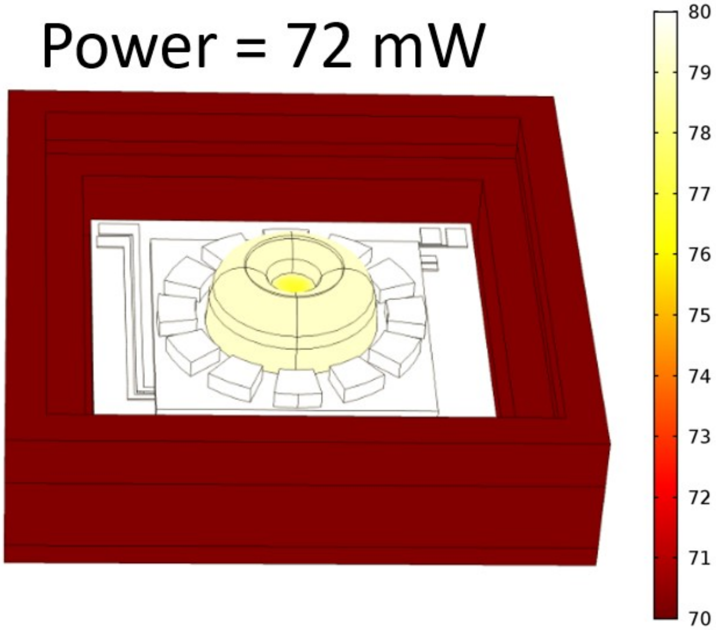

Figure 4.29: Thermal resistance simulation results.

4.3 Potential Challenges in Oven-Controlled BB Shell Resonator

4.3.1 Thermal Gradient on Shell Resonator

Although the RTD temperature on the silicon stage is controlled at a constant temperature in the DOCIS for the BB shell resonator, there will be a finite temperature difference throughout the surface of the shell resonator due to the low thermal conductivity of fused silica, as shown in Figure 4.29. Furthermore, this temperature difference will change as the surrounding temperature changes, which then would cause temperature and temperature-induced stress effects on the shell resonator even when the RTD temperature is precisely controlled. In order to quantify the temperature difference on the surface of the shell resonator as the surrounding temperature changes, a simulation was conducted at different surrounding temperature values. In the simulation, the pressure level inside the package was 1 mTorr, the control set temperature was 80 °C, and the surrounding temperature was changed from -40 °C to 70 °C. As shown in Figure 4.30, the temperature difference was 1.7 °C at -40 °C, and it changed to 0.17 °C at 70 °C. Therefore, there should be a proper method to address this issue for a more accurate oven-control system, and two possible solutions are suggested here.

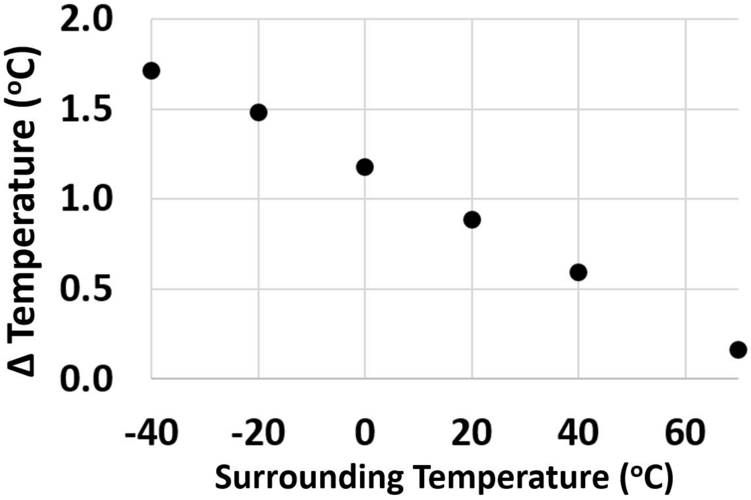

Figure 4.30: Temperature difference on the surface of the shell resonator over surrounding temperature.

The first suggested method is a resonant frequency-based oven-control system in which one of the resonant frequencies of the shell resonator is measured and utilized as a temperature reference [85]. As shown in Figure 4.31, the signals sensed from the sensing electrodes (S1 & S2) are differentially amplified using TIAs and a differential amplifier, and the amplified signal is then read by an analog input channel in a microcontroller. Frequency of this signal is now measured by a frequency counter in the microcontroller, which is then converted to a temperature value using a relationship between the resonant frequency and the temperature found in a separate thermal-cycle experiment, as in Figure 4.15. The calculated temperature is then compared to a set temperature to provide an appropriate amount of current to the heater on the silicon stage for Joule heating, and the process is repeated indefinitely. As mentioned in Chapter II, the actual temperature of the shell resonator in this method would be fluctuated by ±0.4 °C, given that the frequency counter used in the oven-control system is based on the reference clock in Teensy 3.2. It should be noted that this method will require a calibration process for each shell resonator, in which the relationship between the resonant frequency and the temperature is characterized. Since the resonant frequency also depends a lot on the bias voltage on the shell resonator as well as temperature, the bias voltage will need to be considered in the calibration process.

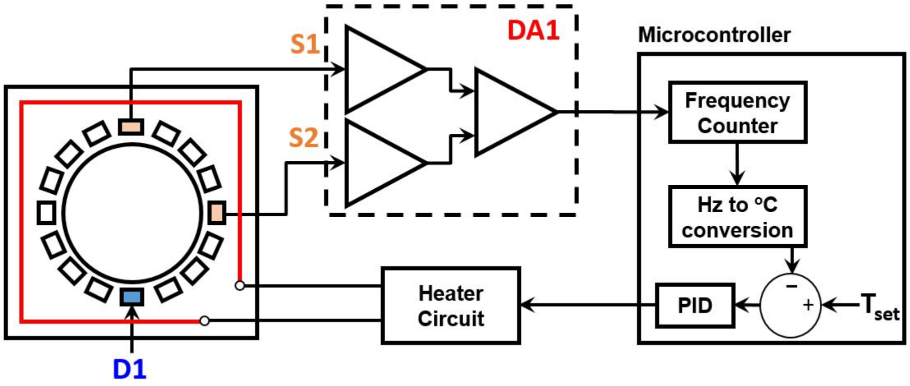

Figure 4.31: Block diagram of frequency-controlled oven-control system.

The second suggested method is an oven-control system with a better thermal equilibrium through extended silicon electrodes. In this method, the silicon electrodes on the electrodes substrate are made taller so that high-temperature silicon electrodes surround the most surface of the shell resonator, as shown in Figure 4.32. In principle, this method is similar to the zero-gradient crystal oven in [86] where a crystal resonator is surrounded by a thermally high-conductive material all around, and the material is heated to a constant temperature. As such, the maximum temperature difference on the surface of the shell resonator would be reduced. In order to verify this, a COMSOL FEM simulation was conducted and the result is plotted over the height of the silicon electrodes when the pressure level inside the package was 1 mTorr and 5 mTorr (Figure 4.33). At 1 mTorr, the maximum temperature difference was found decreasing from 1.8 °C to a sub 1 °C as the height of the electrodes increased from 0 to 2100 μm. Similarly, at 5 mTorr, the maximum temperature difference was found decreasing from 10 °C to 6.6 °C as the height of the electrodes increased from 0 to 2100 μm. Therefore, this method is expected to effectively reduce the thermal gradient on the surface of the shell resonator.

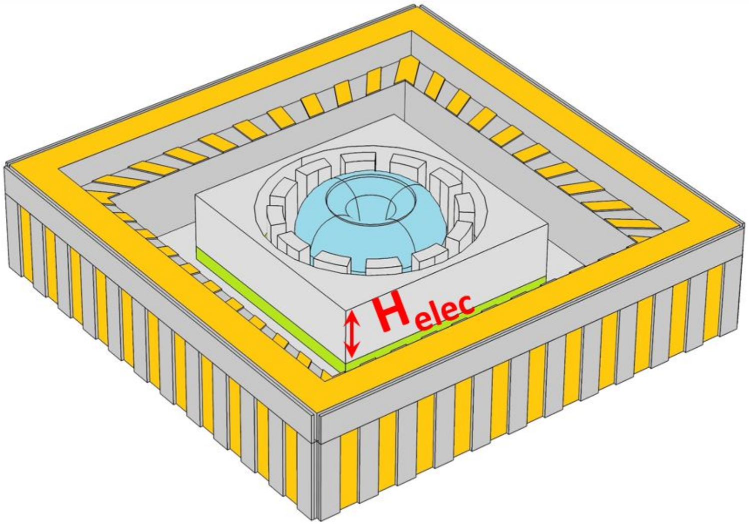

Figure 4.32: Geometry of an oven-control system with better thermal equilibrium through extended silicon electrodes

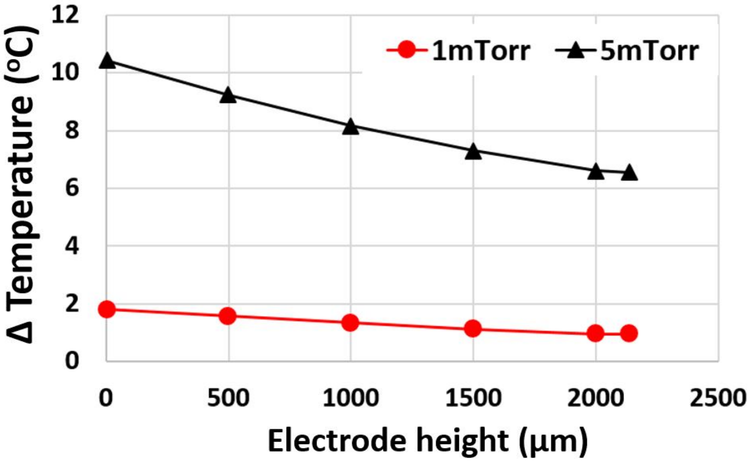

Figure 4.33: The maximum temperature difference on the shell resonator over the height of silicon electrodes.

4.3.2 Reduced Bonding Strength

Another potential challenge is the reduced bonding strength due to the reduced bonding area, which was briefly discussed in Chapter III. In order to produce a high enough thermal resistance in the DOCIS, the attachment between the silicon stage and the aerogel was established only through bonding pads on the bottom surface of the silicon stage, which is a very small fraction of the entire surface, and this may cause the DOCIS to be susceptible to high shock impact. Therefore, the effect of the attachment area on the bonding strength and the thermal resistance will be discussed in this section.

Given that the unit shear strength of the silver epoxy adhesive (ABLEBOND 84-1 LMI, Henkel AG & Company) is 4.75 $kg \cdot f/mm^2$ and is linearly proportional to the bonding area [75, 76], and the total weight of the shell resonator, electrodes substrate, and silicon stage is 5 grams, the maximum shock tolerance and the thermal resistance of the DOCIS are calculated over the attachment area. The results are plotted in Figure 4.34.

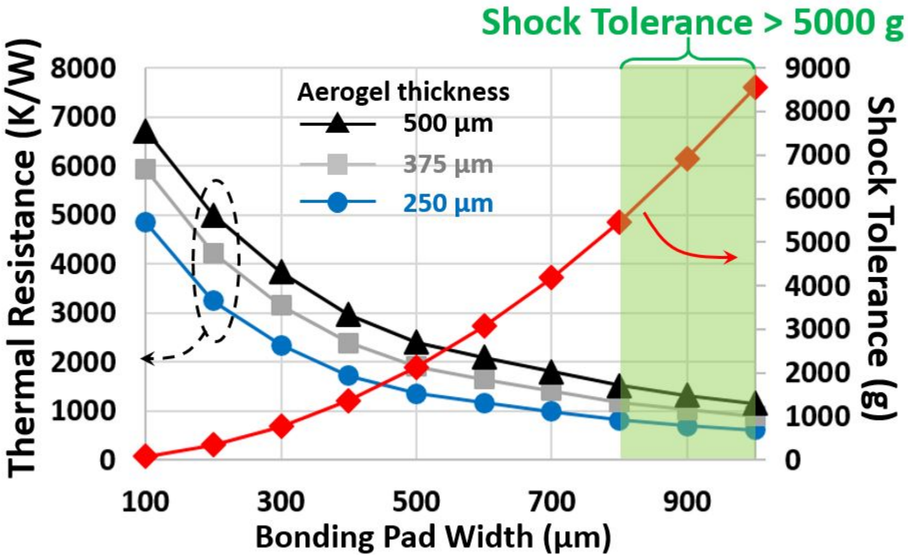

Figure 4.34: Maximum shock tolerance and thermal resistance vs bonding area.

The bonding pad width in the plot indicates the width of each of a 9 x 9 array of square-shaped bonding pads. As a result, it was found that the bonding pad width has to be larger than 800 μm (or a total area of 2.4 x 2.4 mm^2) to tolerate a shock impact higher than 5,000 g. This would be translated to the total thermal resistance of 817 K/W, given that the thickness of the aerogel substrate is 250 μm, the total number of platinum bonding wires is 22, and the pressure level in the vacuum-sealed package is lower than 1 mTorr. If the DOCIS were to survive 5,000 g and provide a thermal resistance higher than 1,000 K/W, the thickness of the aerogel can be increased, as shown in Figure 4.34. When the thickness of the aerogel substrate was increased to 375 μm and 500 μm, the total thermal resistances were improved to 1180 K/W and 1520 K/W, respectively. Therefore, the bonding pad width and the thickness of the aerogel substrate will need to be adjusted upon the specifications required by applications.

CHAPTER V

Conclusions

In this chapter, the contributions of the present study are summarized and possible future works are recommended.

5.1 Summary

In Chapter I, the temperature effect on MEMS inertial sensors and inertial navigation system (INS), and other environmental effects, including stress, shock, and vibration, on the MEMS inertial sensor were presented. Through the modelling of INSs using state-of-the-art inertial sensors and simulations using MATLAB, it was found that the temperature effect on the INS is critical, and the effect becomes more severe on the INSs that use higher performing MEMS inertial sensors, due to the fact that temperature-induced bias errors of the higher performing MEMS inertial sensors are still comparable to or slightly lower than the lower performing MEMS inertial sensors [38]. Therefore, temperature and other environmental effects need to be properly mitigated to develop actual high performing MEMS inertial sensors. In order to mitigate the temperature effect on the MEMS inertial sensors, previous studies proposed various approaches, and they can be classified into three categories: 1) a fundamental approach where structural and material properties of the MEMS inertial sensors are changed to mitigate the temperature effect, 2) a compensation method where algorithms or electrical circuits are used to compensate for the temperature effect, and 3) an oven-control method where the MEMS inertial sensors are vacuum-sealed in an additional package and the MEMS inertial sensors are controlled at a constant temperature. Among these methods, the oven-control method showed the highest reduction in the temperature-induced bias drift to date [44].

In Chapter II, details of the single stage oven-controlled inertial sensors (SOCIS) was presented, as an extended study from Ref. [50]. MEMS inertial sensors that are to be packaged in the SOCIS were first investigated from among the good performing commercial off-the-shelf (COTS) MEMS inertial sensors, where the outputs of six commercial inertial measurement units (IMUs) were measured at room temperature to evaluate and compare their noise performances by using Allan Deviation (ADEV) plots. Based on the evaluation result, Invensense MPU-6050 was found to be the most suitable for the SOCIS due to the low gyroscope noise. After the selection process was completed, several methods to reduce power consumption of the SOCIS were introduced. First, heat losses through solid and gas conductions were analyzed to understand the dominant heat loss path and minimize heat loss through the dominant path by using an equivalent electrical thermal circuit. Second, the heater control algorithm was changed from an analog method to a digital pulse width modulation (PWM) method to improve the efficiency of the heater electronics. By using this method, it was found that the power efficiency of the electronics was improved from 53 % to 94.4 %. Finally, a multiple set point (MSP) algorithm was applied to adjust the temperature set point depending on the surrounding temperature to reduce the temperature difference (ΔT) between the set point and the surrounding temperature, rather than having an invariant temperature set point at all time. Through this method, it was found that the maximum reduction in the heater power consumption was around 88 %. After the methods to reduce power consumption of the SOCIS were discussed, the thermal stability of the SOCIS was discussed by studying temperature sensing and control methods. A good temperature control method, which would provide a good precision of the oven-control system (i.e., 1 σ of the IMU temperature), was developed by using a PID controller, the Ziegler-Nichols tuning method, and a fine-tuning method. As a result, the stability was found to be 7.8 m°C (1 σ) during a thermal-cycle test from -40 °C to 85 °C at the rate of 1 °C/min. On the other hand, several available temperature sensing methods—on-chip solid-sate temperature sensor in the commercial IMU, a temperature sensing technique using temperature coefficient of frequency (TCF) of the resonant frequency of a gyroscope in the commercial IMU, and an RTD sensor on the isolation stage in the SOCIS— were studied and compared to provide an accurate oven-control system by representing the actual temperature of the MEMS inertial sensors. As a result, the on-chip solid-sate temperature sensor in the commercial IMU was found to be the most accurate. After thermal stability was discussed, the isolation stage in the SOCIS was designed to provide both thermal and mechanical isolation capabilities. Since a single isolation stage was used to isolate both thermal and mechanical effects on the MEMS inertial sensors, trade-offs between vibration isolation, stress isolation, and thermal isolation capabilities were considered in the design of the isolation stage. As a result, the isolation stage was designed to filter out vibrations at a frequency higher than 3.1 kHz, and mitigate the PCB stress effect by a factor of 37 on average. After the design of the isolation stage was completed, the thermal isolation capability and other performances were discussed. In order to understand a potential degradation in noise performance and mitigation in the temperature-induced bias drifts of the SOCIS, both the SOCISs, in which Invensese MPU-6050s were packaged, and regular Invensense MPU-6050s were prepared. Their noise performances and the temperature-induced bias drifts were compared at room temperature and during a thermal-cycle from -40 °C to 70 °C, respectively. According to the noise performance result, the SOCISs showed 5-8% higher ARW and VRW values than the regular MPU-6050s, which is expected due to a higher level of mechanical and electrical white noises at the elevated temperature. On the other hand, the SOCISs showed 11-18% lower BI values than the regular MPU-6050s, which is an unexpected result. We think this is because of higher rate ramp (RR) and acceleration ramp (AcR) in the regular MPU-6050s than those in the SOCISs, as the temperature variation during the oven-control in the SOCISs, which was about 10 m°C, is much smaller than the temperature variation when the sensors were exposed to room temperature, which was found to fluctuate by 1 °C for 24 hours of measurement. According to the temperature-induced bias drift result, the average temperature-induced bias drifts of 10 SOCISs were improved by factors of 4.2 and 9.2 for gyroscopes and accelerometers, respectively, while the best improvement was found in an SOCIS where the bias drifts were improved by factors of 108 and 13 for gyroscopes and accelerometers, respectively. After that, COMSOL FEM simulations were conducted to understand residual temperature-induced bias drifts in the inertial sensors, from which it was found that the temperature gradient on the isolation stage in the SOCIS is very high and the gradient changes as the surrounding temperature changes. We think this causes a change in the temperature-induced stress on the inertial sensors during a thermal-cycle test, and thus the residual temperature-induced bias drifts still remain in the SOCIS. Since the temperature-induced stress is inevitable in the SOCIS due to the fact that the isolation stage in the SOCIS has to be made of thermally low-conductive material, we concluded that the amount of temperature-induced stress could be further optimized for higher performance in gyroscopes. another approach needs to be developed to address this issue.

Additionally, other non-ideal effects in the SOCIS—bias voltage, unexpected high bias drift in Z-axis accelerometers, and mounting stress—were found and discussed. The effect of the bias voltage on the gyroscope outputs were first examined by changing the bias voltage from 15 V to 35 V at room temperature. The result showed that resonant frequencies and rate outputs of the gyroscopes changed significantly as the bias voltage changed. This change, however, turned out to be a minor issue, after it was found that the charge pump, which was used to supply the bias voltage, is normally very stable. After that, unexpected high bias drift was observed in the Z-axis accelerometer in the SOCIS, and an apparent correlation between the bias drift and the voltage across the heater during the thermal-cycle test was found from an analysis of 24 OCISs, which suggested that the voltage across the heater should be reduced by decreasing the electrical resistance of the heater on the isolation stage. Finally, the mounting stress due to CTE mismatch among the isolation stage, epoxy molding compound (EMC) package for the commercial IMU, and silicon MEMS inertial sensors was studied through FEM simulations. According to the simulation result, the mounting stress during thermal-cycle can be reduced by a factor of 2.8 by eliminating EMC packaging material for the silicon MEMS inertial sensors. Finally, INSs using the SOCIS and regular MPU-6050 were modeled to estimate position errors of the INSs due to 1.5 °C thermal shock. As a result, the error of the INS using the SOCIS was smaller by a factor of 12 than the INS using the regular MPU-6050.

In Chapter III, the double isolation stage oven-controller inertial sensors (DOCIS) was proposed to address the problems that were found in the SOCIS in Chapter II. In this new OCIS, the mechanical isolation stage is made of silicon, which is thermally high conductive, instead of glass, which is thermally low conductive, to minimize thermal gradient on the isolation stage during a thermal-cycle test. Since this platform cannot provide a good thermal isolation capability due to the high thermal conductivity, a thin thermal isolation stage made of polyimide aerogel was added under the silicon mechanical isolation stage. The polyimide aerogel has an extremely low thermal conductivity of 0.03 W/m·K and much more enhanced mechanical durability than a typical silica aerogel. In order to improve the thermal isolation capability further, the bottom surface of the silicon isolation stage was dri-etched to form bonding pads to reduce the contact area between the aerogel substrate and the silicon stage, and thus to reduce heat loss through the aerogel substrate. Moreover, in order to reduce heat loss through electrical connections from MPU-6050 to the LCC package, 0.5-mil Pt wire, which has about a third of the thermal conductivity and a half of the diameter of a typical Al wire, was used. After that, simulation and experiment results of the thermal resistance of the DOCIS were compared, during which an important concept called "effective contact area" was introduced to explain the discrepancy between the simulation and experiment results. Finally, simulations were conducted to confirm that due to the reduced thermal gradient on the mechanical isolation stage, reduced temperature-induced stress, increased mechanical design flexibility, and reduced mounting stress, the DOCIS would mitigate the temperate-induced bias drifts by a higher factor than the SOCIS does.

In Chapter IV, the DOCIS was applied to one of the state-of-the-art gyroscopes, the fused silica birdbath (BB) shell resonator developed by the University of Michigan. Prior to designing and developing the DOCIS for the resonator, the environmental and non-ideal effects on the shell resonator, including inconsistent performance during and after a vacuum-sealing process, temperature, stresss, shock, and bias voltage, were studied and discussed through experiment and simulation results. Among these, temperature and shock effects were found the most critical, and therefore, a DOCIS was designed to effectively mitigate these two effects. According to simulation results, the DOCIS will survive a shock impact higher than 5,000 g, if the width of each of an array of 9 x 9 bonding pads is equal to or larger than 800 μm. Furthermore, the corresponding thermal resistance was found to be 817 K/W with 250 μm-thick aerogel, 22 bonding wires, and low pressure (lower than 1 mTorr). Finally, the thermal resistance can be increased to 1180 K/W and 1520 K/W by increasing the thickness of the aerogel substrate to 375 μm and 450 μm, respectively. Although the BB shell resonator was not fully integrated with a DOCIS isolation stage due to lack of time and limited availability of shell resonators, the findings of this research will be used in future efforts to fabricate a complete isolated and oven-controlled BB shell resonator.

5.2 Contributions

In this section, the contributions of the present study is summarized:

1) Understanding the effect of temperature on the performance of inertial navigation systems that use MEMS inertial sensors: a simulation tool, equations for a strap-down inertial navigation system, and noise and temperature sensitivity data of state-of-the-art gyroscopes were used to analyze the temperature effect on the inertial navigation system.

2) Understanding available temperature sensing methods for the SOCIS and selecting the most accurate method among them: available temperature sensing methods in the SOCIS were investigated to find the temperature sensor that represents the actual temperature of the MEMS inertial sensors most accurately.

3) Understanding the effect of strain-induced stress and temperature-induced stress on the SOCIS: the strain-induced stress, which is caused when a structure on which inertial sensors are attached is bent, and the temperature-induced stress, which is caused by the temperature gradient and the change of the temperature gradient on the glass isolation stage in the SOCIS, were investigated and appropriate solutions were suggested to mitigate the stress effects.

4) Understanding the limitations of the SOCIS and proposing a new oven control isolation stage for oven-controlled inertial sensors. This new structure is called DOCIS and overcomes limitations in the SOCIS: two main limitations in the SOCIS—temperature-induced stress and limited design and material selection for the isolation stage—were discussed and potential advantages of the DOCIS were discussed and validated through experiments and simulations. DOCIS allows the designer to optimize thermal and mechanical isolation characteristics independently, thus improving

the overall performance.

5) Understanding non-ideal properties of the fused silica birdbath (BB) shell resonator and proposing the oven-controlled birdbath shell resonator based on the DOCIS: in order to apply the DOCIS packaging technology to the fused silica birdbath shell resonator, non-ideal properties of and environmental effects on the BB shell resonator were studied. After that, the oven-controlled birdbath shell resonator was designed to mitigate some of the non-ideal properties and environmental effects that degrade the performance of the BB shell resonator significantly.

5.3 Recommendations for Future Work

In the present study, the DOCIS using Invensense MPU-6050 and the fused silica BB shell resonator were not vacuum-sealed. Therefore, future work may include vacuum-packaging the DOCIS to empirically validate low temperature-induced stress on the MEMS inertial sensors during a thermal-cycle test and other advantages of the DOCIS over the SOCIS. It should be noted that the EMC package of MPU-6050 should be dissolved away to minimize potential stress on the silicon MEMS die due to CTE mismatch. Furthermore, the aerogel substrate that was used in this study has a relatively lower temperature rating of 250 °C than the 400 °C temperature required for the vacuum-sealing process. Therefore, although it was found through several experiments that the aerogel maintains a good thermal properties after the vacuum-sealing process, it is recommended to use another PI aerogel whose temperature rating is higher than the vacuum-sealing process temperature of 340 °C. Such a PI aerogel is commercially available for purchase in [87].

BIBLIOGRAPHY

BIBLIOGRAPHY

[1] W.J. Hughes. Global positioning system (gps) standard positioning service (sps) performance analysis report. Technical report, Federal Aviation Administration, 2014.

[2] B. W. Parkinson. *Progress in astronautics and aeronautics: Global positioning system: Theory and applications*, volume 2. AIAA, 1996.

[3] E. Foxlin. Pedestrian tracking with shoe-mounted inertial sensors. *IEEE Computer graphics and applications*, 25:38–46, 2007.

[4] Hershberger M.C. Skopek, K. and Gladysz. Gyroscopes and the chemical literature: 18522002. *Coordination chemistry reviews*, 251:1723–1733, 2007.

[5] Trusov A. A. Prikhodko, I. P. and A. M. Shkel. Compensation of drifts in high-Q MEMS gyroscopes using temperature self-sensing. *Sensors and Actuators A: Physical*, 201:517–524, 2013.

[6] Zaman M. F. Sharma, A. and F. Ayazi. A Sub-0.2 $degree$/hr Bias Drift Micromechanical Silicon Gyroscope With Automatic CMOS Mode-Matching. *IEEE Journal of Solid-State Circuits*, 44:1593–1608, 2009.

[7] Lipka R. Younkin D. Hrudey P. Tovera J. Rahafrooz A. Zaman M. F. Nagpal S. Jafri I. Serrano, D. E. and F. Ayazi. Environmentally-robust high-performance tri-axial bulk acoustic wave gyroscopes. In *IEEE Position, Location and Navigation Symposium (PLANS)*, 2016.

[8] Howard H. G. Challoner, A. D. and J. Y. Liu. Boeing disc resonator gyroscope. In *IEEE Position, Location and Navigation Symposium (PLANS)*, 2014.

[9] Lim M. Seeger, J. and S. Nasiri. Development of high-performance, high-volume consumer mems gyroscopes. In *Solid-State Sensors, Actuators, and Microsystems Workshop*, 2010.

[10] Woo J. K. Cho J. Y. Nagourney T. Darvishian A. Shiari B. Boyd, C. and K. Najafi. Effect of drive-axis displacement on mems birdbath resonator gyroscope performance. In *IEEE International Symposium on Inertial Sensors and Systems*, 2017.

[11] Z. Liu. Introduction to inertial navigation and pointing control, 2011.

[12] Bosch Sensortec. *BMA280 Digital, triaxial acceleration sensor*, 8 2014.

[13] TDK - Invensense. *High Performance 6-Axis MEMS MotionTracking Device*, 10 2016.

[14] NXP Semiconductors. *MMA8451Q, 3-axis, 14-bit/8-bit digital accelerometer*, 2 2017.

[15] STMicroelectronics. *High-resolution, high-stability 3-axis digital accelerometer*, 10 2017.

[16] Analog Devices. *Low Noise, Low Drift, Low Power, 3-Axis MEMS Accelerometers*, 4 2018.

[17] Miola J. Setterlund R. Dow B. Hopkins, R. and W. Sawyer. The silicon oscillating accelerometer: A high-performance mems accelerometer for precision navigation and strategic guidance applications, 2006. The Draper Technology Digest.

[18] Dong Y. Nguyen A.M. Rudolf F. Stauffer J.M. Ullah P. Zwahlen, P. and V. Ragot. Breakthrough in high performance inertial navigation grade sigma-delta mems accelerometer. In *IEEE/ION Position, Location and Navigation Symposium*, pages 15–19, 2012.

[19] Kulah H. Chae, J. and K. Najafi. An in-plane high-sensitivity, low-noise micro-g silicon accelerometer with CMOS readout circuitry. *Journal of microelectromechanical systems*, 13:628–635, 2004.

[20] B. E. Boser and R. T. Howe. Surface micromachined accelerometers. *Journal of Solid-State Circuits*, 31:366–375, 1996.

[21] C.H. Liu and T.W. Kenny. A high-precision, wide-bandwidth micromachined tunneling accelerometer. *Journal of microelectromechanical systems*, 10:425–433, 2001.

[22] STMicroelectronics. *iNEMO inertial module: always-on 3D accelerometer and 3D gyroscope*, 8 2017.

[23] Bosch Sensortec. *BMG 250 low noise, low power triaxial gyroscope*, 7 2016.

[24] InvenSense. *MPU-6000 and MPU-6050 Product Specification*, 8 2013. Rev. 3.4.

[25] Bosch Sensortec. *BMI 160 small, low power inertial measurement unit*, 2 2015.

[26] Analog Devices. *±450/Sec Precision Angular Rate Sensor*, 2 2014.

[27] Askari S. Asadian, M.H. and A.M. Shkel. An ultrahigh vacuum packaging process demonstrating over 2 million Q-factor in MEMS vibratory gyroscopes. *IEEE sensors letters*, 1:1–4, 2017.

[28] Sharma A. Hao Z. Zaman, M. F. and F. Ayazi. A Mode-Matched Silicon-Yaw Tuning-Fork Gyroscope With Subdegree-Per-Hour Allan Deviation Bias Instability. *Journal of Microelectromechanical Systems*, 17:1526–1536, 2008.

[29] O. J. Woodman. An introduction to inertial navigation. Technical report, University of Cambridge Computer Laboratory, 2007.

[30] Woo J. K. Yan J. Peterson R. L. Cho, J. Y. and K. Najafi. Fused-Silica Micro Birdbath Resonator Gyroscope (-BRG). *Journal of Microelectromechanical Systems*, 23:66–77, 2014.

[31] Woo J.K. Aktakka, E.E. and K. Najafi. On-chip characterization of scale-factor of a mems gyroscope via a micro calibration platform. In *IEEE International Symposium on Inertial Sensors and Systems (INERTIAL)*, 2017.

[32] Aaltonen L. Saukoski, M. and K.A. Halonen. Zero-rate output and quadrature compensation in vibratory MEMS gyroscopes. *IEEE Sensors Journal*, 7:1639–1652, 2007.

[33] J.W. Joo and S.H. Choa. Deformation behavior of MEMS gyroscope sensor package subjected to temperature change. *IEEE Transactions on Components and Packaging Technologies*, 30:346–354, 2007.

[34] Park S. Zhang, X. and M. W. Judy. Accurate assessment of packaging stress effects on MEMS sensors by measurement and sensorpackage interaction simulations. *Journal of Microelectromechanical Systems*, 16:639–649, 2007.

[35] Mukherjee T. Tatar, E. and G. K. Fedder. On-chip characterization of stress effects on gyroscope zero rate output and scale factor. In *28th IEEE International Conference on Micro Electro Mechanical Systems (MEMS)*, 2015.

[36] Najafi K. Lemmerhirt D.F. Yang, D.M. and J. Mitchell. A micro thermal and stress isolation platform for inertial sensors. In *IEEE International Symposium on Inertial Sensors and Systems (INERTIAL)*, 2018.

[37] Everything about stmicroelectronics3-axis digital mems gyroscopes. Technical report, S.T.Microelectronics, 07 2011.

[38] Joyce R.J. Kubena, R.L. and A.D. Challoner. Correlation of frequency, temperature, and bias stability of a si ring gyro. In *Inertial Sensors and Systems*, 2016.

[39] Lee S. Yoon, S.W. and K. Najafi. Vibration-induced errors in MEMS tuning fork gyroscopes. *Sensors and Actuators A: Physical*, 180:32–44, 2012.

[40] Wang W. Yang S. Oh, H. and K. Lee. Development of SAW based gyroscope with high shock and thermal stability. *Sensors and Actuators A: Physical*, 165:8–15, 2011.

[41] Schofield A.R. Trusov A.A. Costlow L.E. Acar, C. and A.M. Shkel. Environmentally robust MEMS vibratory gyroscopes for automotive applications. *IEEE Sensors Journal*, 9:1895–1906, 2009.

[42] S. W. Yoon. *Vibration Isolation and Shock Protection for MEMS*. PhD thesis, University of Michigan Ann Arbor, 2009.

[43] Kline M.H. Izyumin I. Yeh Y.C. Eminoglu, B. and B.E. Boser. Background calibrated mems gyroscope. In *IEEE Sensors*, 2014.

[44] Woo J.K. Lee S. Mitchell J. Challoner A.D. Yang, D. and K. Najafi. A Micro Oven-Control System for Inertial Sensors. *Journal of Microelectromechanical Systems*, 26:507–518, 2017.

[45] J.R. Vig. Introduction to quartz frequency standards. revision. Technical report, Army Lab Command, Fort Monmouth, NJ: Electronics Technology and Devices Lab, 1992.

[46] J.R. Vig and R.L. Filler. Temperature stable crystal oscillator. In *IEEE transactions on ultrasonics, ferroelectrics, and frequency control*, 1995.

[47] Chen C. Y. Li C. S. Chin C. H. Li, M. H. and S. S. Li. A monolithic CMOS-MEMS oscillator based on an ultra-low-power ovenized micromechanical resonator. *Journal of Microelectromechanical Systems*, 24:360–372, 2015.

[48] Hong V. A. Park W. Yang Y. Chen Y. Ng E. J. Huynh J. Challoner A. D. Goodson K. E. Ahn, C. H. and T. W. Kenny. On-chip ovenization of encapsulated disk resonator gyroscope (drg). In *18th IEEE International Conference on Solid-State Sensors, Actuators and Microsystems (TRANSDUCERS)*, 2015.

[49] Z. Wu and M. Rais-Zadeh. A temperature-stable piezoelectric MEMS oscillator using a CMOS PLL circuit for temperature sensing and oven control. *Journal of Microelectromechanical Systems*, 24:1747–1758, 2015.

[50] Lee S. W. Lee, S. H. and K. Najafi. A generic environment-resistant packaging technology for mems. In *Solid-State Sensors, Actuators and Microsystems Conference (TRANSDUCERS)*, 2007.

[51] S. H. Lee. *Wafer-level packaging for environment-resistant microinstruments*. PhD thesis, University of Michigan Ann Arbor, 2009.

[52] IEEE Standard Specification Format Guide and Test Procedure for Single-Axis Interferometric Fiber Optic Gyros. Standard, The Institute of Electrical and Electronics Engineers, New York, NY, 1997.

[53] M. M. Tehrani. Ring laser gyro data analysis with cluster sampling technique. In *Proceedings of SPIE*, 1983.

[54] Allan variance: Noise analysis for gyroscopes. Technical report, Freescale Semiconductor, 2015.

[55] Falco G. Falletti E. Dovis F. Quinchia, A.G. and C. Ferrer. A comparison between different error modeling of MEMS applied to GPS/INS integrated systems. *Sensors*, 13:9549–9588, 2013.

[56] General Electric Company. *Fluid Flow Databook*, volume 1. Genium Publishing, 1982.

[57] Woo J. K. Najafi K. Lee S. Mitchell J. Challoner D. Yang, D. +/-2ppm frequency drift and 300x reduction of bias drift of commercial 6-axis inertial measurement units using a low-power oven-control micro platform. In *IEEE SENSORS*, 2015.

[58] A.D. Mitchell, J. Challoner and S. Lee. System with oven control and compensation for detecting motion and/or orientation, May 4 2017. US Patent App. 14/925,349.

[59] Hao Z. Pourkamali, S. and F. Ayazi. VHF single crystal silicon capacitive elliptic bulk-mode disk resonators-part II: implementation and characterization. *Journal of Microelectromechanical Systems*, 13:1054–1062, 2004.

[60] M.A. Johnson and M.H. Moradi. *PID control*. Springer-Verlag London Limited, 2005.

[61] J.G. Ziegler and N.B. Nichols. Optimum settings for automatic controllers. *Transactions of the ASME*, 64:759–765, 1942.

[62] E. Yoon and K. Najafi. Lecture notes in intorduction to mems, September 2014.

[63] A. Patoun. *A Compleat Treatise of Practical Navigation Demonstrated From its First Principles*, volume 1. Eighteenth Century Collections Online (ECCO), 1770.

[64] Systron Donner Inertial. *QRS11 MEMS Quartz Angular Rate Sensor*.

[65] Systron Donner Inertial. *SDD3000-A01 MEMS Quartz Digital Single Axis Rate Sensor*.

[66] Silicon Sensing. *CRS39 Analogue Angular Rate Sensor High Performance MEMS Gyroscope*, 2017.

[67] Systron Donner Inertial. *QRS116 MEMS Quartz Angular Rate Sensor*.

[68] R.C. Chang and L.C. Kuo. A new low-voltage charge pump circuit for pll. In *IEEE International Symposium on Circuits and Systems*, 2000.

[69] Malow E.J. Silva R. Wright S. Quade D. Vivod S.L. Guo H. Guo J. Meador, M.A.B. and M. Cakmak. Mechanically strong, flexible polyimide aerogels crosslinked with aromatic triamine. *ACS applied materials and interfaces*, 4:536–544, 2012.

[70] Crayons on aerogel over a flame. `https://stardust.jpl.nasa.gov/photo/aerogel.html`. Accessed: 2018-12-28.

[71] Johnson B. Melde, B. and P. Charles. Mesoporous silicate materials in sensing. *Sensors*, 8:5202–5228, 2008.

[72] Fan S.K. Kim C.J. Wu M.C. Paik, J.A. and B. Dunn. Micromachining of mesoporous oxide films for microelectromechanical system structures. *Journal of materials research*, 17:2121–2129, 2002.

[73] Rolled film aerogel. https://www.blueshiftmaterials.com/rolled-film-aerogel.

[74] Peterson R.L. Egert, D. and K. Najafi. Parylene microprobes with engineered stiffness and shape for improved insertion. In *IEEE 16th International Solid-State Sensors, Actuators and Microsystems Conference (TRANSDUCERS)*, 2011.

[75] Henkel. *ABLEBOND 84-1LMI Technical Datasheet*, 3 2009.

[76] Noh S. Zhang H. Choe C. Jiu J. Nagao S. Chen, C. and K. Suganuma. Bonding technology based on solid porous Ag for large area chips. *Scripta Materialia*, 146:123–127, 2018.

[77] Shiari B. Cho J.Y. Nagourney T. Darvishian, A. and K. Najafi. Anchor loss in hemispherical shell resonators. *Journal of Microelectromechanical Systems*, 26:51–66, 2017.

[78] K. Jousten. *Handbook of vacuum technology*. John Wiley & Sons, 2016.

[79] Wu Y.C. Lai, C.H. and C.C. Chiang. Effects of forming gas annealing on low-temperature ordering of FePt films. *Journal of applied physics*, 97:10H305, 2005.

[80] Rossmann T. Ma, Q. and Z. Guo. Temperature sensitivity of silica micro-resonators. *Journal of Physics D: Applied Physics*, 41:1–6, 2008.

[81] Broas M. Makkonen J. Mattila T.T. Hokka J. Li, J. and M. Paulasto-Krckel. Shock impact reliability and failure analysis of a three-axis MEMS gyroscope. *Journal of Microelectromechanical systems*, 23:347–355, 2014.

[82] P.M. Leonhardt. Acceleration levels of dropped objects. Technical report, Endevco Corporation, 2001.

[83] Pegasus-Glass. *PYREX Technical Information: Properties Of Borosilicate (PYREX 7740) Glass.*

[84] Maxim Integrated Products. *500kHz, 36V Output, SOT23, PWM Step-Up DC-DC Converters*, 3 2009. Rev. 2.

[85] Melamud R. Chandorkar S.A. Lord S.F. Salvia, J.C. and T.W. Kenny. Real-time temperature compensation of MEMS oscillators using an integrated micro-oven and a phase-locked loop. *Journal of Microelectromechanical Systems*, 19:192–201, 2010.

[86] Cutler L.S. Ingman E.M. Johnson J.L. Karlquist, R.K. and T. Parisek. The theory of zero-gradient crystal ovens. In *IEEE International Frequency Control Symposium*, 1997.

[87] Airloy x116 non-flammable strong aerogel large panels. http://www.buyaerogel.com/product/airloy-x116-large-panels/. Accessed: 2019-2-23.